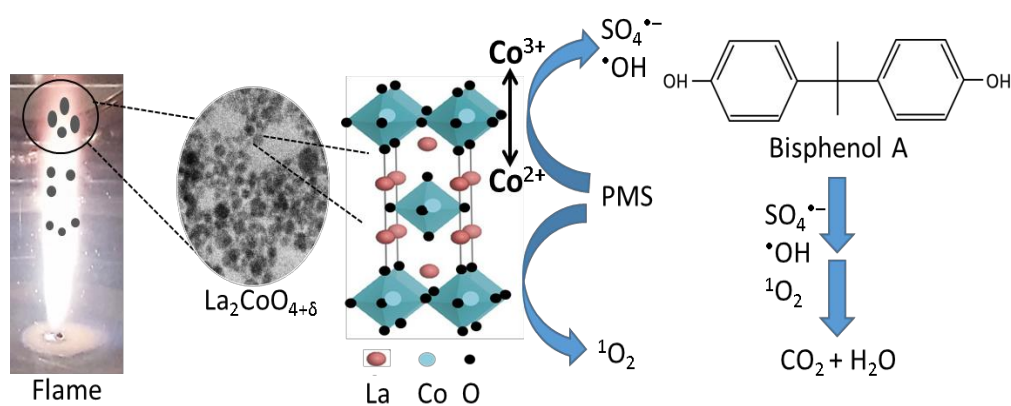


Graphical abstract

Enhanced heterogeneous activation of peroxymonosulfate by Ruddlesden-Popper-type $\text{La}_2\text{CoO}_{4+\delta}$ nanoparticles for bisphenol A degradation

Mohaned Hammad^{a*}, Baris Alkan^a, Ahmed K. Al-kamal^a, Md Yusuf Ali^a, Cheolyong Kim^b, Haakon T. A. Wiedemann^c, Dina Klippert^c, Torsten C. Schmidt^b, Christopher W. M. Kay^{c,d}, Hartmut Wiggers^{a,c*}



Highlight

- A scalable spray-flame technique to produce novel $\text{La}_2\text{CoO}_{4+\delta}$ nanoparticles is presented.
- Outstanding PMS activation capacity with very low amount of leached cobalt was achieved
- A high content of Co^{2+} and high electron transfer ability are identified as key parameter
- The $\text{La}_2\text{CoO}_{4+\delta}$ material has a good chemical stability over a wide pH range (3-11)

Enhanced heterogeneous activation of peroxydisulfate by Ruddlesden-Popper-type $\text{La}_2\text{CoO}_{4+\delta}$ nanoparticles for bisphenol A degradation

Mohaned Hammad^{a*}, Baris Alkan^a, Ahmed k. Al-kamal^a, Md Yusuf Ali^a, Cheolyong Kim^b, Haakon T. A. Wiedemann^c, Dina Klippert^c, Torsten C. Schmidt^b, Christopher W. M. Kay^{c,e}, Hartmut Wiggers^{a,d*}

^a IVG, Institute for Combustion and Gas Dynamics – Reactive Fluids, University of Duisburg-Essen, Duisburg, Germany

^b Instrumental Analytical Chemistry and Centre for Water and Environmental Research, University of Duisburg-Essen, Essen, Germany

^c Department of Chemistry, Saarland University, Saarbrücken, Germany

^d CENIDE, Center for Nanointegration Duisburg-Essen, University of Duisburg-Essen, Duisburg, Germany

^e London Centre for Nanotechnology, University College London, 17-19 Gordon Street, London WC1H 0AH, United Kingdom

Corresponding authors:

Dr. Mohaned Hammad*

Prof. Hartmut Wiggers*

Institute for Combustion and Gas Dynamics – Reactive Fluids

University of Duisburg-Essen

Carl-Benz-Str. 199

47057 Duisburg, Germany

mohaned.hammad@uni-due.de

hartmut.wiggers@uni-due.de

Abstract

The scalable synthesis of stable catalysts for environmental remediation applications remains challenging. Nonetheless, metal leaching is a serious environmental issue hindering the practical application of transition-metal based catalysts including Co-based catalysts. Herein, for the first time, we describe a facile one-step and scalable synthesis of $\text{La}_2\text{CoO}_{4+\delta}$ nanoparticles containing excess oxygen interstitials ($+\delta$) using spray-flame synthesis, and use them as a stable and efficient catalyst for activating peroxymonosulfate (PMS) towards the degradation of bisphenol A. Importantly, the $\text{La}_2\text{CoO}_{4+\delta}$ catalyst exhibits higher catalytic degradation of bisphenol A (95% in 20 minutes) and stably than LaCoO_{3-x} nanoparticles (60%) in the peroxymonosulfate activation system. A high-surface area and high content of Co^{2+} in the structure showed a strong impact on the catalytic performance of the $\text{La}_2\text{CoO}_{4+\delta}$ +PMS system. Despite its high specific surface area, our results showed a very low amount of leached cobalt (less than 0.04 mg/L in 30 minutes), indicating high chemical stability. According to the radical quenching experiments and the electron paramagnetic resonance technology $\text{SO}_4^{\bullet-}$, $\cdot\text{OH}$, and $^1\text{O}_2$ were generated and $\text{SO}_4^{\bullet-}$ played a dominant role in bisphenol A degradation. Moreover, the $\text{La}_2\text{CoO}_{4+\delta}$ +PMS system maintained conspicuous catalytic performance for the degradation of other organic pollutants including methyl orange, rhodamine B, and methylene blue. Overall, our results showed that we developed a new synthesis method for stable $\text{La}_2\text{CoO}_{4+\delta}$ nanoparticles that can be used as a highly active heterogeneous catalyst for PMS-assisted oxidation of organic pollutants.

Keywords: heterogeneous catalysis, gas-phase synthesis, peroxymonosulfate, sulfate radical, bisphenol A degradation.

1 Introduction

1
2
3
4 Bisphenol A (2,2-bis (4-hydroxyphenyl) propane, BPA) is intensively utilized as a key
5
6 industrial chemical for the production of polycarbonate plastics and epoxy resins in the plastic
7
8 industry [1]. Unfortunately, a significant amount of BPA is continuously discharged into the
9
10 environment and detected in food, drinking water, and aquatic animals [2]. BPA mimics
11
12 estrogenic activity in human and animal bodies causing disruption of the endocrine system
13
14 through interfering with hormonal and homeostatic functions [3]. Therefore, the removal of
15
16 BPA especially from aquatic environments is of great interest.
17
18

19
20
21 Recently, the Fenton reaction employing hydroxyl ($\cdot\text{OH}$) and sulfate radicals ($\text{SO}_4^{\cdot-}$) has
22
23 attracted increasing interest as a promising method to oxidize organic pollutant in water [4].
24
25 Compared to the $\cdot\text{OH}$, $\text{SO}_4^{\cdot-}$ has a longer half-life time, higher standard oxidation potential, and
26
27 wider pH range applicability, which is more efficient for bisphenol A degradation [5]. Sulfate
28
29 radicals are typically generated by peroxymonosulfate (PMS) or peroxydisulfate (PDS)
30
31 activation using heat [6], ultrasound [7], UV [8], electrochemical processes [9], and transition
32
33 metal ions (e.g., Co, Mn, Cu, Fe, and Ni) [10].
34
35
36

37
38 Homogenous transition-metal catalysis is one of the feasible and cost-effective ways to generate
39
40 $\text{SO}_4^{\cdot-}$. Among the transition metals, Co^{2+} exhibits the most efficient homogeneous catalyst for
41
42 PMS activation [11] and is catalytically regenerated during PMS activation, which enhances its
43
44 catalytic activity [12]. However, Co-based homogeneous activation has serious drawbacks,
45
46 especially secondary metal-ion pollution and high catalyst consumption [13]. Thus,
47
48 heterogeneous, Co-based catalysts such as cobalt oxide [14], cobalt-based bimetallic oxide [15],
49
50 and supported cobalt oxide [16] nanoparticles have been investigated for PMS activation.
51
52 Among them, transition metal-based perovskites (ABO_3 with B being the transition metal) have
53
54 attracted increasing attention in heterogeneous catalysis because of their flexibility in chemical
55
56 composition and their ability for generating oxygen vacancies, thus enabling catalytic redox
57
58
59
60
61
62
63
64
65

1 reactions [17]. More recently, some reports have focused on different transition metals La-based
2 perovskites (LaMO_3 (M: Co, Cu, Fe, and Ni)) for PMS activation [18]. Particularly, LaCoO_3
3 perovskites have been considered being very effective to generate $\text{SO}_4^{\cdot-}$ from PMS as Co–O–
4 bonding enable a high number of reactive sites for PMS activation [19]. Moreover, the B-site
5 cation deficiency in the $\text{LaCoO}_{3-\delta}$ perovskite structures enhances their catalytic activity [20].
6
7 Although these perovskite catalysts have some advantages such as high catalytic activity, they
8 suffer from metal leaching in the aqueous medium [21]. Thus, it is essential to explore highly
9 stable heterogeneous catalysts for PMS activation.
10
11

12 Compared to transition metal-based perovskites (ABO_3), Ruddlesden-Popper mixed oxides
13 (A_2BO_4) nanoparticles (RP-MONp) exhibit higher stability and redox ability, because their
14 crystal structure is more opened due to extra space between A-site atoms. They consist of
15 alternating layers of perovskite (ABO_3) and rock salt (AO) [22]. These layered structures
16 possess good thermal stability [23] and show high ionic conductivity. Another study on RP-
17 based catalysts show that the RP-MONp reveal better oxygen diffusion coefficients and surface
18 exchange than other ABO_3 perovskite type.
19
20

21 RP-MONp has been reported as catalysts in various heterogeneously catalyzed reactions
22 including oxygen reduction reaction (ORR) and evolution reaction (OER) [24], photocatalytic
23 water splitting process [25], NO and CO removal [26], oxidation of urea and small alcohols
24 [27], a cathode for a solid oxide electrolysis cell [28], and Fenton reaction [29]. In this regard,
25 $\text{La}_2\text{CoO}_{4+\delta}$ nanoparticles have been selected to use as a PMS activator as their structure can
26 tolerate excess amounts of oxygen up to a δ of 0.16 upon oxidation at room temperature [30].
27
28 Moreover, the oxidation state of the B-site ion in this structure can be controlled by tailoring
29 oxygen non-stoichiometry [31]. Therefore, $\text{La}_2\text{CoO}_{4+\delta}$ materials are suitable for advanced
30 catalytic oxidation processes.
31
32

33 Several methods have been demonstrated to synthesize Ruddlesden-Popper mixed oxide
34 catalysts including co-precipitation [32], sol-gel synthesis [33], combustion methods [34],
35
36
37
38
39
40
41
42
43
44
45
46
47
48
49
50
51
52
53
54
55
56
57
58
59
60
61
62
63
64
65

1 hydrothermal flow synthesis [35], and solid-state reactions [36]. However, all these methods
2 require high-temperature annealing (≥ 1000 °C) at an extended period, which promotes particle
3 growth and sintering, leading to a reduced catalytically active surface area. As an alternative,
4 spray-flame synthesis is an established method to produce non-sintered, homogeneously
5 distributed perovskite nanoparticles down to 10 nm, and even below [37,38]. Surface-sensitive
6 measurements of spray-flame-synthesized LaCoO_3 nanoparticles show a high content of Co^{2+}
7 ions being present at the particles' surface. These results are attributed to the local formation of
8 oxygen-deficient or layered perovskite structures such as A_2BO_4 type Ruddlesden-Popper
9 structures, which can stabilize Co^{2+} much better than the pure perovskite ABO_3 [39]. Thus,
10 specific interest is in the targeted formation and investigation of Co-containing Ruddlesden-
11 Popper-type nanoparticles as highly active heterogeneous catalysts.
12
13
14
15
16
17
18
19
20
21
22
23
24
25

26 Herein, the objective of this study is to seek a one-step method for the synthesis of $\text{La}_2\text{CoO}_{4+\delta}$
27 nanoparticles using a spray-flame method with the purpose of improving their catalytic
28 performance with a very low amount of metal leaching to achieve the environmental friendly
29 requirement during organic pollutant degradation. The performance for PMS activation of the
30 catalysts was evaluated in terms of BPA degradation. Moreover, effects of several important
31 parameters such as initial pH value, inorganic anions (such as Cl^- , NO_3^- , H_2PO_4^- , HCO_3^- , etc.),
32 and water bodies (tap water) on their catalytic performances along with the reusability of the
33 $\text{La}_2\text{CoO}_{4+\delta}$ nanoparticles were also investigated. The radical generation was identified by
34 radical scavenging experiments and electron paramagnetic resonance studies and a mechanism
35 for PMS activation is proposed.
36
37
38
39
40
41
42
43
44
45
46
47
48
49
50
51
52
53
54
55
56
57
58
59
60
61
62
63
64
65

2 Material and methods

2.1 Materials

For the synthesis of $\text{La}_2\text{CoO}_{4+\delta}$ nanoparticles, $\text{La}(\text{CH}_3\text{COO})_3 \cdot 1.05 \text{H}_2\text{O}$ (99.9%; Sigma-Aldrich) and $\text{Co}(\text{CH}_3\text{COO})_2 \cdot 4 \text{H}_2\text{O}$ ($\geq 98\%$; Sigma-Aldrich) were used as the metal precursors while propionic acid (ACS reagent, $>99.5\%$; Sigma-Aldrich), propanol (anhydrous, 99.7%; Sigma-Aldrich), ultrapure DI water (18.2 M Ω cm at 25 °C) and ethanol ($>99.8\%$; Sigma-Aldrich) were employed as solvents. 5,5-dimethyl-1-pyrroline N-oxide (DMPO) ($>97.0\%$; TCI), Bisphenol A ($\geq 99\%$), potassium peroxymonosulfate, sodium phosphate monobasic ($\geq 99\%$), sodium nitrate ($\geq 99\%$), sodium chloride ($\geq 99\%$), sodium hydrogencarbonate ($\geq 99\%$), β -carotene ($\geq 95\%$), tert-butyl alcohol ($\geq 99.5\%$), methylene blue ($\geq 97\%$), rhodamine B ($\geq 95\%$), Acid Orange 7 ($\geq 98\%$) potassium bicarbonate ($\geq 99.5\%$), potassium iodide ($\geq 90\%$), and absolute ethanol were purchased from Sigma Aldrich to be used for the catalytic tests. Sodium hydroxide ($\geq 97\%$) and nitric acid ($>69\%$, both VWR International) were used to adjust the pH of the respective solution. All chemicals were used as received without further purification.

2.2 Synthesis of $\text{La}_2\text{CoO}_{4+\delta}$ nanoparticles

Spray-flame synthesis of lattice-oxygen-deficient LaCoO_{3-x} perovskite and interstitial-oxygen-rich $\text{La}_2\text{CoO}_{4+\delta}$ Ruddlesden-Popper phases was carried out similar to the process described before [40] (Figure 2) using precursor solutions and process parameters are given in detail in Table S1. Briefly, a precursor solution is transferred to a syringe pump connected to a homemade enclosed reactor, which allows full control of gas flow and pressure. The syringe pump is connected to a hollow needle (0.4 mm inner diameter and 0.7 mm outer diameter) adjusted in the center of a burner nozzle. Oxygen dispersion gas (introduced through an annular gap surrounding the hollow needle) was used to atomize the precursor solution injected into the

1 precursor solution as well as lower volume flows of the CH₄/O₂ pilot flame gases and the O₂
2 dispersion gas.
3

4 The precursor solution for LaCoO_{3-x} was composed of propionic acid mixed with 1-propanol
5 in a glass flask at room temperature and stirred for 10 min. La- and Co-precursors were
6 subsequently added to the solvent mixture and the flask was then heated in a silicon oil bath at
7 60°C to dissolve the precursors under constant magnetic stirring for 2 h. The total metal
8 concentration of La and Co was adjusted to 0.45 M and the nominal atomic ratios of La/Co
9 were adjusted to 1. For the precursor solution of La₂CoO_{4+δ}, a similar procedure was used except
10 that octanoic acid was used as an organic acid and a small amount of water was added to the
11 solvent mixture to appropriately dissolve the La-acetate. The precursor solution was then heated
12 in a silicon oil bath at 70°C under constant magnetic stirring for 2 h. The total metal
13 concentration of La and Co was adjusted to 0.15 M and the nominal atomic ratios of La/Co
14 were adjusted to 2.
15
16
17
18
19
20
21
22
23
24
25
26
27
28
29
30

31 **2.3 Methods of Characterization**

32
33 The crystal phases of the samples were determined by X-ray diffraction (XRD) recorded with
34 a PANalytical X-ray diffractometer X'Pert (Netherlands) with a Cu K_α radiation ($\lambda = 1.5406$
35 Å). The surface morphology and energy dispersive spectra were analyzed using transmission
36 electron microscopy (TEM, JEM-2200FS, JEOL, Japan). X-ray photoelectron spectroscopy
37 (XPS, VersaProbe II, ULVAC-PHI, Japan with monochromatic Al K_α light at an emission angle
38 of 45°) was applied to analyze the surface elemental composition and chemical state of the
39 samples. All measured binding energies were referenced to the Cu2p peak at 933 eV.
40
41 Attenuated total reflectance Fourier transform infrared spectra (ATR-FTIR) were recorded
42 using a Bruker Vertex 80 spectrometer (Bruker, Germany) in the 400-4000 cm⁻¹ region. The
43 zeta potential of the catalysts was determined by a Malvern Zetasizer (Malvern Panalytical,
44
45
46
47
48
49
50
51
52
53
54
55
56
57
58
59
60
61
62
63
64
65

1
2
3
4
5
6
7
8
9
10
11
12
13
14
15
16
17
18
19
20
21
22
23
24
25
26
27
28
29
30
31
32
33
34
35
36
37
38
39
40
41
42
43
44
45
46
47
48
49
50
51
52
53
54
55
56
57
58
59
60
61
62
63
64
65

United Kingdom). The specific surface areas were measured on a Quantachrome NOVA2200 (Quantachrome GmbH, Germany) analyzer at 77 K by the Brunauer–Emmett–Teller (BET) Nitrogen adsorption/desorption isotherm method.

2.4 Catalytic studies and analyses

The catalytic performance of the as-prepared $\text{La}_2\text{CoO}_{4+\delta}$ nanoparticles was evaluated for PMS activation in terms of BPA degradation. The concentration of BPA was analyzed by high-performance liquid chromatography (HPLC, Shimadzu LC-10AT, Shimadzu Corporation, Japan). The HPLC was equipped with an SPD-M10A diode array detector (detection wavelength: 230 nm) and a Kinetex C18 reverse-phase column (100 mm×2 mm, 5 μm). The flow rate of the mobile phase consisting of 0.1% formic acid in water and acetonitrile (80:20, v:v) was 0.5 mL/min. In a typical experiment, 2.4 mg catalyst was initially dispersed into 40 mL BPA aqueous solution (40 mg/L) at 25 °C and the resultant suspension was magnetically stirred in dark for 30 min to ensure the establishment of an adsorption/desorption equilibrium between catalyst and BPA before a certain dose of PMS was added. At selected time intervals, 2 mL of the suspension was withdrawn, immediately quenched with 0.5 mL methanol, filtered with a 0.22 μm membrane filter, centrifuged (12000 rpm, 20 min) to remove the particles, and injected into the HPLC vial. 1.0 M solutions of NaOH and HNO_3 were used to adjust the initial pH. The same operation was repeated with different organic compounds such as methylene blue (MB), rhodamine B (RhB), and acid orange 7 (AO7). The concentrations of MB, RhB, and AO7 were measured by UV-Vis spectroscopy (Varian Cary 400, Varian, Australia) at wavelengths of 664, 553, and 483 nm, respectively. To study the reusability of the $\text{La}_2\text{CoO}_{4+\delta}$ nanoparticles, the catalyst was collected by centrifugation at 14000 rpm for 10 min, followed by thorough washing with deionized water and then re-dispersed into fresh BPA solution for the next experimental run reaction.

1
2
3
4
5
6
7
8
9
10
11
12
13
14
15
16
17
18
19
20
21
22
23
24
25
26
27
28
29
30
31
32
33
34
35
36
37
38
39
40
41
42
43
44
45
46
47
48
49
50
51
52
53
54
55
56
57
58
59
60
61
62
63
64
65

To compare the degradation reaction kinetics of the BPA degradation, pseudo-first-order kinetics reaction rate constants (k_{app}) of the BPA removal were measured according to the following equation:

$$\ln \left(\frac{C_t}{C_0} \right) = -k_{app}t \text{ (equation 1)}$$

where C_t depicts the pollutant concentration at time, C_0 is the initial pollutant concentration, k_{app} is the kinetics rate constants, and t is the time.

The concentration of dissolved metal ions in concentrated nitric acid (60%) was determined by atomic absorption spectroscopy (M-Serie, Thermo Electron Corporation, Germany). Total organic carbon (TOC) concentration was analyzed by using a TOC-L total organic carbon analyzer (Shimadzu, Japan) to evaluate the degree of BPA mineralization. To determine the residual concentration of PMS, 100 μ L of the suspension was withdrawn at given time intervals, mixed with potassium bicarbonate (5 g/L) and potassium iodide (40 g/L), and then was measured by UV-Vis spectroscopy (Varian Cary 400, Varian, Australia) at a wavelength of 352 nm. To evaluate the contributions of the radical reactions to mineralization, a certain amount of ethanol (EtOH), tert-butyl alcohol (TBA), and β -carotene were added to the catalytic system to scavenge $SO_4^{\cdot-}$ and $\cdot OH$, $\cdot OH$, and 1O_2 respectively. The β -carotene experiment was conducted in 37 mL of acetone and 3 mL of deionized water for dissolving PMS. The intermediates of BPA degradation were identified by Agilent 1260 Infinity II Liquid Chromatography system equipped with 6120 Quadrupole Mass Detector and Kinetex C18 reverse-phase column (100 mm \times 2 mm, 5 μ m). Same mobile phase as HPLC. The generated reactive radicals were measured using the MiniScope MS-5000 electron spin resonance spectrometer (Freiberg Instruments, Germany) with a microwave power of 10 mW and modulation amplitude of 0.2 G at room temperature. The impedance measurements were performed using impedance analyzer Solartron 1260 (Solartron Analytical, United Kingdom) with a frequency range of 0.1 Hz–1

1 MHz and with an output signal voltage of 100 mV. Gold sputtering was done on both sides of
2 the pellet before the experiment.
3
4

5 **3 Results and discussion**

6
7
8
9

10 **3.1 Characterization of $\text{La}_2\text{CoO}_{4+\delta}$ nanoparticles**

11
12
13

14 The XRD patterns of the pristine nanoparticles were analyzed to determine crystalline phases
15 of $\text{La}_2\text{CoO}_{4+\delta}$ and LaCoO_{3-x} (Figure 2). The $\text{LaCoO}_{3-\delta}$ diffraction peaks show a good match to
16 a $\text{LaCoO}_{2.937}$ perovskite phase (Inorganic Crystal Structure Database (ICSD): 153995), while
17 the XRD pattern of $\text{La}_2\text{CoO}_{4+\delta}$ can be mainly related to a Ruddlesden-Popper type phase of
18 $\text{La}_2\text{CoO}_{4.13}$ (ICSD: 237238) with a minor content of $\text{La}(\text{OH})_3$ (ICSD: 31584). Notably, the
19 diffraction peaks of $\text{La}_2\text{CoO}_{4+\delta}$ appear more broadened compared to those of LaCoO_{3-x} , and
20 this finding points out a low degree of crystallinity and/or small crystal sizes of $\text{La}_2\text{CoO}_{4+\delta}$. A
21 possible decrease in the crystallinity of the $\text{La}_2\text{CoO}_{4+\delta}$ phase can be owing to hydrated groups
22 incorporated in its structure as previously reported in Co-based Ruddlesden-Popper type
23 crystals [41].
24
25
26
27
28
29
30
31
32
33
34
35
36
37
38
39
40
41
42
43
44
45
46
47
48
49
50
51
52
53
54
55
56
57
58
59
60
61
62
63
64
65

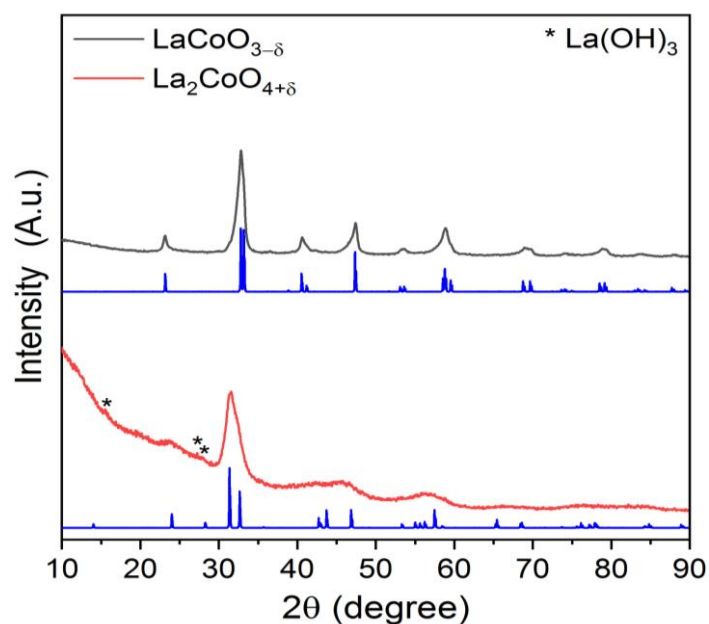
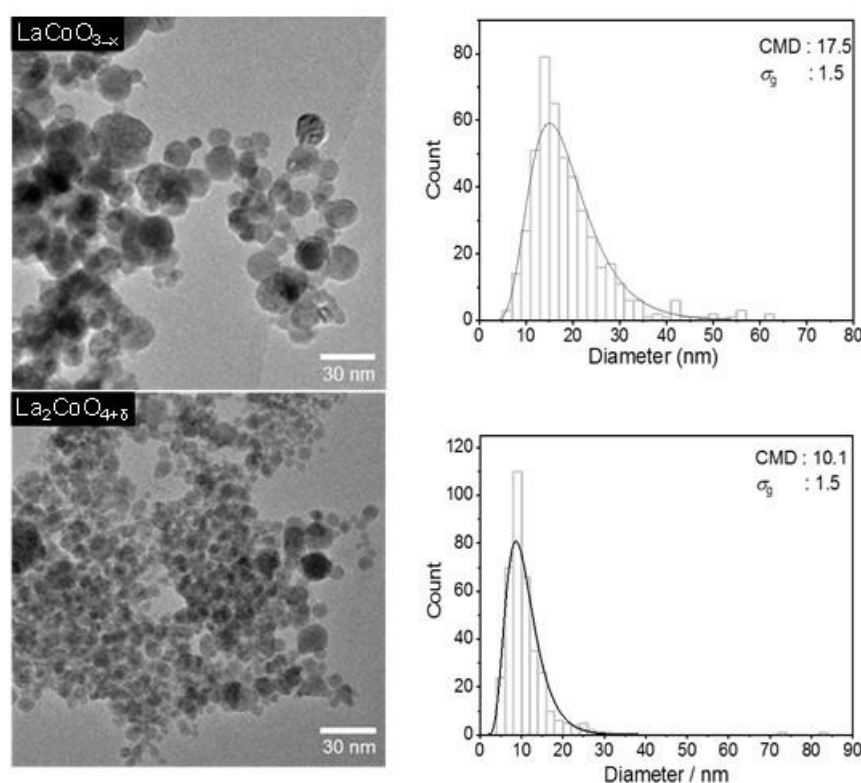


Figure 2. XRD patterns of as-prepared LaCoO_{3-x} and $\text{La}_2\text{CoO}_{4+\delta}$ nanoparticles. Reference phases are $\text{La}_2\text{CoO}_{4.13}$ (ICSD no: 237238, blue line), $\text{LaCoO}_{2.937}$ (ICSD no: 153995, blue line), and La(OH)_3 (ICSD no: 31584), respectively.

To investigate the morphology and size distribution of as-prepared nanoparticles, transmission electron microscopy was performed as shown in Figure 3. For both samples, the count median diameter (CMD) and geometric standard deviation (σ_g) were determined by fitting the size distribution histograms of about 400 nanoparticles to a lognormal distribution. The CMD and σ_g of LaCoO_{3-x} were measured as 17.5 nm and 1.5 while those of $\text{La}_2\text{CoO}_{4+\delta}$ correspond to 10.1 nm and 1.5. Lower particle sizes of $\text{La}_2\text{CoO}_{4+\delta}$ are also implied from the specific surface areas of $\text{La}_2\text{CoO}_{4+\delta}$ and LaCoO_{3-x} nanoparticles being determined by nitrogen adsorption-desorption isotherms through the BET measurements (Brunauer Emmett Teller) [32]. The specific surface area (SSA) of $\text{La}_2\text{CoO}_{4+\delta}$ was measured as $89 \text{ m}^2/\text{g}$, being considerably higher than the SSA of LaCoO_{3-x} about $43 \text{ m}^2/\text{g}$. The lower CMD and higher SSA of $\text{La}_2\text{CoO}_{4+\delta}$ particles compared to LaCoO_{3-x} can be associated with precursor characteristics in that lower concentration of La and Co metals being used in the precursor solution of $\text{La}_2\text{CoO}_{4+\delta}$ bring about lower nanoparticles sizes and higher SSA of $\text{La}_2\text{CoO}_{4+\delta}$ (see supplementary material, Table S1). Beside that, the chemical composition of LaCoO_{3-x} , being determined by Energy dispersive X-Ray (EDX)

1 measurements, indicate that their La/Co atomic ratio is close to unity (see supplementary
2 material, Figure S1), while La/Co atomic ratio of $\text{La}_2\text{CoO}_{4+\delta}$ was measured about 2.3, being
3 slightly higher than nominal atomic ratios in $\text{La}_2\text{CoO}_{4+\delta}$. Excess La content can be owing to
4 small amounts of $\text{La}(\text{OH})_3$ secondary phase being detected from XRD analyses. Overall, the
5 bulk compositions of LaCoO_{3-x} and $\text{La}_2\text{CoO}_{4+\delta}$ nanoparticles show a good agreement with the
6 expected nominal compositions.
7
8
9
10
11
12
13
14
15
16
17
18
19
20
21
22
23
24
25
26
27
28
29
30
31
32
33
34
35
36
37
38
39
40



41
42
43
44
45
46
47
48
49
50
51
52
53
54
55
56
57
58
59
60
61
62
63
64
65

Figure 3. TEM images of LaCoO_{3-x} and $\text{La}_2\text{CoO}_{4+\delta}$ materials (on the left side) and the respective histograms of their particle sizes fitted to a log-normal particle size distribution (on the right side). Count median particle diameter and geometric standard deviation were abbreviated as a CMD and a σ_g , respectively.

Surface oxidation state and chemistry of Co and La ions were further investigated using the core-level and satellite X-ray photoelectron spectroscopy (XPS) features of $\text{Co}2p_{3/2}$ and $\text{La}3d_{5/2}$ spectra (Figure 4). In both $\text{Co}2p$ and $\text{La}3d$ spectra, lower XPS signals were measured for $\text{La}_2\text{CoO}_{4+\delta}$ compared to for LaCoO_{3-x} and this result can be well attributed to the effect of higher contents of carbon impurities in $\text{La}_2\text{CoO}_{4+\delta}$, which reduce the overall XPS signals coming from this sample. For LaCoO_{3-x} , the intense XPS signals of the $\text{Co}2p_{3/2}$ at $\sim 779.3, 781.4$

1 and 789.5 eV correspond to those of Co^{3+} ions [42], whereas the low-intensity signals of
 2 $\text{Co}2p_{3/2}$ at ~ 780.4 , 782.2 and 785.2 eV can be assigned to the core-level and satellites of Co^{2+}
 3 ions, respectively [43]. The atomic proportion of surface $\text{Co}^{3+}/\text{Co}^{2+}$ for LaCoO_{3-x} was found as
 4 58/42, which corresponds to a chemical formula of $\text{LaCoO}_{2.58}$. At the XPS spectra of
 5 $\text{La}_2\text{CoO}_{4+\delta}$, the core-level signals of Co^{2+} ions show more intense XPS signals relative to those
 6 of Co^{3+} ions, and a low-intensity peak of metallic Co appears at ~ 778.1 eV. The proportion of
 7 $\text{Co}^{3+}/\text{Co}^{2+}/\text{Co}$ in $\text{La}_2\text{CoO}_{4+\delta}$ was measured as 40/49/11, confirming reduced oxidation of cobalt
 8 ions in this sample. The La3d spectra of LaCoO_{3-x} and $\text{La}_2\text{CoO}_{4+\delta}$ exhibit similar XPS spectra
 9 at different binding energies. The core-level and satellite signals of La3d_{5/2} signals of LaCoO_{3-x}
 10 are visible at ~ 833.3 and ~ 837.1 eV with a multiplet splitting of 3.8 eV being in agreement
 11 with the La3d spectrum of La-based perovskites [44]. Despite showing a similar multiplet
 12 splitting, La3d_{5/2} signals of $\text{La}_2\text{CoO}_{4+\delta}$ shift about 1.1 eV towards higher binding energies, and
 13 these spectral feature can be attributed to those of Ruddlesden-Popper-type compounds [45].
 14 All in all, XPS analyses of Co and La ions draw attention to a varying content of surface Co^{2+}
 15 and Co^{3+} ions in LaCoO_{3-x} and $\text{La}_2\text{CoO}_{4+\delta}$, which can govern their catalytic activity for PMS
 16 activation.

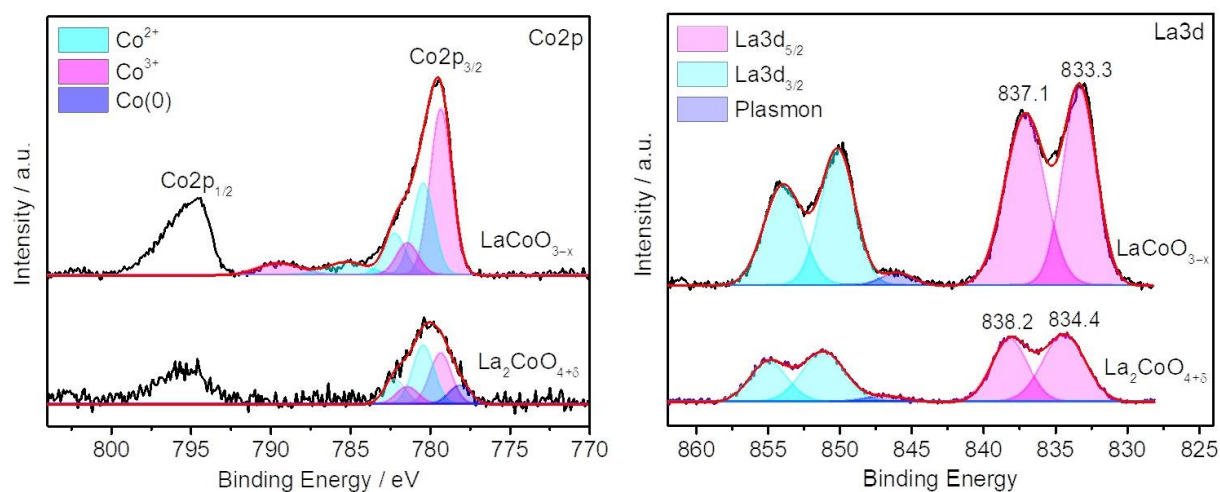


Figure 4. XPS spectra of Co2p and La3d in LaCoO_{3-x} and $\text{La}_2\text{CoO}_{4+\delta}$, respectively.

3.2 Catalytic activity and stability of catalysts

Figure 5a shows the removal efficiency of BPA for both catalysts and control measurements. The removal of BPA was negligible in the presence of only PMS or catalyst. In the case of the $\text{La}_2\text{CoO}_{4+\delta}$ /PMS system, 97% BPA was removed within 30 min, which was higher than that in a LaCoO_{3-x} +PMS system (70%), implying that the catalytic activity of $\text{La}_2\text{CoO}_{4+\delta}$ is significantly higher than that of LaCoO_{3-x} . We attribute the remarkable catalytic enhancement of $\text{La}_2\text{CoO}_{4+\delta}$ to the high specific surface area (see supplementary material, Figure S2) and especially the higher surface concentration of Co^{2+} compared to LaCoO_{3-x} material, as we have shown before (Figure 4). Moreover, the BPA removal in both systems could be well fitted by pseudo-first-order kinetics (see supplementary material, Figure S3). The k_{app} of BPA degradation was about 0.152 min^{-1} and 0.03 min^{-1} for $\text{La}_2\text{CoO}_{4+\delta}$ and LaCoO_{3-x} samples, respectively, confirming that the catalytic performance of the $\text{La}_2\text{CoO}_{4+\delta}$ catalyst is significantly higher than that of LaCoO_{3-x} material.

Besides, electrochemical impedance analyses were further performed to investigate the electron transfer behavior of both materials (see supplementary material, Figure S5). Obviously, the $\text{La}_2\text{CoO}_{4+\delta}$ electrode (44898Ω) exhibited lower charge transfer resistance compared to the LaCoO_{3-x} electrode ($5705 \times 10^7 \Omega$), suggesting that the electron transfer in the $\text{La}_2\text{CoO}_{4+\delta}$ structure is more efficient than that in the LaCoO_{3-x} , which is favorable for the electron transfer during PMS activation [46].

To support these findings, the variation of residual PMS during the PMS activation in both systems was performed (Figure 5c). The residual PMS concentration in a $\text{La}_2\text{CoO}_{4+\delta}$ +PMS system (0.1 mM) was lower to a LaCoO_3 +PMS system (0.32 mM), which attributed to about 80 % and 64 % of the initial PMS concentration, respectively, manifesting that the $\text{La}_2\text{CoO}_{4+\delta}$ +PMS system activates more PMS as a result of fast electron transport from PMS molecules to the $\text{La}_2\text{CoO}_{4+\delta}$, and therefore higher BPA degradation is obtained. The comparison

of previously reported heterogeneous Co-based catalysts for BPA degradation (Table 1) indicates that $\text{La}_2\text{CoO}_{4+\delta}$ materials show a remarkable improvement for PMS activation.

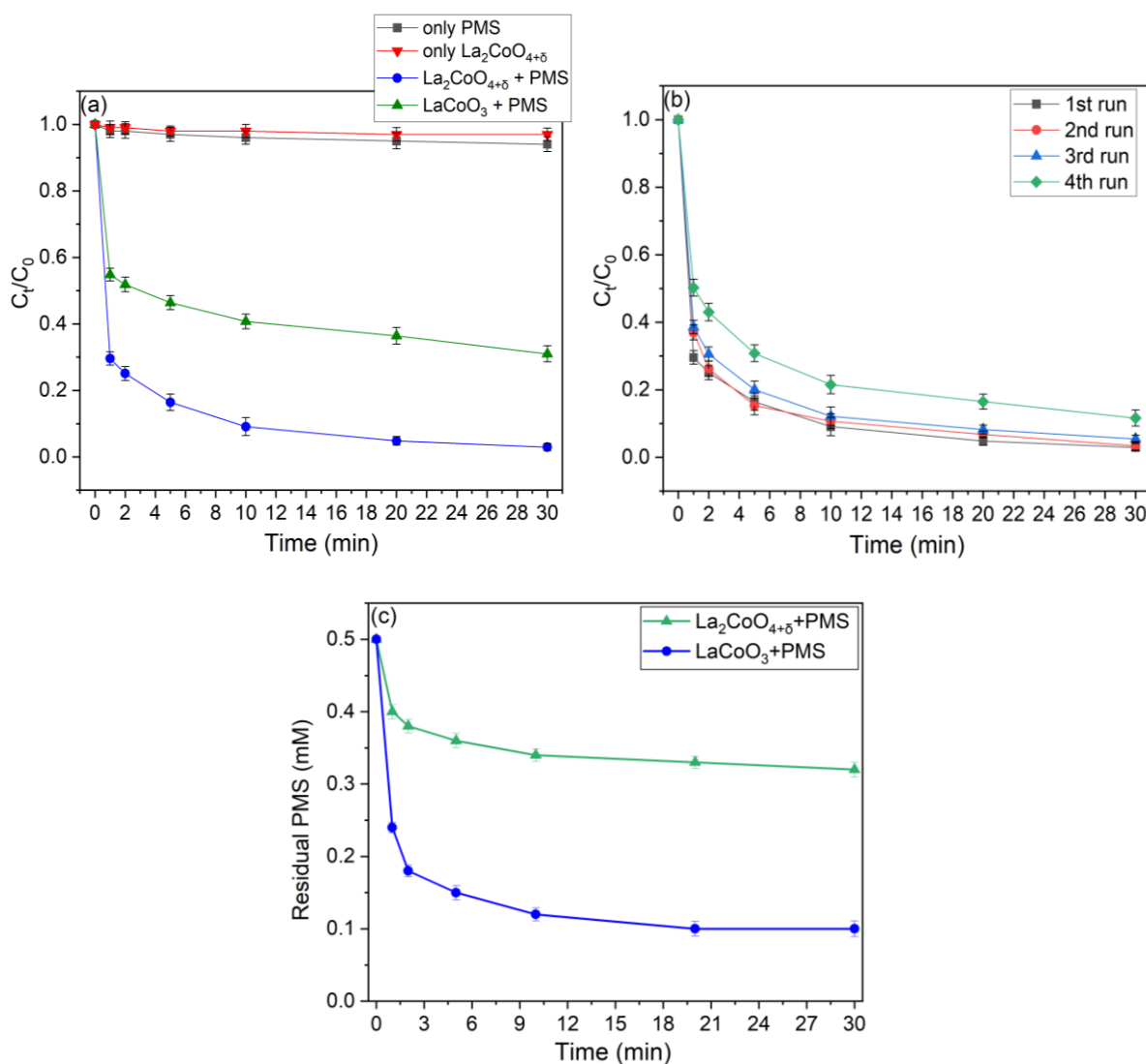


Figure 5. a) BPA degradation with various catalysts in different reaction systems, b) Stability tests of $\text{La}_2\text{CoO}_{4+\delta}$, and c) Residual PMS variation along with the reaction time in different systems. Reaction conditions: (BPA) = 40 mg/L, (PMS) = 0.5 mM; (Catalyst) = 60 mg/L, initial pH = 6.8.

Table 1. Comparison of the BPA degradation by $\text{La}_2\text{CoO}_{4+\delta}$ in this work with those of other related Co-based catalysts in the literature.

| Catalyst | Dosage (mg L ⁻¹) | BPA conc. (mg L ⁻¹) | PMS conc (mM) | BPA removal (%) | Time (min) | Co leaching (mg L ⁻¹) | References |
|-------------------------------|---------------------------------|------------------------------------|------------------|--------------------|---------------|--------------------------------------|------------|
| $\text{CoFe}_2\text{O}_{4-x}$ | 50 | 30 | 1 | 98 | 30 | ≈ 1.2 | [47] |

| | | | | | | | |
|--|-----|----|------|-----|----|---------|-----------|
| Co ₃ O ₄ /MXene | 100 | 20 | 1 | >99 | 20 | ≈ 0.36 | [48] |
| Fe _{0.8} Co _{2.2} O ₄ | 100 | 20 | 0.65 | 95 | 60 | ≈ 0.36 | [49] |
| Fe ₃ Co ₇ /C | 100 | 20 | 1.3 | 98 | 30 | ≈ 3.30 | [50] |
| Co ₃ O ₄ /MOFs | 100 | 20 | 1.6 | 95 | 10 | ≈ 0.35 | [51] |
| Co ₃ O ₄ /Bi ₂ O ₃ | 300 | 20 | 0.32 | 98 | 30 | ≈ 0.35 | [52] |
| Co ₃ O ₄ /CC | 100 | 10 | 0.32 | >99 | 10 | ≈ 0.25 | [53] |
| LaCoO ₃ /Al ₂ O ₃ | 100 | 5 | 0.32 | >99 | 30 | ≈ 0.001 | [54] |
| (Atrazine) | | | | | | | |
| La ₂ CoO _{4+δ} | 60 | 40 | 0.5 | 95 | 20 | ≈ 0.04 | This work |

To confirm the practicability of the catalyst in the La₂CoO_{4+δ}/PMS system, the reusability of the La₂CoO_{4+δ} material was investigated in four cycling experiments. As displayed in Figure 5b, the reused La₂CoO_{4+δ} exhibited excellent catalytic performance in the first three reaction runs. However, a decrease in BPA removal to 89% was observed after three reaction runs, which can be mainly ascribed to the formation of insoluble lanthanum carbonate contaminants on the surface of La₂CoO_{4+δ}, resulting in the partial deactivation of the catalyst. This structural change of La₂CoO_{4+δ} catalyst could also be identified by XRD and FTIR. The XRD pattern of the multiple used catalyst shows three additional low-intensity peaks at $2\theta = 18.4^\circ$, 28° , and 41° (Figure 6a), which can be indexed to the orthorhombic layered structure of La₂(CO₃)₃·1.1H₂O [55]. A similar phenomenon was also observed in the FTIR spectra (Figure 6b). An increased peak intensity around 730 cm⁻¹ might be ascribed to the formation of La₂(CO₃)₃·1.1H₂O.

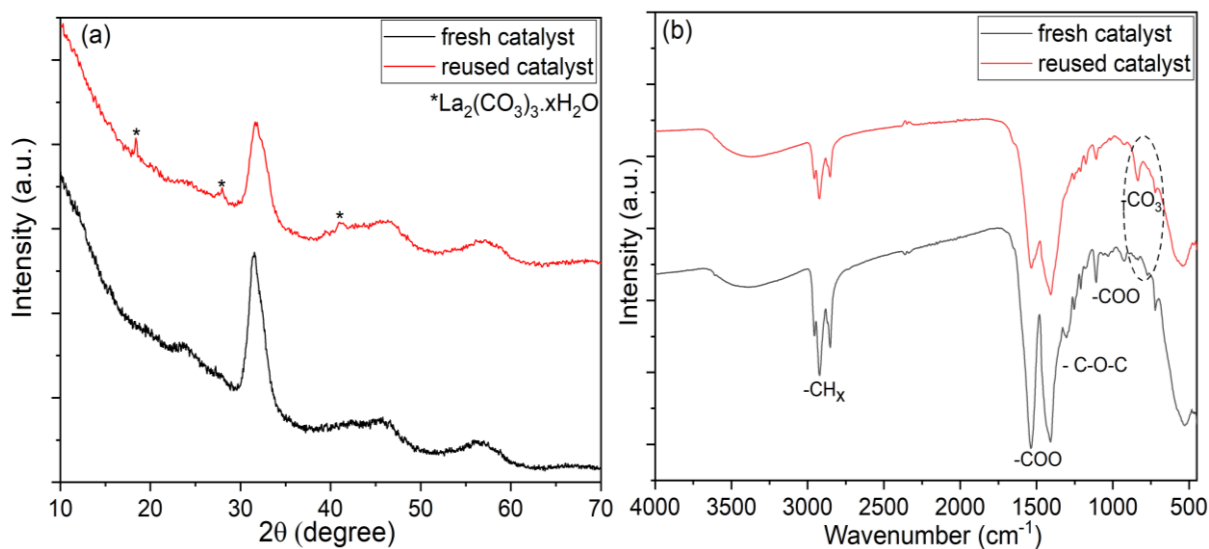


Figure 6. a) XRD patterns and b) FTIR spectra of fresh and reused $\text{La}_2\text{CoO}_{4+\delta}$ catalyst.

Besides, the mineralization extent of BPA was monitored by the TOC analyzer. After 30 min, the TOC removals of BPA was 27% and 49% for LaCoO_{3-x} and $\text{La}_2\text{CoO}_{4+\delta}$ materials, respectively, implying the high BPA mineralization in the $\text{La}_2\text{CoO}_{4+\delta}$ +PMS system. Moreover, the leaching of cobalt and lanthanum ions was further investigated by Atomic absorption spectroscopy analysis during the PMS activation. Compared to LaCoO_{3-x} (2.6 mg/mL), $\text{La}_2\text{CoO}_{4+\delta}$ showed less Co leaching (0.04 mg/mL), which attributed to about 4.3% and 0.06% of the initial catalyst concentration, respectively, whereas the concentrations of leached lanthanum for LaCoO_{3-x} and $\text{La}_2\text{CoO}_{4+\delta}$ material were around 6.1 and 0.7 mg/L, respectively, which accounted to about 10.2% and 1.17% of the initial catalyst concentration, respectively. We also tested the BPA removal efficiency using the leaching solution under the same conditions (see supplementary material, Figure S5). The BPA removal on the homogenous system was less than 5%. This suggests that the catalytic activity mainly results from the heterogeneous $\text{La}_2\text{CoO}_{4+\delta}$ /PMS system. These results showed that the $\text{La}_2\text{CoO}_{4+\delta}$ catalyst exhibited high stability and very low cobalt leaching, compared to other cobalt-based catalysts used for BPA removal (Table 1) and further cobalt-based perovskite materials [21,56,57].

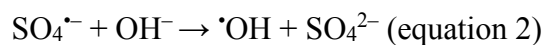
3.3 Reactive species and possible mechanisms

Many reactive oxygen species such as $\text{SO}_4^{\cdot-}$, $\cdot\text{OH}$, $^1\text{O}_2$, and $\text{SO}_5^{\cdot-}$ may be involved in the reaction of BPA degradation [58]. $\text{SO}_5^{\cdot-}$ is less efficient to oxidize BPA due to its lower oxidation potential (0.81 V) compared to $\text{SO}_4^{\cdot-}$ [59]. To obtain more detailed information, the contribution of different reactive radicals to BPA degradation was investigated by radical quenching experiments employing $\text{La}_2\text{CoO}_{4+\delta}$. Ethanol (EtOH) was used to scavenge both $\text{SO}_4^{\cdot-}$ and $\cdot\text{OH}$ with a high quenching rate constant of $k_{\text{EtOH}/\cdot\text{OH}} = (1.2\text{--}2.8) \times 10^9 \text{ M}^{-1} \text{ s}^{-1}$ and $k_{\text{EtOH}/\text{SO}_4^{\cdot-}} = (1.6\text{--}7.7) \times 10^9 \text{ M}^{-1} \text{ s}^{-1}$, while tert-butyl alcohol (TBA) was employed to scavenge only $\cdot\text{OH}$ with a reaction rate constant of $k_{\text{TBA}/\cdot\text{OH}} = (3.8\text{--}7.6) \times 10^9 \text{ M}^{-1} \text{ s}^{-1}$ [60]. Besides, singlet oxygen ($^1\text{O}_2$) might be generated during PMS activation and can be scavenged by β -carotene with a rate constant of $k_{\beta\text{-carotene}/^1\text{O}_2} = (2\text{--}3.0) \times 10^{10} \text{ M}^{-1} \text{ s}^{-1}$ [61].

As shown in Figure 7a, the addition of 0.1 M TBA slightly decreased the removal efficiency of BPA from 97% to 95%, and no significant change was observed with the increase of TBA concentration to 0.5 M. In contrast, the BPA removal with the addition of 0.1 M EtOH was significantly declined to about 58% and even stronger inhibition was observed for higher EtOH concentration (0.5 M). However, the BPA removal inhibited by EtOH is incomplete, suggesting that other reactive radicals may be involved in the reaction of BPA degradation. Singlet oxygen ($^1\text{O}_2$) may also be generated during PMS activation and can be scavenged by β -carotene [61]. It can be seen from Figure 7a that the addition of 0.5 mM β -carotene declined the BPA removal to about 76%, while the addition of β -carotene together with EtOH decreased the BPA degradation in 30 min from 97% to 6%, confirming that $^1\text{O}_2$ was also generated in $\text{La}_2\text{CoO}_{4+\delta}$ /PMS system. The quenching tests imply that $\text{SO}_4^{\cdot-}$ is the primary active radical in the $\text{La}_2\text{CoO}_{4+\delta}$ /PMS system.

To confirm the generation of reactive radicals from PMS activation, Electron paramagnetic resonance (EPR) experiments were conducted using DMPO and TEMP as a radical spin-

1 trapping agent (Figure 7b). There was no signal peak detected in the presence of PMS alone or
2 of the catalyst alone, indicating that no radicals could be generated with bare PMS and catalyst.
3
4 However, when $\text{La}_2\text{CoO}_{4+\delta}/\text{PMS}$ were added, characteristic signals for DMPO- $\cdot\text{OH}$ adducts
5 (with hyperfine splitting constants of $\alpha_{\text{H}} = \alpha_{\text{N}} = 14.8$ G) and DMPO- $\text{SO}_4^{\cdot-}$ adducts ($\alpha_{\text{N}} = 13.2$
6 G, $\alpha_{\text{N}} = 9.6$ G, $\alpha_{\text{H}} = 1.48$ G, $\alpha_{\text{H}} = 0.78$ G) were observed, confirming that both $\cdot\text{OH}$ and $\text{SO}_4^{\cdot-}$
7 radicals were produced by the $\text{La}_2\text{CoO}_{4+\delta}/\text{PMS}$ system. Thus, we propose that the generation
8 of $\cdot\text{OH}$ in the $\text{La}_2\text{CoO}_{4+\delta}/\text{PMS}$ system originates from the reaction of $\text{SO}_4^{\cdot-}$ with the hydroxyl
9 ion (equation 2) or water (equation 3) [62].
10
11
12
13
14
15
16
17
18



19 Besides, TEMP was selected as the trapping agent to gain more evidence for the generation of
20 the singlet oxygen ($^1\text{O}_2$) by the EPR test. As illustrated in Figure 7c, the characteristic peak
21 assigned to TEMP- $^1\text{O}_2$ was observed in the $\text{La}_2\text{CoO}_{4+\delta}/\text{PMS}$ system. These results are in good
22 agreement with the quenching experiments, confirming the generation of $^1\text{O}_2$ in the
23
24 $\text{La}_2\text{CoO}_{4+\delta}/\text{PMS}$ system.
25
26
27
28
29
30
31
32
33
34
35
36
37
38
39
40
41
42
43
44
45
46
47
48
49
50
51
52
53
54
55
56
57
58
59
60
61
62
63
64
65

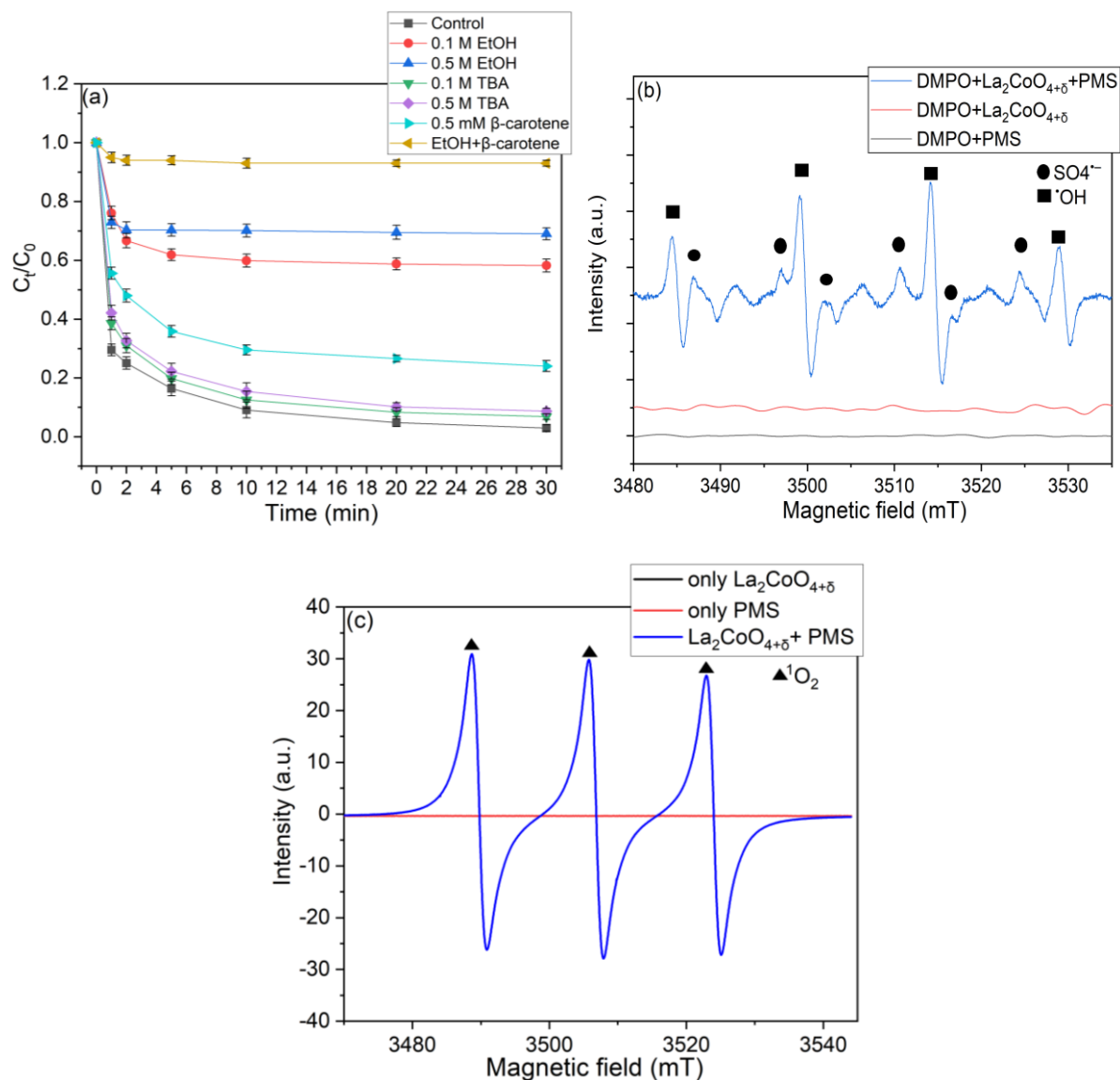


Figure 7. a) Effect of radical scavengers on BPA degradation in different reaction systems, b) EPR spectra in La₂CoO_{4+δ}/PMS systems with DMPO, and c) EPR spectra in La₂CoO_{4+δ}/PMS systems with TEMP as the trapping agent. Reaction conditions: (BPA) = 40 mg/L, (PMS) = 0.5 mM, (Catalyst) = 60 mg/L, (DMPO) = 50 mM, (TEMP) = 20 mM, initial pH = 6.8.

To further elaborate the mechanism of PMS activation and the roles of La, Co, and O species, the XPS spectra of La₂CoO_{4+δ} before and after four runs of catalytic experiments were studied. There was no significant change in the La3d spectrum before and after the reaction, suggesting that La is not involved in the PMS activation (see supplementary material, Figure S6). As depicted in Figure 8a, the high-resolution Co2p XPS spectra for the fresh and used catalysts can be fitted using five core-level peaks centered at ~ 778.2, 779.6, 780.4, 781.4, 782.2, and the

1 satellite at ~ 786.5 eV. The binding energies at 780.4 and 782.1 eV can be assigned to Co^{2+} ,
 2 whereas the peak with binding energy positioned at 779.6 eV is assigned to Co^{3+} [63]. The
 3 shake-up satellite peak located at 786.5 eV indicates the presence of Co^{2+} species [63]. While
 4 the initial proportions of $\text{Co}^{3+}/\text{Co}^{2+}/\text{Co}$ were determined as of 40/49/11, they changed to
 5 37/55/8, which indicates the increasing surface concentration of Co^{2+} ions, thereby suggesting
 6 a redox process $\text{Co}^{2+}-\text{Co}^{3+}-\text{Co}^{2+}$ at the catalysts' surface. This finding is supported by analyzing
 7 the O1s spectra (Figure 8b). The peaks centered at 528.5, 529.6, 531.2, and 532.3 eV
 8 corresponded to oxygen in the lattice (O_L), surface $\text{O}_2^{2-}/\text{O}^-$, surface hydroxyl groups (OH), and
 9 adsorbed water and carbonates, respectively, and initially accounted for 22, 13, 46, and 19%,
 10 respectively [57]. These relative proportions change to 17, 14, 46, and 23% after the catalytic
 11 reaction [57]. The decline in the O_L can be attributed to the release of oxygen in combination
 12 with the reduction of Co^{3+} to Co^{2+} , suggesting that lattice O_L participated in the cobalt redox
 13 reaction. The increment of carbonate and water contents can be attributed to the formation of
 14 lanthanum carbonate contaminants on the surface of $\text{La}_2\text{CoO}_{4+\delta}$.

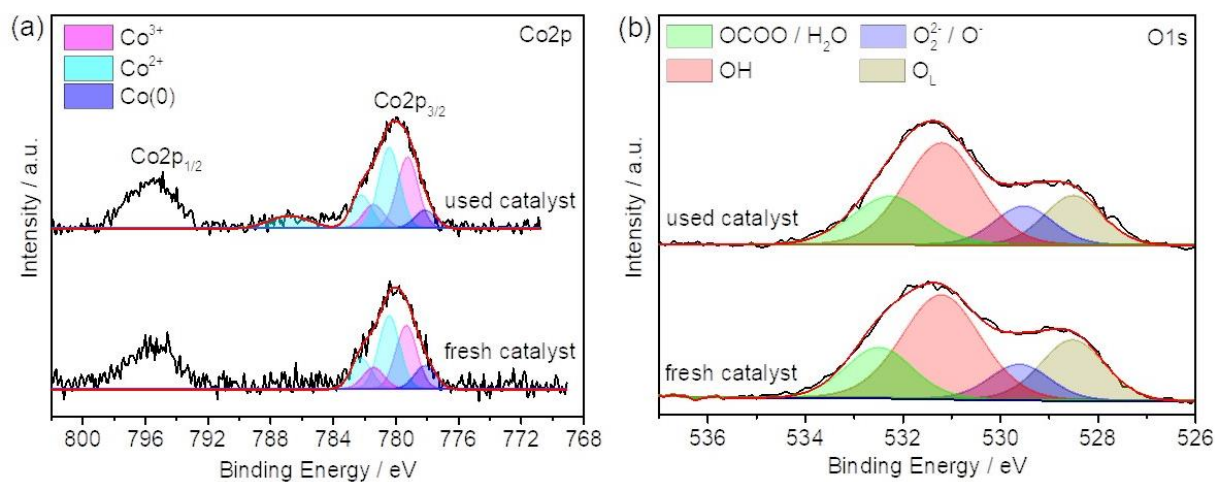
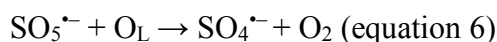
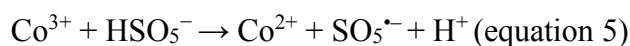
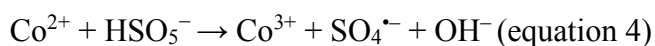


Figure 8. XPS spectra of (a) Co2p and (b) O1s for fresh and used $\text{La}_2\text{CoO}_{4+\delta}$ materials.

52 Based on the above results, a catalysis mechanism of PMS activation by $\text{La}_2\text{CoO}_{4+\delta}$ is proposed
 53 as follows: After the addition of PMS, $\text{SO}_4^{\bullet-}$ is initially generated by the activation of HSO_5^-
 54 species on $\text{La}_2\text{CoO}_{4+\delta}$ (equation 4) and simultaneously some initially generated $\text{SO}_4^{\bullet-}$ will react
 55 with hydroxyl ion or water to generate $\bullet\text{OH}$ (equations 2-3). These radicals could attack and
 56

1 mineralize the BPA to small organic intermediates and then finally to CO₂ (equation 7). On the
 2 other hand, to keep the charge balance on the La₂CoO_{4+δ} surface, the lattice oxygen could
 3 facilitate the charge transfer to Co³⁺ and be released to the system in the form of O₂ (equations
 4 5-6). Lattice oxygen ions cannot migrate from the bulk to the surface under the atmospheric
 5 ambience in the aqueous phase [64,65]. Therefore, the adsorbed oxygen might transform to
 6 lattice oxygen due to the high charge and oxygen-ion conductivity [66], which would
 7 compensate the surface lattice oxygen to improve catalytic efficiency. Furthermore, since the
 8 standard potential value of Co²⁺/Co³⁺ redox pairs (1.8 V) is higher than that of HSO₅⁻/SO₅⁻
 9 (1.1 V), the reduction of Co³⁺ is thermodynamically favorable. Therefore, the regeneration of
 10 the catalyst can be achieved by the reverse electron transfer from Co³⁺ to Co²⁺.



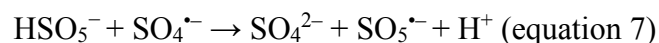
34 **3.4 Effect of reaction parameters on BPA degradation**

35 To select the optimum dosage of La₂CoO_{4+δ} and PMS concentration, the influence of catalyst
 36 dosage and PMS concentration on the BPA removal efficiency was investigated. Moreover, the
 37 pH of the medium is one of the important factors for the catalytic stability of La₂CoO_{4+δ}. Thus,
 38 different initial pH values, as well as the effect of the inorganic anions in the process of PMS
 39 oxidation, were also investigated as a basis for a practical application of the La₂CoO_{4+δ} catalyst.

40 **3.4.1 Effect of catalyst dose and PMS concentration**

41 Not surprisingly, as depicted in Figure 9a, BPA removal efficiency was enhanced from 37%
 42 within 1 min to 92% when the La₂CoO_{4+δ} loading was increased from between 0.03 to 0.24 g/L.
 43 We attribute this to an increasing number of active sites on the surface of La₂CoO_{4+δ} which are

1 accessible for PMS activation and thus generating more active radicals. The removal efficiency
2 also was promoted as the PMS concentration was increased from 0.25 to 2 mM (Figure 9b),
3
4 however, it decreased slightly in the case of overdose (4 mM), which was most likely due to
5
6 the scavenging of $\text{SO}_4^{\bullet-}$ by the excessive HSO_5^- (equation 7) [67].
7
8

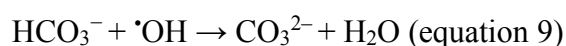


13 3.4.2 Effect of initial pH

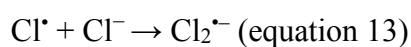
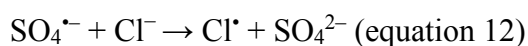
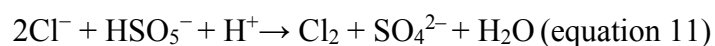
16 The initial pH of the reaction solution is also a significant parameter for PMS activation that
17
18 can affect the interfacial interactions between the catalyst and PMS and is studied in the process
19
20 of PMS oxidation. Figure 9c displays the influence of initial pH on BPA removal in the
21
22 $\text{La}_2\text{CoO}_{4+\delta}$ /PMS system. It is obvious that the BPA was almost degraded within 30 min over a
23
24 pH of 5.0 to 8.8. However, when the initial pH of the solution was adjusted to 3.3 and 10.6, the
25
26 BPA removal efficiency decreased to 50 and 89%, respectively. Since the pK_{a1} of PMS is 0 and
27
28 pK_{a2} is 9.4, PMS mainly exists as HSO_5^- in the pH range of 0-9.4. The pH_{pzc} (pH at the point
29
30 of zero charges) of $\text{La}_2\text{CoO}_{4+\delta}$ is determined at around 9.5 (see supplementary material, Figure
31
32 S7). Accordingly, when pH is higher than 9.4, SO_5^{2-} would replace HSO_5^- , which reduces the
33
34 amount of active reactive species and therefore diminishing the $\text{La}_2\text{CoO}_{4+\delta}$ /PMS efficiency
35
36 [68]. Moreover, the electrostatic repulsion interactions between negatively charged $\text{La}_2\text{CoO}_{4+\delta}$
37
38 and PMS species would slow the activation efficiency of PMS, thus the removal efficiency of
39
40 BPA is reduced. At strong acidic conditions (pH=3.5), a large number of hydrogen ions H^+
41
42 attached to HSO_5^- and form a hydrogen bond, which is unfavorable for the interaction between
43
44 $\text{La}_2\text{CoO}_{4+\delta}$ and PMS species. Furthermore, lower pH can result in the leaching of cobalt ions
45
46 into the solution, resulting in a decrease in the number of catalytic sites (Figure 9d). The
47
48 concentration of leached cobalt ions in the acidic solution (pH = 3.5) is 0.8 mg/L and decreased
49
50 to 0.04 mg/L at pH = 6.8. Therefore, BPA removal efficiency declined significantly at acidic
51
52 conditions (pH = 3.5).
53
54
55
56
57
58
59
60
61
62
63
64
65

3.4.3 Effect of co-existing ions

The effect of various anions relevant in aqueous systems (such as Cl^- , NO_3^- , H_2PO_4^- , HCO_3^- , etc.) on the degradation of BPA in $\text{La}_2\text{CoO}_{4+\delta}/\text{PMS}$ was also investigated and is shown in Figure 9e. Compared to the $\text{La}_2\text{CoO}_{4+\delta}/\text{PMS}$ system, the addition of NO_3^- anion did not have a significant impact on BPA degradation. Moreover, H_2PO_4^- and HCO_3^- anions exerted an inhibitory effect on BPA degradation while the Cl^- anions accelerated the BPA degradation. In the presence of H_2PO_4^- , the degradation of BPA was reduced due to the formation of complex compounds of phosphate-Co during the PMS oxidation system (see supplementary material, Figure S8), which deactivate the catalytic reactive sites. However, HCO_3^- exhibited an inhibitory effect on BPA removal higher than the inhibition caused by H_2PO_4^- . This negative influence might be due to the scavenging effect of $\text{SO}_4^{\bullet-}$ and $\bullet\text{OH}$ by HCO_3^- in the solution (equation 8-9), which can lead to a decrease in the performance of BPA degradation.



In contrast, the removal efficiency is increased with the addition of Cl^- . The positive influence of Cl^- ions on BPA degradation may be ascribed to the generation of active chlorine species (e.g. HOCl , Cl_2 , and Cl^{\bullet}) which participate in BPA degradation because of the reaction with HSO_5^- (equations 10-11) and $\text{SO}_4^{\bullet-}$ (equations 12-13), which can react with the unsaturated bonds of BPA and form organic halides, which are more susceptible to degradation [69].



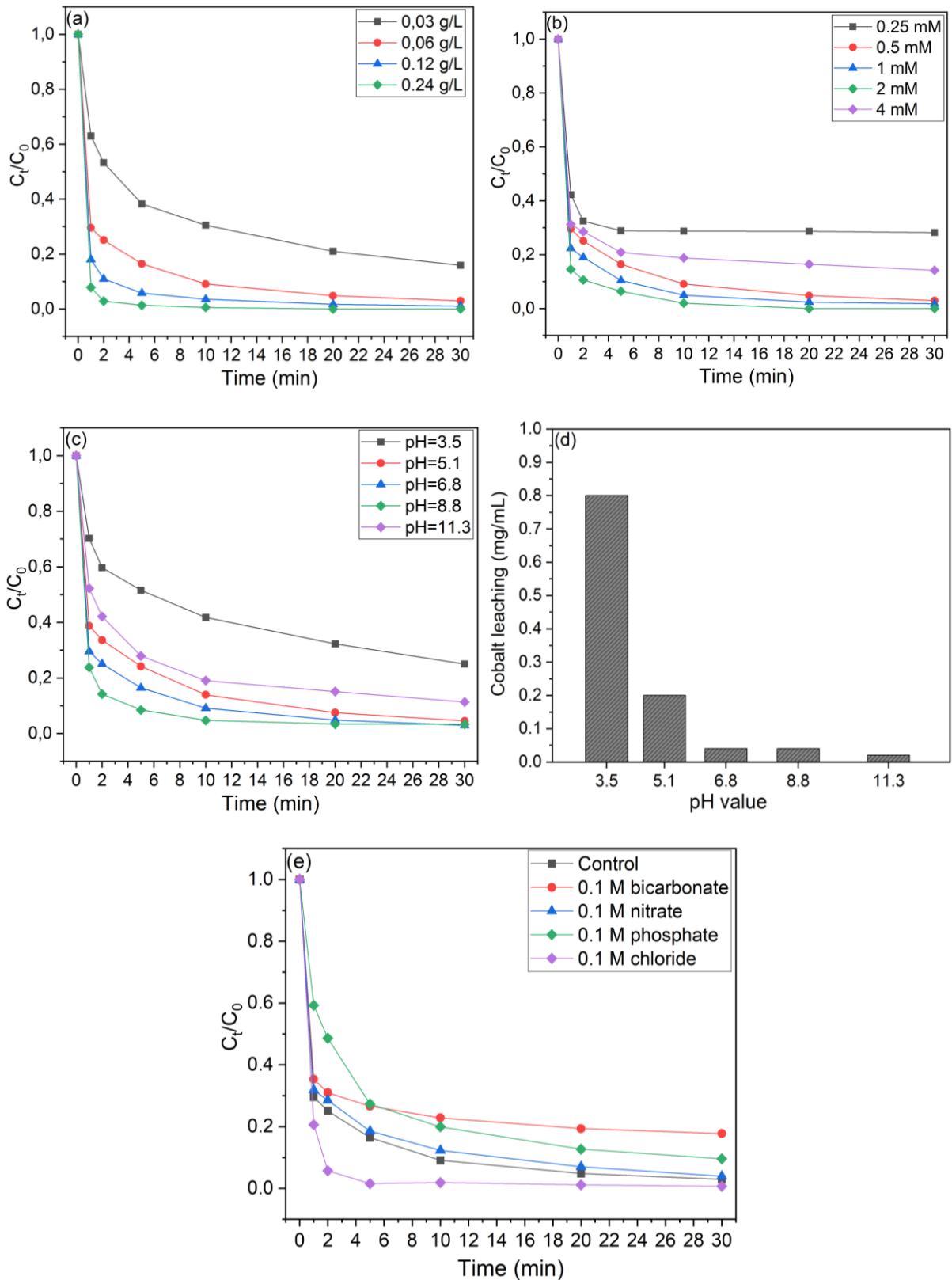


Figure 9. Effects of (a) catalyst loading, (b) PMS dosages, (c) initial pH values and (d) cobalt leaching, and (e) inorganic anions on BPA degradation by $\text{La}_2\text{CoO}_{4+\delta}/\text{PMS}$. Reaction conditions: (BPA) = 40 mg/L, (PMS) = 0.5 mM, (Catalyst) = 60 mg/L, initial pH = 6.8.

3.4.4 Effect of water matrices and different pollutants

The catalytic performance of the $\text{La}_2\text{CoO}_{4+\delta}$ nanoparticles in degrading different types of organic pollutants is important for its environmental remediation applications. Hence, the catalytic activity $\text{La}_2\text{CoO}_{4+\delta}$ was evaluated with different charge organic pollutants including MB, RhB, and AO7. As shown in Figure 10a, the removal efficiency of MB, RhB, and AO7 after 30 min was 99%, 90%, and 99%, respectively, proving that the $\text{La}_2\text{CoO}_{4+\delta}$ /PMS system could be employed to degrade effectively different kind of organic pollutant. Moreover, to detect the applicability of the $\text{La}_2\text{CoO}_{4+\delta}$ /PMS system in real aquatic environments, the effect of various water matrices such as drinking water and taping water on the catalytic activity of $\text{La}_2\text{CoO}_{4+\delta}$ was studied. As depicted in Figure 10b, the removal efficiency of BPA was unremarkably affected in the drinking water sample, whereas the degradation efficiency of BPA was decreased slightly in the tap water sample to 90%. These results suggest that the anions in the water had an insignificant inhibitory effect on the BPA removal.

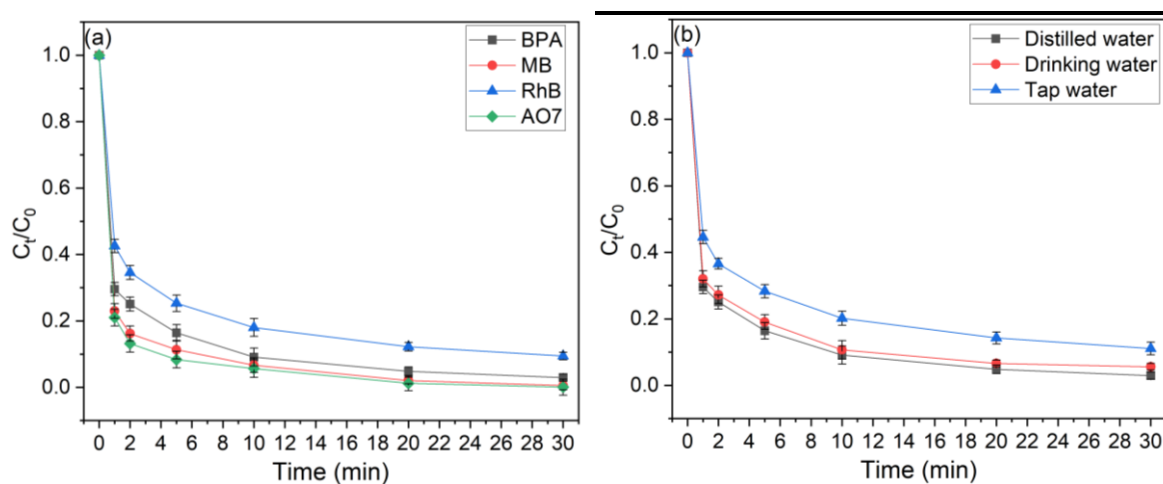


Figure 10. a) The catalytic activity of $\text{La}_2\text{CoO}_{4+\delta}$ a) in the removal of various organics dyes and b) in water matrices.

3.5 Possible degradation pathways

To study the degradation pathway of BPA, the degradation intermediates of BPA via the $\text{La}_2\text{CoO}_{4+\delta}$ /PMS system were identified by LC-MS (see supplementary material, Figure S9). According to the mass spectrometric results (see supplementary material, Table S2), the aromatic and aliphatic intermediates, namely, 2-(4-hydroxyphenyl)-propanol-2-ol, 4-isopropenylphenol, ethanedioic acid, 1,5-hexadiene-3-ol, and trimethylhexane were detected. Mainly, the aromatic ring in BPA is attacked by $\text{SO}_4^{\bullet-}$ or $\cdot\text{OH}$ and converted to 2-(4-hydroxyphenyl)-propanol-2-ol [49] and the attack on the tertiary hydroxyl produces 4-isopropenylphenol. Afterwards, the intermediate products were subsequently attacked to form ethanedioic acid, 1,5-hexadiene-3-ol, and trimethylhexane. Finally, the intermediate products were further oxidized and mineralized into CO_2 and H_2O .

4 Conclusions

In summary, we have demonstrated that $\text{La}_2\text{CoO}_{4+\delta}$ nanoparticles were successfully synthesized via spray-flame synthesis, and applied as novel catalysts for PMS activation. The spray-flame synthesis method has practical advantages such as producing a large amount of $\text{La}_2\text{CoO}_{4+\delta}$ nanoparticles in one step without high-temperature annealing, eco-friendly, and cost-effective. Compared to LaCoO_{3-x} catalyst, $\text{La}_2\text{CoO}_{4+\delta}$ nanoparticles exhibit a faster catalytic activity for BPA oxidation and better stability with less cobalt leaching in the presence of PMS. Such enhancement was attributed to the lower oxidation state of cobalt, fast regeneration of Co^{2+} during PMS activation, and large surface area. Moreover, the removal efficiency maintained 89% after four successive experimental runs reaction. The radicals quenching experiments and electron paramagnetic resonance studies showed that $\text{SO}_4^{\bullet-}$ played a dominant role during the activation of PMS.

1
2
3
4
5
6
7
8
9
10
11
12
13
14
15
16
17
18
19
20
21
22
23
24
25
26
27
28
29
30
31
32
33
34
35
36
37
38
39
40
41
42
43
44
45
46
47
48
49
50
51
52
53
54
55
56
57
58
59
60
61
62
63
64
65

In consideration of cost, this study provides an option to broaden the application of $\text{La}_2\text{CoO}_{4+\delta}$ catalysts for water treatment by PMS activation.

5 References

- [1] C. Erler, J. Novak, Bisphenol A Exposure: Human Risk and Health Policy, *J. Pediatr. Nurs.* 25 (2010) 400–407. <https://doi.org/https://doi.org/10.1016/j.pedn.2009.05.006>.
- [2] A. Schecter, N. Malik, D. Haffner, S. Smith, T.R. Harris, O. Paepke, L. Birnbaum, Bisphenol A (BPA) in U.S. Food, *Environ. Sci. Technol.* 44 (2010) 9425–9430. <https://doi.org/10.1021/es102785d>.
- [3] Y. Yoon, P. Westerhoff, S.A. Snyder, E.C. Wert, Nanofiltration and ultrafiltration of endocrine disrupting compounds, pharmaceuticals and personal care products, *J. Memb. Sci.* 270 (2006) 88–100. <https://doi.org/https://doi.org/10.1016/j.memsci.2005.06.045>.
- [4] M. Hammad, P. Fortugno, S. Hardt, C. Kim, S. Salamon, T.C. Schmidt, H. Wende, C. Schulz, H. Wiggers, Large-scale synthesis of iron oxide/graphene hybrid materials as highly efficient photo-Fenton catalyst for water remediation, *Environ. Technol. Innov.* (2020) 101239. <https://doi.org/https://doi.org/10.1016/j.eti.2020.101239>.
- [5] P. Hu, M. Long, Cobalt-catalyzed sulfate radical-based advanced oxidation: A review on heterogeneous catalysts and applications, *Appl. Catal. B Environ.* 181 (2016) 103–117. <https://doi.org/https://doi.org/10.1016/j.apcatb.2015.07.024>.
- [6] Y. Liu, Y. Wang, Q. Wang, J. Pan, J. Zhang, Simultaneous removal of NO and SO₂ using vacuum ultraviolet light (VUV)/heat/peroxymonosulfate (PMS), *Chemosphere.* 190 (2018) 431–441. <https://doi.org/https://doi.org/10.1016/j.chemosphere.2017.10.020>.

- 1
2
3
4
5
6
7
8
9
10
11
12
13
14
15
16
17
18
19
20
21
22
23
24
25
26
27
28
29
30
31
32
33
34
35
36
37
38
39
40
41
42
43
44
45
46
47
48
49
50
51
52
53
54
55
56
57
58
59
60
61
62
63
64
65
- [7] Z.-H. Diao, Z.-Y. Lin, X.-Z. Chen, L. Yan, F.-X. Dong, W. Qian, L.-J. Kong, J.-J. Du, W. Chu, Ultrasound-assisted heterogeneous activation of peroxymonosulphate by natural pyrite for 2,4-dichlorophenol degradation in water: Synergistic effects, pathway and mechanism, *Chem. Eng. J.* (2019) 123771.
<https://doi.org/https://doi.org/10.1016/j.cej.2019.123771>.
- [8] R. Xie, J. Ji, K. Guo, D. Lei, Q. Fan, D.Y.C. Leung, H. Huang, Wet scrubber coupled with UV/PMS process for efficient removal of gaseous VOCs: Roles of sulfate and hydroxyl radicals, *Chem. Eng. J.* 356 (2019) 632–640.
<https://doi.org/https://doi.org/10.1016/j.cej.2018.09.025>.
- [9] H. Song, L. Yan, Y. Wang, J. Jiang, J. Ma, C. Li, G. Wang, J. Gu, P. Liu, Electrochemically activated PMS and PDS: Radical oxidation versus nonradical oxidation, *Chem. Eng. J.* (2019) 123560.
<https://doi.org/https://doi.org/10.1016/j.cej.2019.123560>.
- [10] B. Bouzayani, E. Rosales, M. Pazos, S.C. Elaoud, M.A. Sanromán, Homogeneous and heterogeneous peroxymonosulfate activation by transition metals for the degradation of industrial leather dye, *J. Clean. Prod.* 228 (2019) 222–230.
<https://doi.org/https://doi.org/10.1016/j.jclepro.2019.04.217>.
- [11] G.P. Anipsitakis, D.D. Dionysiou, Radical Generation by the Interaction of Transition Metals with Common Oxidants, *Environ. Sci. Technol.* 38 (2004) 3705–3712.
<https://doi.org/10.1021/es035121o>.
- [12] F.J. Rivas, O. Gimeno, T. Borallho, Aqueous pharmaceutical compounds removal by potassium monopersulfate. Uncatalyzed and catalyzed semicontinuous experiments, *Chem. Eng. J.* 192 (2012) 326–333.
<https://doi.org/https://doi.org/10.1016/j.cej.2012.03.055>.
- [13] J. Wang, S. Wang, Activation of persulfate (PS) and peroxymonosulfate (PMS) and application for the degradation of emerging contaminants, *Chem. Eng. J.* 334 (2018)

1502–1517. <https://doi.org/https://doi.org/10.1016/j.cej.2017.11.059>.

- 1
2
3
4
5
6
7
8
9
10
11
12
13
14
15
16
17
18
19
20
21
22
23
24
25
26
27
28
29
30
31
32
33
34
35
36
37
38
39
40
41
42
43
44
45
46
47
48
49
50
51
52
53
54
55
56
57
58
59
60
61
62
63
64
65
- [14] E. Saputra, S. Muhammad, H. Sun, H.-M. Ang, M.O. Tadé, S. Wang, A comparative study of spinel structured Mn₃O₄, Co₃O₄ and Fe₃O₄ nanoparticles in catalytic oxidation of phenolic contaminants in aqueous solutions, *J. Colloid Interface Sci.* 407 (2013) 467–473. <https://doi.org/https://doi.org/10.1016/j.jcis.2013.06.061>.
- [15] Y. Yao, Y. Cai, G. Wu, F. Wei, X. Li, H. Chen, S. Wang, Sulfate radicals induced from peroxymonosulfate by cobalt manganese oxides (Co_xMn_{3-x}O₄) for Fenton-Like reaction in water, *J. Hazard. Mater.* 296 (2015) 128–137. <https://doi.org/https://doi.org/10.1016/j.jhazmat.2015.04.014>.
- [16] J.C. Espinosa, P. Manickam-Periyaraman, F. Bernat-Quesada, S. Sivanesan, M. Álvaro, H. García, S. Navalón, Engineering of activated carbon surface to enhance the catalytic activity of supported cobalt oxide nanoparticles in peroxymonosulfate activation, *Appl. Catal. B Environ.* 249 (2019) 42–53. <https://doi.org/https://doi.org/10.1016/j.apcatb.2019.02.043>.
- [17] J. Zhu, H. Li, L. Zhong, P. Xiao, X. Xu, X. Yang, Z. Zhao, J. Li, Perovskite Oxides: Preparation, Characterizations, and Applications in Heterogeneous Catalysis, *ACS Catal.* 4 (2014) 2917–2940. <https://doi.org/10.1021/cs500606g>.
- [18] K.-Y.A. Lin, Y.-C. Chen, Y.-F. Lin, LaMO₃ perovskites (M=Co, Cu, Fe and Ni) as heterogeneous catalysts for activating peroxymonosulfate in water, *Chem. Eng. Sci.* 160 (2017) 96–105. <https://doi.org/https://doi.org/10.1016/j.ces.2016.11.017>.
- [19] X. Pang, Y. Guo, Y. Zhang, B. Xu, F. Qi, LaCoO₃ perovskite oxide activation of peroxymonosulfate for aqueous 2-phenyl-5-sulfobenzimidazole degradation: Effect of synthetic method and the reaction mechanism, *Chem. Eng. J.* 304 (2016) 897–907. <https://doi.org/https://doi.org/10.1016/j.cej.2016.07.027>.
- [20] P. Liang, D. Meng, Y. Liang, Z. Wang, C. Zhang, S. Wang, Z. Zhang, Cation deficiency tuned LaCoO_{3-δ} perovskite for peroxymonosulfate activation towards

- bisphenol A degradation, *Chem. Eng. J.* 409 (2021) 128196.
<https://doi.org/https://doi.org/10.1016/j.cej.2020.128196>.
- [21] X. Duan, C. Su, J. Miao, Y. Zhong, Z. Shao, S. Wang, H. Sun, Insights into perovskite-catalyzed peroxymonosulfate activation: Maneuverable cobalt sites for promoted evolution of sulfate radicals, *Appl. Catal. B Environ.* 220 (2018) 626–634.
<https://doi.org/https://doi.org/10.1016/j.apcatb.2017.08.088>.
- [22] Y. Takeda, R. Kanno, M. Sakano, O. Yamamoto, M. Takano, Y. Bando, H. Akinaga, K. Takita, J.B. Goodenough, Crystal chemistry and physical properties of $\text{La}_{2-x}\text{Sr}_x\text{NiO}_4$ ($0 \leq x \leq 1.6$), *Mater. Res. Bull.* 25 (1990) 293–306.
[https://doi.org/https://doi.org/10.1016/0025-5408\(90\)90100-G](https://doi.org/https://doi.org/10.1016/0025-5408(90)90100-G).
- [23] S.D. Peter, E. Garbowski, N. Guilhaume, V. Perrichon, M. Primet, Catalytic properties of La_2CuO_4 in the CO + NO reaction, *Catal. Letters.* 54 (1998) 79–84.
<https://doi.org/10.1023/A:1019063502409>.
- [24] Y. Huan, S. Chen, R. Zeng, T. Wei, D. Dong, X. Hu, Y. Huang, Intrinsic Effects of Ruddlesden-Popper-Based Bifunctional Catalysts for High-Temperature Oxygen Reduction and Evolution, *Adv. Energy Mater.* 9 (2019) 1901573.
<https://doi.org/https://doi.org/10.1002/aenm.201901573>.
- [25] T. Oshima, T. Yokoi, M. Eguchi, K. Maeda, Synthesis and photocatalytic activity of $\text{K}_2\text{CaNaNb}_3\text{O}_{10}$, a new Ruddlesden–Popper phase layered perovskite, *Dalt. Trans.* 46 (2017) 10594–10601. <https://doi.org/10.1039/C6DT04872B>.
- [26] J. Zhu, Z. Zhao, D. Xiao, J. Li, X. Yang, Y. Wu, CO Oxidation, NO Decomposition, and NO + CO Reduction over Perovskite-like Oxides La_2CuO_4 and $\text{La}_{2-x}\text{Sr}_x\text{CuO}_4$: An MS–TPD Study, *Ind. Eng. Chem. Res.* 44 (2005) 4227–4233.
<https://doi.org/10.1021/ie050317d>.
- [27] R.P. Forslund, C.T. Alexander, A.M. Abakumov, K.P. Johnston, K.J. Stevenson, Enhanced Electrocatalytic Activities by Substitutional Tuning of Nickel-Based

- Ruddlesden–Popper Catalysts for the Oxidation of Urea and Small Alcohols, *ACS Catal.* 9 (2019) 2664–2673. <https://doi.org/10.1021/acscatal.8b04103>.
- [28] J. Choi, S. Park, H. Han, M. Kim, M. Park, J. Han, W.B. Kim, Highly efficient CO₂ electrolysis to CO on Ruddlesden–Popper perovskite oxide with in situ exsolved Fe nanoparticles, *J. Mater. Chem. A.* 9 (2021) 8740–8748. <https://doi.org/10.1039/D0TA11328J>.
- [29] H. Chen, Y. Xu, K. Zhu, H. Zhang, Understanding oxygen-deficient La₂CuO_{4-δ} perovskite activated peroxy monosulfate for bisphenol A degradation: The role of localized electron within oxygen vacancy, *Appl. Catal. B Environ.* 284 (2021) 119732. <https://doi.org/https://doi.org/10.1016/j.apcatb.2020.119732>.
- [30] Ş. Ortatatlı, J. Ternieden, C. Weidenthaler, Low Temperature Formation of Ruddlesden–Popper-Type Layered La₂CoO_{4±δ} Perovskite Monitored via In Situ X-ray Powder Diffraction, *Eur. J. Inorg. Chem.* 2018 (2018) 5238–5245. <https://doi.org/https://doi.org/10.1002/ejic.201801162>.
- [31] X.-K. Gu, E. Nikolla, Design of Ruddlesden–Popper Oxides with Optimal Surface Oxygen Exchange Properties for Oxygen Reduction and Evolution, *ACS Catal.* 7 (2017) 5912–5920. <https://doi.org/10.1021/acscatal.7b01483>.
- [32] S.-Y. Jeon, M.-B. Choi, H.-N. Im, J.-H. Hwang, S.-J. Song, Oxygen ionic conductivity of La₂NiO_{4+δ} via interstitial oxygen defect, *J. Phys. Chem. Solids.* 73 (2012) 656–660. <https://doi.org/https://doi.org/10.1016/j.jpcs.2012.01.006>.
- [33] J. Guo, H. Lou, Y. Zhu, X. Zheng, La-based perovskite precursors preparation and its catalytic activity for CO₂ reforming of CH₄, *Mater. Lett.* 57 (2003) 4450–4455. [https://doi.org/https://doi.org/10.1016/S0167-577X\(03\)00341-0](https://doi.org/https://doi.org/10.1016/S0167-577X(03)00341-0).
- [34] C. Jeong, J.-H. Lee, M. Park, J. Hong, H. Kim, J.-W. Son, J.-H. Lee, B.-K. Kim, K.J. Yoon, Design and processing parameters of La₂NiO_{4+δ}-based cathode for anode-supported planar solid oxide fuel cells (SOFCs), *J. Power Sources.* 297 (2015) 370–

378. <https://doi.org/https://doi.org/10.1016/j.jpowsour.2015.08.023>.

- 1
2
3
4
5
6
7
8
9
10
11
12
13
14
15
16
17
18
19
20
21
22
23
24
25
26
27
28
29
30
31
32
33
34
35
36
37
38
39
40
41
42
43
44
45
46
47
48
49
50
51
52
53
54
55
56
57
58
59
60
61
62
63
64
65
- [35] X. Weng, P. Boldrin, I. Abrahams, S.J. Skinner, J.A. Darr, Direct Syntheses of Mixed Ion and Electronic Conductors $\text{La}_4\text{Ni}_3\text{O}_{10}$ and $\text{La}_3\text{Ni}_2\text{O}_7$ from Nanosized Coprecipitates, *Chem. Mater.* 19 (2007) 4382–4384.
<https://doi.org/10.1021/cm070134c>.
- [36] S.J. Kim, T. Akbay, J. Matsuda, A. Takagaki, T. Ishihara, Strain Effects on Oxygen Reduction Activity of Pr_2NiO_4 Caused by Gold Bulk Dispersion for Low Temperature Solid Oxide Fuel Cells, *ACS Appl. Energy Mater.* 2 (2019) 1210–1220.
<https://doi.org/10.1021/acsaem.8b01776>.
- [37] D. Waffel, B. Alkan, Q. Fu, Y.-T. Chen, S. Schmidt, C. Schulz, H. Wiggers, M. Muhler, B. Peng, Towards Mechanistic Understanding of Liquid-Phase Cinnamyl Alcohol Oxidation with tert-Butyl Hydroperoxide over Noble-Metal-Free $\text{LaCo}_{1-x}\text{Fe}_x\text{O}_3$ Perovskites, *Chempluschem.* 84 (2019) 1155–1163.
<https://doi.org/10.1002/cplu.201900429>.
- [38] S. Angel, J. Neises, M. Dreyer, K. Friedel Ortega, M. Behrens, Y. Wang, H. Arandiyán, C. Schulz, H. Wiggers, Spray-flame synthesis of $\text{La}(\text{Fe}, \text{Co})\text{O}_3$ nanoperoovskites from metal nitrates, *AIChE J.* 66 (2020) e16748.
<https://doi.org/10.1002/aic.16748>.
- [39] B. Alkan, S. Cychy, S. Varhade, M. Muhler, C. Schulz, W. Schuhmann, H. Wiggers, C. Andronescu, Spray-Flame-Synthesized $\text{LaCo}_{1-x}\text{Fe}_x\text{O}_3$ Perovskite Nanoparticles as Electrocatalysts for Water and Ethanol Oxidation, *ChemElectroChem.* 6 (2019) 4266–4274. <https://doi.org/10.1002/celec.201900168>.
- [40] F. Schneider, S. Suleiman, J. Menser, E. Borukhovich, I. Wlokas, A. Kempf, H. Wiggers, C. Schulz, SpraySyn—A standardized burner configuration for nanoparticle synthesis in spray flames, *Rev. Sci. Instrum.* 90 (2019) 85108.
<https://doi.org/10.1063/1.5090232>.

- 1
2
3
4
5
6
7
8
9
10
11
12
13
14
15
16
17
18
19
20
21
22
23
24
25
26
27
28
29
30
31
32
33
34
35
36
37
38
39
40
41
42
43
44
45
46
47
48
49
50
51
52
53
54
55
56
57
58
59
60
61
62
63
64
65
- [41] A. Grimaud, F. Mauvy, J.M. Bassat, S. Fourcade, L. Rocheron, M. Marrony, J.C. Grenier, Hydration Properties and Rate Determining Steps of the Oxygen Reduction Reaction of Perovskite-Related Oxides as H⁺-SOFC Cathodes, *J. Electrochem. Soc.* 159 (2012) B683–B694. <https://doi.org/10.1149/2.101205jes>.
- [42] L. Armelao, M. Bettinelli, G. Bottaro, D. Barreca, E. Tondello, LaCoO₃ Nanopowders by XPS, *Surf. Sci. Spectra.* 8 (2001) 24–31. <https://doi.org/10.1116/11.20010701>.
- [43] M.C. Biesinger, B.P. Payne, A.P. Grosvenor, L.W.M. Lau, A.R. Gerson, R.S.C. Smart, Resolving surface chemical states in XPS analysis of first row transition metals, oxides and hydroxides: Cr, Mn, Fe, Co and Ni, *Appl. Surf. Sci.* 257 (2011) 2717–2730. <https://doi.org/https://doi.org/10.1016/j.apsusc.2010.10.051>.
- [44] P.H.T. Ngamou, K. Kohse-Höinghaus, N. Bahlawane, CO and ethanol oxidation over LaCoO₃ planar model catalysts: Effect of the thickness, *Catal. Commun.* 12 (2011) 1344–1350. <https://doi.org/https://doi.org/10.1016/j.catcom.2011.04.029>.
- [45] S. Pegoraro, M.M. Natile, A. Galenda, A. Glisenti, La₂Cu_{0.8}Co_{0.2}O_{4+δ} by Pechini Method, *Surf. Sci. Spectra.* 16 (2009) 75–82. <https://doi.org/10.1116/11.20090201>.
- [46] X. Duan, C. Su, L. Zhou, H. Sun, A. Suvorova, T. Odedairo, Z. Zhu, Z. Shao, S. Wang, Surface controlled generation of reactive radicals from persulfate by carbocatalysis on nanodiamonds, *Appl. Catal. B Environ.* 194 (2016) 7–15. <https://doi.org/https://doi.org/10.1016/j.apcatb.2016.04.043>.
- [47] L. Wu, Y. Yu, Q. Zhang, J. Hong, J. Wang, Y. She, A novel magnetic heterogeneous catalyst oxygen-defective CoFe₂O_{4-x} for activating peroxymonosulfate, *Appl. Surf. Sci.* 480 (2019) 717–726. <https://doi.org/https://doi.org/10.1016/j.apsusc.2019.03.034>.
- [48] Y. Liu, R. Luo, Y. Li, J. Qi, C. Wang, J. Li, X. Sun, L. Wang, Sandwich-like Co₃O₄/MXene composite with enhanced catalytic performance for Bisphenol A degradation, *Chem. Eng. J.* 347 (2018) 731–740. <https://doi.org/https://doi.org/10.1016/j.cej.2018.04.155>.

- 1
2
3
4
5
6
7
8
9
10
11
12
13
14
15
16
17
18
19
20
21
22
23
24
25
26
27
28
29
30
31
32
33
34
35
36
37
38
39
40
41
42
43
44
45
46
47
48
49
50
51
52
53
54
55
56
57
58
59
60
61
62
63
64
65
- [49] X. Li, Z. Wang, B. Zhang, A.I. Rykov, M.A. Ahmed, J. Wang, $\text{Fe}_x\text{Co}_{3-x}\text{O}_4$ nanocages derived from nanoscale metal–organic frameworks for removal of bisphenol A by activation of peroxymonosulfate, *Appl. Catal. B Environ.* 181 (2016) 788–799. <https://doi.org/https://doi.org/10.1016/j.apcatb.2015.08.050>.
- [50] X. Li, A.I. Rykov, B. Zhang, Y. Zhang, J. Wang, Graphene encapsulated Fe_xCo_y nanocages derived from metal–organic frameworks as efficient activators for peroxymonosulfate, *Catal. Sci. Technol.* 6 (2016) 7486–7494. <https://doi.org/10.1039/C6CY01479H>.
- [51] C. Wang, H. Wang, R. Luo, C. Liu, J. Li, X. Sun, J. Shen, W. Han, L. Wang, Metal-organic framework one-dimensional fibers as efficient catalysts for activating peroxymonosulfate, *Chem. Eng. J.* 330 (2017) 262–271. <https://doi.org/https://doi.org/10.1016/j.cej.2017.07.156>.
- [52] L. Hu, G. Zhang, Q. Wang, Y. Sun, M. Liu, P. Wang, Facile synthesis of novel Co_3O_4 - Bi_2O_3 catalysts and their catalytic activity on bisphenol A by peroxymonosulfate activation, *Chem. Eng. J.* 326 (2017) 1095–1104. <https://doi.org/https://doi.org/10.1016/j.cej.2017.05.168>.
- [53] R. Luo, C. Liu, J. Li, C. Wang, X. Sun, J. Shen, W. Han, L. Wang, Convenient synthesis and engineering of ultrafine Co_3O_4 -incorporated carbon composite: towards practical application of environmental remediation, *J. Mater. Chem. A.* 6 (2018) 3454–3461. <https://doi.org/10.1039/C7TA11052A>.
- [54] R. Zhang, Y. Wan, J. Peng, G. Yao, Y. Zhang, B. Lai, Efficient degradation of atrazine by $\text{LaCoO}_3/\text{Al}_2\text{O}_3$ catalyzed peroxymonosulfate: Performance, degradation intermediates and mechanism, *Chem. Eng. J.* 372 (2019) 796–808. <https://doi.org/https://doi.org/10.1016/j.cej.2019.04.188>.
- [55] X. ZHANG, C. HE, L. WANG, J. LIU, M. DENG, Q. FENG, Non-isothermal kinetic analysis of thermal dehydration of $\text{La}_2(\text{CO}_3)_3 \cdot 3.4\text{H}_2\text{O}$ in air, *Trans. Nonferrous Met.*

- Soc. China. 24 (2014) 3378–3385. [https://doi.org/https://doi.org/10.1016/S1003-6326\(14\)63480-4](https://doi.org/https://doi.org/10.1016/S1003-6326(14)63480-4).
- [56] S. Lu, G. Wang, S. Chen, H. Yu, F. Ye, X. Quan, Heterogeneous activation of peroxymonosulfate by $\text{LaCo}_{1-x}\text{Cu}_x\text{O}_3$ perovskites for degradation of organic pollutants, *J. Hazard. Mater.* 353 (2018) 401–409. <https://doi.org/10.1016/j.jhazmat.2018.04.021>.
- [57] C. Su, X. Duan, J. Miao, Y. Zhong, W. Zhou, S. Wang, Z. Shao, Mixed Conducting Perovskite Materials as Superior Catalysts for Fast Aqueous-Phase Advanced Oxidation: A Mechanistic Study, *ACS Catal.* 7 (2017) 388–397. <https://doi.org/10.1021/acscatal.6b02303>.
- [58] X. Tian, P. Gao, Y. Nie, C. Yang, Z. Zhou, Y. Li, Y. Wang, A novel singlet oxygen involved peroxymonosulfate activation mechanism for degradation of ofloxacin and phenol in water, *Chem. Commun.* 53 (2017) 6589–6592. <https://doi.org/10.1039/C7CC02820B>.
- [59] P. Neta, R.E. Huie, A.B. Ross, Rate Constants for Reactions of Inorganic Radicals in Aqueous Solution, *J. Phys. Chem. Ref. Data.* 17 (1988) 1027–1284. <https://doi.org/10.1063/1.555808>.
- [60] G.P. Anipsitakis, D.D. Dionysiou, Degradation of Organic Contaminants in Water with Sulfate Radicals Generated by the Conjunction of Peroxymonosulfate with Cobalt, *Environ. Sci. Technol.* 37 (2003) 4790–4797. <https://doi.org/10.1021/es0263792>.
- [61] R. Luo, M. Li, C. Wang, M. Zhang, M.A. Nasir Khan, X. Sun, J. Shen, W. Han, L. Wang, J. Li, Singlet oxygen-dominated non-radical oxidation process for efficient degradation of bisphenol A under high salinity condition, *Water Res.* 148 (2019) 416–424. <https://doi.org/https://doi.org/10.1016/j.watres.2018.10.087>.
- [62] X. Dong, B. Ren, Z. Sun, C. Li, X. Zhang, M. Kong, S. Zheng, D.D. Dionysiou, Monodispersed CuFe_2O_4 nanoparticles anchored on natural kaolinite as highly

- 1
2
3
4
5
6
7
8
9
10
11
12
13
14
15
16
17
18
19
20
21
22
23
24
25
26
27
28
29
30
31
32
33
34
35
36
37
38
39
40
41
42
43
44
45
46
47
48
49
50
51
52
53
54
55
56
57
58
59
60
61
62
63
64
65
- efficient peroxymonosulfate catalyst for bisphenol A degradation, *Appl. Catal. B Environ.* 253 (2019) 206–217.
<https://doi.org/https://doi.org/10.1016/j.apcatb.2019.04.052>.
- [63] A.F. Lucrédio, G.T. Filho, E.M. Assaf, Co/Mg/Al hydrotalcite-type precursor, promoted with La and Ce, studied by XPS and applied to methane steam reforming reactions, *Appl. Surf. Sci.* 255 (2009) 5851–5856.
<https://doi.org/https://doi.org/10.1016/j.apsusc.2009.01.020>.
- [64] Z. Shao, S.M. Haile, A high-performance cathode for the next generation of solid-oxide fuel cells, *Nature*. 431 (2004) 170–173. <https://doi.org/10.1038/nature02863>.
- [65] S. Baumann, F. Schulze-Küppers, S. Roitsch, M. Betz, M. Zwick, E.M. Pfaff, W.A. Meulenber, J. Mayer, D. Stöver, Influence of sintering conditions on microstructure and oxygen permeation of Ba_{0.5}Sr_{0.5}Co_{0.8}Fe_{0.2}O_{3-δ} (BSCF) oxygen transport membranes, *J. Memb. Sci.* 359 (2010) 102–109.
<https://doi.org/https://doi.org/10.1016/j.memsci.2010.02.002>.
- [66] M.M. Kuklja, E.A. Kotomin, R. Merkle, Y.A. Mastrikov, J. Maier, Combined theoretical and experimental analysis of processes determining cathode performance in solid oxide fuel cells, *Phys. Chem. Chem. Phys.* 15 (2013) 5443–5471.
<https://doi.org/10.1039/C3CP44363A>.
- [67] Y. Huang, C. Han, Y. Liu, M.N. Nadagouda, L. Machala, K.E. O’Shea, V.K. Sharma, D.D. Dionysiou, Degradation of atrazine by Zn_xCu_{1-x}Fe₂O₄ nanomaterial-catalyzed sulfite under UV–vis light irradiation: Green strategy to generate SO₄⁻, *Appl. Catal. B Environ.* 221 (2018) 380–392.
<https://doi.org/https://doi.org/10.1016/j.apcatb.2017.09.001>.
- [68] Y. Feng, P.-H. Lee, D. Wu, K. Shih, Surface-bound sulfate radical-dominated degradation of 1,4-dioxane by alumina-supported palladium (Pd/Al₂O₃) catalyzed peroxymonosulfate, *Water Res.* 120 (2017) 12–21.

1
2
3
4
5
6
7
8
9
10
11
12
13
14
15
16
17
18
19
20
21
22
23
24
25
26
27
28
29
30
31
32
33
34
35
36
37
38
39
40
41
42
43
44
45
46
47
48
49
50
51
52
53
54
55
56
57
58
59
60
61
62
63
64
65

<https://doi.org/https://doi.org/10.1016/j.watres.2017.04.070>.

- [69] H. V Lutze, N. Kerlin, T.C. Schmidt, Sulfate radical-based water treatment in presence of chloride: Formation of chlorate, inter-conversion of sulfate radicals into hydroxyl radicals and influence of bicarbonate, *Water Res.* 72 (2015) 349–360.

<https://doi.org/https://doi.org/10.1016/j.watres.2014.10.006>.

Enhanced heterogeneous activation of peroxymonosulfate by Ruddlesden-Popper-type $\text{La}_2\text{CoO}_{4+\delta}$ nanoparticles for bisphenol A degradation

Mohaned Hammad^{a*}, Baris Alkan^a, Ahmed K. Al-kamal^a, Cheolyong Kim^b, Md Yusuf Ali^a, Steven Angel^a, Haakon T. A. Wiedemann^c, Dina Klippert^c, Torsten C. Schmidt^b, Christopher W. M. Kay^{c,d}, Hartmut Wiggers^{a,e*}

^a IVG, Institute for Combustion and Gas Dynamics – Reactive Fluids, University of Duisburg-Essen, Duisburg, Germany

^b Instrumental Analytical Chemistry and Centre for Water and Environmental Research, University of Duisburg-Essen, Essen, Germany

^c Department of Chemistry, Saarland University, Saarbrücken, Germany

^d London Centre for Nanotechnology, University College London, 17-19 Gordon Street, London WC1H 0AH, United Kingdom

^e CENIDE, Center for Nanointegration Duisburg-Essen, University of Duisburg-Essen, Duisburg, Germany

Corresponding authors:

Dr. Mohaned Hammad*

Prof. Hartmut Wiggers*

Institute for Combustion and Gas Dynamics – Reactive Fluids

University of Duisburg-Essen

Carl-Benz-Str. 199

47057 Duisburg, Germany

mohaned.hammad@uni-due.de

hartmut.wiggers@uni-due.de

Abstract

The scalable synthesis of stable catalysts for environmental remediation applications remains challenging. Nonetheless, metal leaching is a serious environmental issue hindering the practical application of transition-metal based catalysts including Co-based catalysts. Herein, for the first time, we describe a facile one-step and scalable spray-flame synthesis of high surface area $\text{La}_2\text{CoO}_{4+\delta}$ nanoparticles containing excess oxygen interstitials ($+\delta$) and use them as a stable and efficient catalyst for activating peroxymonosulfate (PMS) towards the degradation of bisphenol A. Importantly, the $\text{La}_2\text{CoO}_{4+\delta}$ catalyst exhibits higher catalytic degradation of bisphenol A (95% in 20 minutes) and stability than LaCoO_{3-x} nanoparticles (60%) in the peroxymonosulfate activation system. The high content of Co^{2+} in the structure showed a strong impact on the catalytic performance of the $\text{La}_2\text{CoO}_{4+\delta}$ +PMS system. Despite its high specific surface area, our results showed a very low amount of leached cobalt (less than 0.04 mg/L in 30 minutes), distinguishing it as a material with high chemical stability. According to the radical quenching experiments and the electron paramagnetic resonance technology, $\text{SO}_4^{\bullet-}$, $\cdot\text{OH}$, and $^1\text{O}_2$ were generated and $\text{SO}_4^{\bullet-}$ played a dominant role in bisphenol A degradation. Moreover, the $\text{La}_2\text{CoO}_{4+\delta}$ +PMS system maintained conspicuous catalytic performance for the degradation of other organic pollutants including methyl orange, rhodamine B, and methylene blue. Overall, our results showed that we developed a new synthesis method for stable $\text{La}_2\text{CoO}_{4+\delta}$ nanoparticles that can be used as a highly active heterogeneous catalyst for PMS-assisted oxidation of organic pollutants.

Keywords: heterogeneous catalysis, spray flame synthesis, peroxymonosulfate, sulfate radical, bisphenol A degradation.

1 Introduction

Bisphenol A (2,2-bis (4-hydroxyphenyl) propane, BPA) is intensively utilized as a key industrial chemical for the production of polycarbonate plastics and epoxy resins in the plastic industry [1]. Unfortunately, a significant amount of BPA is continuously discharged into the environment and detected in food, drinking water, and aquatic animals [2]. BPA mimics estrogenic activity in human and animal bodies causing disruption of the endocrine system through interfering with hormonal and homeostatic functions [3]. Therefore, the removal of BPA especially from aquatic environments is of great interest.

Recently, the Fenton reaction employing hydroxyl ($\cdot\text{OH}$) and sulfate radicals ($\text{SO}_4^{\cdot-}$) has attracted increasing interest as a promising method to oxidize organic pollutant in water [4–6]. Compared to the $\cdot\text{OH}$, $\text{SO}_4^{\cdot-}$ has a longer half-life time, higher standard oxidation potential, and wider pH range applicability, which is more efficient for bisphenol A degradation [7]. Sulfate radicals are typically generated by peroxymonosulfate (PMS) or peroxydisulfate (PDS) activation using heat [8], ultrasound [9], UV [10], electrochemical processes [11], and transition metal ions (e.g., Co, Mn, Cu, Fe, and Ni) [12].

Homogenous transition-metal catalysis is one of the feasible and cost-effective ways to generate $\text{SO}_4^{\cdot-}$. Among the transition metals, Co^{2+} exhibits the most efficient homogeneous catalyst for PMS activation [13] and is catalytically regenerated during PMS activation, which enhances its catalytic activity [14]. However, Co-based homogeneous activation has serious drawbacks, especially secondary metal-ion pollution and high catalyst consumption [15]. Thus, heterogeneous, Co-based catalysts such as cobalt oxide [16], cobalt-based bimetallic oxide [17,18], and supported cobalt oxide [19] nanoparticles have been investigated for PMS activation. Among them, transition metal-based perovskites (ABO_3 with B being the transition metal) have attracted increasing attention in heterogeneous catalysis because of their flexibility in chemical composition and their ability for generating oxygen vacancies, thus enabling

catalytic redox reactions [20]. More recently, some reports have focused on different transition metals La-based perovskites (LaMO_3 (M: Co, Cu, Fe, and Ni)) for PMS activation [21]. Particularly, LaCoO_3 perovskites have been considered being very effective to generate $\text{SO}_4^{\cdot-}$ from PMS as Co–O– bonds enable a high number of reactive sites for PMS activation [22]. Moreover, the B-site cation deficiency in the $\text{LaCoO}_{3-\delta}$ perovskite structures enhances their catalytic activity [23]. Although these perovskite catalysts have some advantages such as high catalytic activity, they suffer from metal leaching in the aqueous medium [24]. Thus, it is essential to explore highly stable heterogeneous catalysts for PMS activation.

Compared to transition metal-based perovskites (ABO_3), Ruddlesden-Popper mixed oxides (A_2BO_4) nanoparticles (RP-MONp) exhibit higher stability and redox ability, because their crystal structure is more opened due to extra space between A-site atoms. They consist of alternating layers of perovskite (ABO_3) and rock salt (AO) [25]. These layered structures possess good thermal stability [26] and show high ionic conductivity. Several studies on RP-based catalysts show that the RP-MONp reveal better oxygen diffusion coefficients and surface exchange than other ABO_3 perovskite type. They have been reported as catalysts in various heterogeneously catalyzed reactions including oxygen reduction reaction (ORR) and oxygen evolution reaction (OER) [27], photocatalytic water splitting [28], NO and CO removal [29], oxidation of urea and small alcohols [30], as a cathode for a solid oxide electrolysis cell [31], and as a catalyst in the Fenton reaction [32]. In this regard, $\text{La}_2\text{CoO}_{4+\delta}$ has been selected to be used as a PMS activator since its structure can tolerate excess amounts of oxygen upon oxidation at room temperature up to a δ of 0.16 [33]. Moreover, the oxidation state of the B-site cation in this structure can be controlled by tailoring oxygen non-stoichiometry [34]. To summarize, $\text{La}_2\text{CoO}_{4+\delta}$ is a highly suitable material for advanced catalytic oxidation processes. Several methods have been demonstrated to synthesize Ruddlesden-Popper mixed oxide catalysts including co-precipitation [35], sol-gel synthesis [36], combustion methods [37], hydrothermal flow synthesis [38], and solid-state reactions [39]. However, all these methods

require high-temperature annealing (≥ 1000 °C) at an extended period, which promotes particle growth and sintering, leading to a reduced catalytically active surface area. As an alternative, spray-flame synthesis is an established method to produce non-sintered, homogeneously distributed perovskite nanoparticles down to 10 nm, and even below [40,41]. Surface-sensitive measurements of spray-flame-synthesized LaCoO_3 nanoparticles show a high content of Co^{2+} ions being present at the particles' surface. These results are attributed to the local formation of oxygen-deficient or layered perovskite structures such as A_2BO_4 type Ruddlesden-Popper structures, which can stabilize Co^{2+} much better than the pure perovskite ABO_3 [42]. Thus, specific interest is in the targeted formation and investigation of Co-containing Ruddlesden-Popper-type nanoparticles as highly active heterogeneous catalysts.

Herein, the objective of this study is to seek a one-step method for the synthesis of $\text{La}_2\text{CoO}_{4+\delta}$ nanoparticles using a spray-flame method with the purpose of improving their catalytic performance with a very low amount of metal leaching to achieve the environmental requirements in respect of organic pollutant degradation. The performance of the catalysts for PMS activation was evaluated in terms of BPA degradation. Moreover, effects of several important parameters such as initial pH value, inorganic anions (such as Cl^- , NO_3^- , H_2PO_4^- , HCO_3^- , etc.), and water bodies (tap water, and drinking water) on their catalytic performances along with the reusability of the $\text{La}_2\text{CoO}_{4+\delta}$ nanoparticles were also investigated. The radical generation was identified by radical scavenging experiments and electron paramagnetic resonance studies, and a mechanism for PMS activation is proposed.

2 Materials and methods

2.1 Materials

For the synthesis of $\text{La}_2\text{CoO}_{4+\delta}$ nanoparticles, $\text{La}(\text{CH}_3\text{COO})_3 \cdot 1.05 \text{H}_2\text{O}$ (99.9%; Sigma-Aldrich) and $\text{Co}(\text{CH}_3\text{COO})_2 \cdot 4 \text{H}_2\text{O}$ ($\geq 98\%$; Sigma-Aldrich) were used as the metal precursors

while propionic acid (ACS reagent, >99.5%; Sigma-Aldrich), propanol (anhydrous, 99.7%; Sigma-Aldrich), ultrapure DI water (18.2 MΩ cm at 25 °C) and ethanol (>99.8%; Sigma-Aldrich) were employed as solvents. 5,5-dimethyl-1-pyrroline N-oxide (DMPO) (>97.0%; TCI), Bisphenol A (≥99%), potassium peroxymonosulfate, sodium phosphate monobasic (≥99%), sodium nitrate (≥99%), sodium chloride (≥99%), sodium hydrogencarbonate (≥99%), β-carotene (≥95%), tert-butyl alcohol (≥99.5%), methylene blue (≥ 97%), rhodamine B (≥ 95%), Acid Orange 7 (≥ 98%) potassium bicarbonate (≥99.5%), potassium iodide (≥90%), and absolute ethanol were purchased from Sigma Aldrich to be used for the catalytic tests. Sodium hydroxide (≥97%) and nitric acid (>69%, both VWR International) were used to adjust the pH of the respective solution. All chemicals were used as received without further purification.

2.2 Synthesis of $\text{La}_2\text{CoO}_{4+\delta}$ nanoparticles

The spray-flame syntheses of lattice-oxygen-deficient LaCoO_{3-x} perovskite and interstitial-oxygen-rich $\text{La}_2\text{CoO}_{4+\delta}$ Ruddlesden-Popper phases were carried out similar to the process described before [43] (Figure 1) using precursor solutions and process parameters given in detail in Table S1. Briefly, a precursor solution is transferred to a syringe pump connected to a homemade enclosed reactor, which allows full control of gas flow and pressure. The syringe pump is connected to a hollow needle (0.4 mm inner diameter and 0.7 mm outer diameter) adjusted in the center of a burner nozzle. Oxygen dispersion gas (introduced through an annular gap surrounding the hollow needle) was used to atomize the precursor solution injected into the reactor at a precursor solution flow rate of 3 mL/min. A premixed pilot flame (CH_4/O_2) surrounding the hollow needle was used to ignite and stabilize the spray-flame while a sheath gas surrounding the flame was used to stabilize the reactor gas flow. The reactor was operated at pressures of 930 and 900 mbar, respectively, adjusted by a valve and a rotary vane pump. The formed particles were collected on a filter membrane.

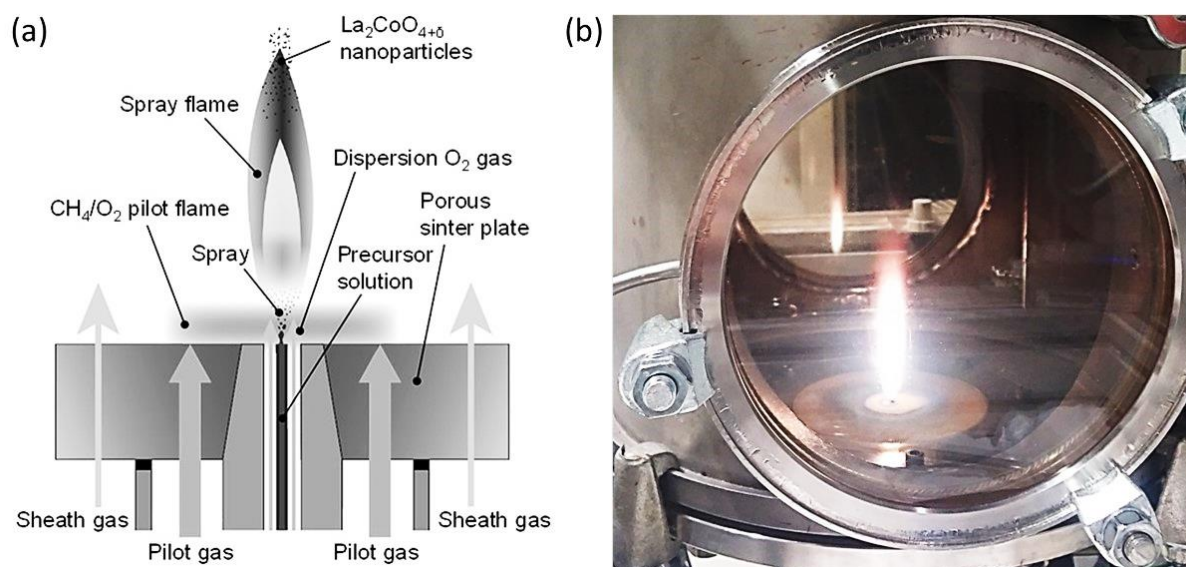


Figure 1. (a) Schematics of the spray-flame synthesis (adapted from Ref [43]) and (b) a photo of the spray-flame during nanoparticle synthesis.

To investigate the influence of cobalt oxidation states on PMS oxidation, we aimed to synthesize two types of catalysts: LaCoO₃ perovskites with mostly Co³⁺ surface ions, and the newly investigated La₂CoO₄ compounds containing a high number of Co²⁺ ions. Thus, for the formation of almost stoichiometric LaCoO₃, the process and combustion parameters were adjusted to lean conditions using low hydrocarbon chained components as solvent (i.e. propanol and propionic acid), a high volume flow of the CH₄/O₂ pilot flame, and a high volume flow of O₂ dispersion gas. The product is labeled “LaCoO_{3-x}“. For the new synthesis of La₂CoO_{4+δ} developed in the course of these investigations, fuel-rich combustion conditions were employed as a strategy to efficiently obtain a cobalt oxidation state of Co²⁺ in the nanoparticle product. For this reason, a high carbon chained carboxylic acid was used in the precursor solution as well as lower volume flows of the CH₄/O₂ pilot flame gases and the O₂ dispersion gas.

The precursor solution for LaCoO_{3-x} was composed of propionic acid mixed with 1-propanol in a glass flask at room temperature and stirred for 10 min. La- and Co-precursors were subsequently added to the solvent mixture and the flask was then heated in a silicon oil bath at 60°C to dissolve the precursors under constant magnetic stirring for 2 h. The total metal

concentration of La and Co was adjusted to 0.45 M and the nominal atomic ratios of La/Co were adjusted to 1. For the precursor solution of $\text{La}_2\text{CoO}_{4+\delta}$, a similar procedure was used except that octanoic acid was used as an organic acid and a small amount of water was added to the solvent mixture to appropriately dissolve the La-acetate. The precursor solution was then heated in a silicon oil bath at 70°C under constant magnetic stirring for 2 h. The total metal concentration of La and Co was adjusted to 0.15 M and the nominal atomic ratios of La/Co were adjusted to 2.

2.3 Methods of Characterization

The crystal phases of the samples were determined by X-ray diffraction (XRD) recorded with a PANalytical X-ray diffractometer X'Pert (Netherlands) with a Cu K_α radiation ($\lambda = 1.5406$ Å). The surface morphology and energy dispersive spectra were analyzed using transmission electron microscopy (TEM, JEM-2200FS, JEOL, Japan). X-ray photoelectron spectroscopy (XPS, VersaProbe II, ULVAC-PHI, Japan with monochromatic Al K_α light at an emission angle of 45°) was applied to analyze the surface elemental composition and chemical state of the samples. All measured binding energies were referenced to the Cu2p peak at 933 eV. Attenuated total reflectance Fourier transform infrared spectra (ATR-FTIR) were recorded using a Bruker Vertex 80 spectrometer (Bruker, Germany) in the 400-4000 cm^{-1} region. The zeta potential of the catalysts was determined by a Malvern Zetasizer (Malvern Panalytical, United Kingdom). The specific surface areas were measured on a Quantachrome NOVA2200 (Quantachrome GmbH, Germany) analyzer at 77 K by the Brunauer–Emmett–Teller (BET) Nitrogen adsorption/desorption isotherm method.

2.4 Catalytic studies and analyses

The catalytic performance of the as-prepared $\text{La}_2\text{CoO}_{4+\delta}$ nanoparticles was evaluated for PMS activation in terms of BPA degradation. The concentration of BPA was analyzed by high-performance liquid chromatography (HPLC, Shimadzu LC-10AT, Shimadzu Corporation, Japan). The HPLC was equipped with an SPD-M10A diode array detector (detection wavelength: 230 nm) and a Kinetex C18 reverse-phase column (100 mm \times 2 mm, 5 μm). The flow rate of the mobile phase consisting of 0.1% formic acid in water and acetonitrile (80:20, v:v) was 0.5 mL/min. In a typical experiment, 2.4 mg catalyst was initially dispersed into 40 mL BPA aqueous solution (40 mg/L) at 25 $^\circ\text{C}$ and the resultant suspension was magnetically stirred in dark for 30 min to ensure the establishment of an adsorption/desorption equilibrium between catalyst and BPA before a certain dose of PMS was added. At selected time intervals, 2 mL of the suspension was withdrawn, immediately quenched with 0.5 mL methanol, filtered with a 0.22 μm membrane filter, centrifuged (12000 rpm, 20 min) to remove the particles, and injected into the HPLC vial. 1.0 M solutions of NaOH and HNO_3 were used to adjust the initial pH. The same operation was repeated with different organic compounds such as methylene blue (MB), rhodamine B (RhB), and acid orange 7 (AO7). The concentrations of MB, RhB, and AO7 were measured by UV-Vis spectroscopy (Varian Cary 400, Varian, Australia) at wavelengths of 664, 553, and 483 nm, respectively. **To study the reusability of the $\text{La}_2\text{CoO}_{4+\delta}$ nanoparticles, the catalyst was collected by centrifugation (Sigma 3-30KS centrifuge, Sigma Laborzentrifugen GmbH, Germany) at 14000 rpm for 10 min, followed by thorough washing with deionized water and then re-dispersed into fresh BPA solution for the next experimental run.**

To compare the degradation reaction kinetics of the BPA degradation, pseudo-first-order kinetics reaction rate constants (k_{app}) of the BPA removal were measured according to the following equation:

$$\ln \left(\frac{C_t}{C_0} \right) = -k_{\text{app}} t \text{ (equation 1)}$$

where C_t depicts the pollutant concentration at time, C_0 is the initial pollutant concentration, k_{app} is the kinetics rate constants, and t is the time.

The concentration of dissolved metal ions in concentrated nitric acid (60%) was determined by atomic absorption spectroscopy (M-Serie, Thermo Electron Corporation, Germany). The total organic carbon (TOC) concentration was analyzed by using a TOC-L total organic carbon analyzer (Shimadzu, Japan) to evaluate the degree of BPA mineralization. To determine the residual concentration of PMS, 100 μL of the suspension was withdrawn at given time intervals, mixed with potassium bicarbonate (5 g/L) and potassium iodide (40 g/L), and then was measured by UV-Vis spectroscopy (Varian Cary 400, Varian, Australia) at a wavelength of 352 nm. To evaluate the contributions of the radical reactions to mineralization, a certain amount of ethanol (EtOH), tert-butyl alcohol (TBA), and β -carotene were added to the catalytic system to scavenge $\text{SO}_4^{\cdot-}$ and $\cdot\text{OH}$, $\cdot\text{OH}$, and $^1\text{O}_2$ respectively. The β -carotene experiment was conducted in 37 mL of acetone and 3 mL of deionized water for dissolving PMS. The intermediates of BPA degradation were identified by an Agilent 1260 Infinity II Liquid Chromatography (LC-MS) system equipped with a 6120 Quadrupole Mass Detector and a Kinetex C18 reverse-phase column (100 mm \times 2 mm, 5 μm). The mobile phase of LC-MS was the same as HPLC. The generated reactive radicals were measured using the MiniScope MS-5000 electron spin resonance spectrometer (Freiberg Instruments, Germany) with a microwave power of 10 mW and a modulation amplitude of 0.2 G at room temperature. The impedance measurements were performed using an impedance analyzer Solartron 1260 (Solartron Analytical, United Kingdom) with a frequency range of 0.1 Hz – 1 MHz and with an output signal voltage of 100 mV. Gold sputtering was done on both sides of the pellet before the experiment.

3 Results and discussion

3.1 Characterization of $\text{La}_2\text{CoO}_{4+\delta}$ nanoparticles

The XRD patterns of the pristine nanoparticles were analyzed to determine crystalline phases of $\text{La}_2\text{CoO}_{4+\delta}$ and LaCoO_{3-x} (Figure 2). The LaCoO_{3-x} diffraction peaks show a good match to a $\text{LaCoO}_{2.937}$ perovskite phase (Inorganic Crystal Structure Database (ICSD): 153995), while the XRD pattern of $\text{La}_2\text{CoO}_{4+\delta}$ can be mainly related to a Ruddlesden-Popper type phase of $\text{La}_2\text{CoO}_{4.13}$ (ICSD: 237238) with a minor content of $\text{La}(\text{OH})_3$ (ICSD: 31584). Notably, the diffraction peaks of $\text{La}_2\text{CoO}_{4+\delta}$ appear more broadened compared to those of LaCoO_{3-x} , and this finding points out a low degree of crystallinity and/or small crystal sizes of $\text{La}_2\text{CoO}_{4+\delta}$. A possible decrease in the crystallinity of the $\text{La}_2\text{CoO}_{4+\delta}$ phase can be owing to hydrated groups incorporated in its structure as previously reported in Co-based Ruddlesden-Popper type crystals [44].

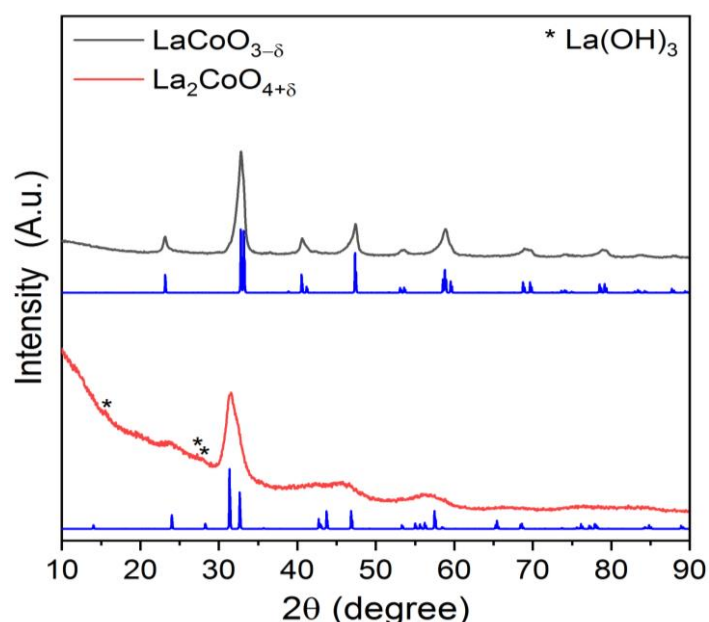


Figure 2. XRD patterns of as-prepared LaCoO_{3-x} and $\text{La}_2\text{CoO}_{4+\delta}$ nanoparticles. Reference phases are $\text{La}_2\text{CoO}_{4.13}$ (ICSD no: 237238, blue line), $\text{LaCoO}_{2.937}$ (ICSD no: 153995, blue line), and $\text{La}(\text{OH})_3$ (ICSD no: 31584), respectively.

To investigate the morphology and size distribution of as-prepared nanoparticles, transmission electron microscopy was performed as shown in Figure 3. For both samples, the count median diameter (CMD) and geometric standard deviation (σ_g) were determined by fitting the size distribution histograms of about 400 nanoparticles to a lognormal distribution. The CMD and σ_g of LaCoO_{3-x} were measured as 17.5 nm and 1.5 while those of $\text{La}_2\text{CoO}_{4+\delta}$ correspond to 10.1 nm and 1.5. Lower particle sizes of $\text{La}_2\text{CoO}_{4+\delta}$ are also implied from the specific surface areas of $\text{La}_2\text{CoO}_{4+\delta}$ and LaCoO_{3-x} nanoparticles being determined by nitrogen adsorption-desorption isotherms through the BET measurements (Brunauer Emmett Teller) [32]. The specific surface area (SSA) of $\text{La}_2\text{CoO}_{4+\delta}$ was measured as 89 m²/g, being considerably higher than the SSA of LaCoO_{3-x} about 43 m²/g. The lower CMD and higher SSA of $\text{La}_2\text{CoO}_{4+\delta}$ particles compared to LaCoO_{3-x} can be associated with precursor characteristics in that lower concentration of La and Co metals being used in the precursor solution of $\text{La}_2\text{CoO}_{4+\delta}$ bring about lower nanoparticles sizes and higher SSA of $\text{La}_2\text{CoO}_{4+\delta}$ (see supplementary material, Table S1). Beside that, the chemical composition of LaCoO_{3-x} , being determined by Energy Dispersive X-Ray (EDX) measurements, indicate that their La/Co atomic ratio is close to unity (see supplementary material, Figure S1), while La/Co atomic ratio of $\text{La}_2\text{CoO}_{4+\delta}$ was measured about 2.3, being slightly higher than nominal atomic ratios in $\text{La}_2\text{CoO}_{4+\delta}$. Excess La content can be owing to small amounts of $\text{La}(\text{OH})_3$ secondary phase being detected from XRD analyses. Overall, the bulk compositions of LaCoO_{3-x} and $\text{La}_2\text{CoO}_{4+\delta}$ nanoparticles show a good agreement with the expected nominal compositions.

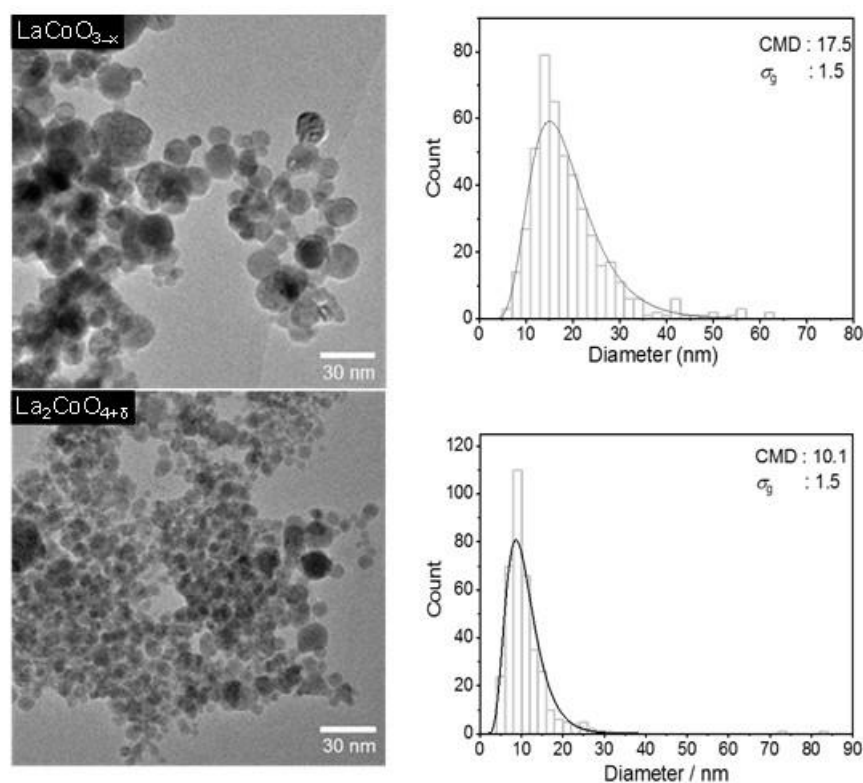


Figure 3. TEM images of LaCoO_{3-x} and $\text{La}_2\text{CoO}_{4+\delta}$ materials (on the left side) and the respective histograms of their particle sizes fitted to a log-normal particle size distribution (on the right side). Count median particle diameter and geometric standard deviation were abbreviated as a CMD and a σ_g , respectively.

The Surface oxidation state and chemistry of Co and La ions were further investigated using the core-level and satellite X-ray photoelectron spectroscopy (XPS) features of $\text{Co}2p_{3/2}$ and $\text{La}3d_{5/2}$ spectra (Figure 4). In both $\text{Co}2p$ and $\text{La}3d$ spectra, lower XPS signals were measured for $\text{La}_2\text{CoO}_{4+\delta}$ compared to LaCoO_{3-x} . This result can be well attributed to the effect of higher content of carbon impurities in $\text{La}_2\text{CoO}_{4+\delta}$, which reduces the respective XPS signal of this sample. For LaCoO_{3-x} , the intense XPS signals of the $\text{Co}2p_{3/2}$ at ~ 779.3 , 781.4 , and 789.5 eV indicate Co^{3+} ions [45], whereas the low-intensity signals of $\text{Co}2p_{3/2}$ at ~ 780.4 , 782.2 , and 785.2 eV can be assigned to the core-level and satellites of Co^{2+} ions, respectively [46]. The atomic proportion of surface $\text{Co}^{3+}/\text{Co}^{2+}$ for LaCoO_{3-x} was found as 58/42, which corresponds to a chemical formula of $\text{LaCoO}_{2.58}$. At the XPS spectra of $\text{La}_2\text{CoO}_{4+\delta}$, the core-level signals of Co^{2+} ions show more intense XPS signals relative to those of Co^{3+} ions, and a low-intensity peak of metallic Co appears at ~ 778.1 eV. The proportion of $\text{Co}^{3+}/\text{Co}^{2+}/\text{Co}$ in $\text{La}_2\text{CoO}_{4+\delta}$ was

measured as 40/49/11, confirming reduced oxidation state of cobalt ions in this sample. The La3d spectra of LaCoO_{3-x} and La₂CoO_{4+δ} exhibit similar XPS spectra at different binding energies. The core-level and satellite signals of La3d_{5/2} signals of LaCoO_{3-x} are visible at ~833.3 and ~837.1 eV with a multiplet splitting of 3.8 eV being in agreement with the La3d spectrum of La-based perovskites [47]. Despite showing a similar multiplet splitting, La3d_{5/2} signals of La₂CoO_{4+δ} shift about 1.1 eV towards higher binding energies. This spectral feature can be attributed to Ruddlesden-Popper-type compounds [48]. All in all, XPS analyses of Co and La ions draw attention to a varying content of surface Co²⁺ and Co³⁺ ions in LaCoO_{3-x} and La₂CoO_{4+δ}, which can govern their catalytic activity for PMS activation.

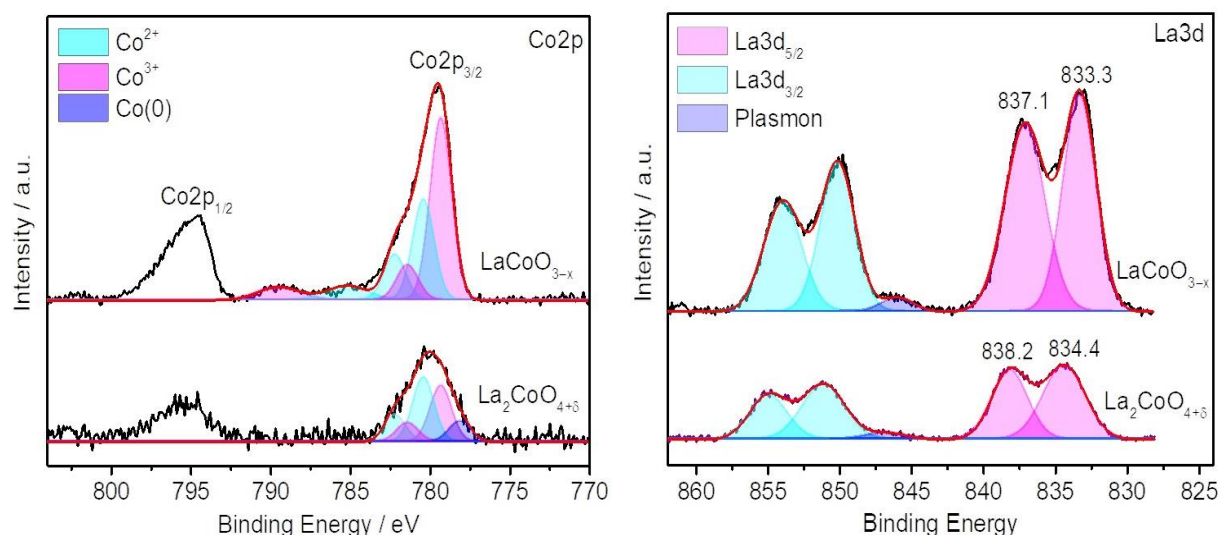


Figure 4. XPS spectra of Co2p and La3d in LaCoO_{3-x} and La₂CoO_{4+δ}, respectively.

3.2 Catalytic activity and stability of catalysts

Figure 5a shows the removal efficiency of BPA for both catalysts and control measurements. The removal of BPA was negligible in the presence of only PMS or catalyst. In the case of the La₂CoO_{4+δ}/PMS system, 97% BPA was removed within 30 min, which was higher than that in the LaCoO_{3-x} + PMS system (70%), implying that the catalytic activity of La₂CoO_{4+δ} is significantly higher than that of LaCoO_{3-x}. Furthermore, the catalytic activity of La₂CoO_{4+δ} was

compared to those of other related Co-based catalysts in the literature (Table 1), and the spray-flame synthesized La_2O_3 and Co_3O_4 , which attained 7% and 45% BPA removal efficiency, respectively, indicating that $\text{La}_2\text{CoO}_{4+\delta}$ materials show a remarkable improvement for PMS activation.

We attribute the remarkable catalytic enhancement of $\text{La}_2\text{CoO}_{4+\delta}$ to the high specific surface area (see supplementary material, Figure S2) and especially the higher surface concentration of Co^{2+} compared to LaCoO_{3-x} material, as we have shown before (Figure 4). Moreover, the BPA removal in both systems could be well fitted by pseudo-first-order kinetics (see supplementary material, Figure S3). The k_{app} of BPA degradation was about 0.152 min^{-1} and 0.03 min^{-1} for $\text{La}_2\text{CoO}_{4+\delta}$ and LaCoO_{3-x} samples, respectively, confirming that the catalytic performance of the $\text{La}_2\text{CoO}_{4+\delta}$ catalyst is significantly higher than that of LaCoO_{3-x} .

Besides, electrochemical impedance analyses were further performed to investigate the electron transfer behavior of both materials (see supplementary material, Figure S4). Obviously, the $\text{La}_2\text{CoO}_{4+\delta}$ electrode (44898Ω) exhibited lower charge transfer resistance compared to the LaCoO_{3-x} electrode ($5705 \cdot 10^7 \Omega$), suggesting that the electron transfer in the $\text{La}_2\text{CoO}_{4+\delta}$ structure is more efficient than that in the LaCoO_{3-x} , which is favorable for the electron transfer during PMS activation [49].

To support these findings, the variation of residual PMS during the PMS activation in both systems was performed (Figure 5c). The residual PMS concentration in a $\text{La}_2\text{CoO}_{4+\delta} + \text{PMS}$ system (0.1 mM) was lower to a $\text{LaCoO}_3 + \text{PMS}$ system (0.32 mM), which attributed to about 80 % and 64 % of the initial PMS concentration, respectively, manifesting that the $\text{La}_2\text{CoO}_{4+\delta} + \text{PMS}$ system activates more PMS as a result of fast electron transport from PMS molecules to the $\text{La}_2\text{CoO}_{4+\delta}$, and therefore higher BPA degradation is obtained.

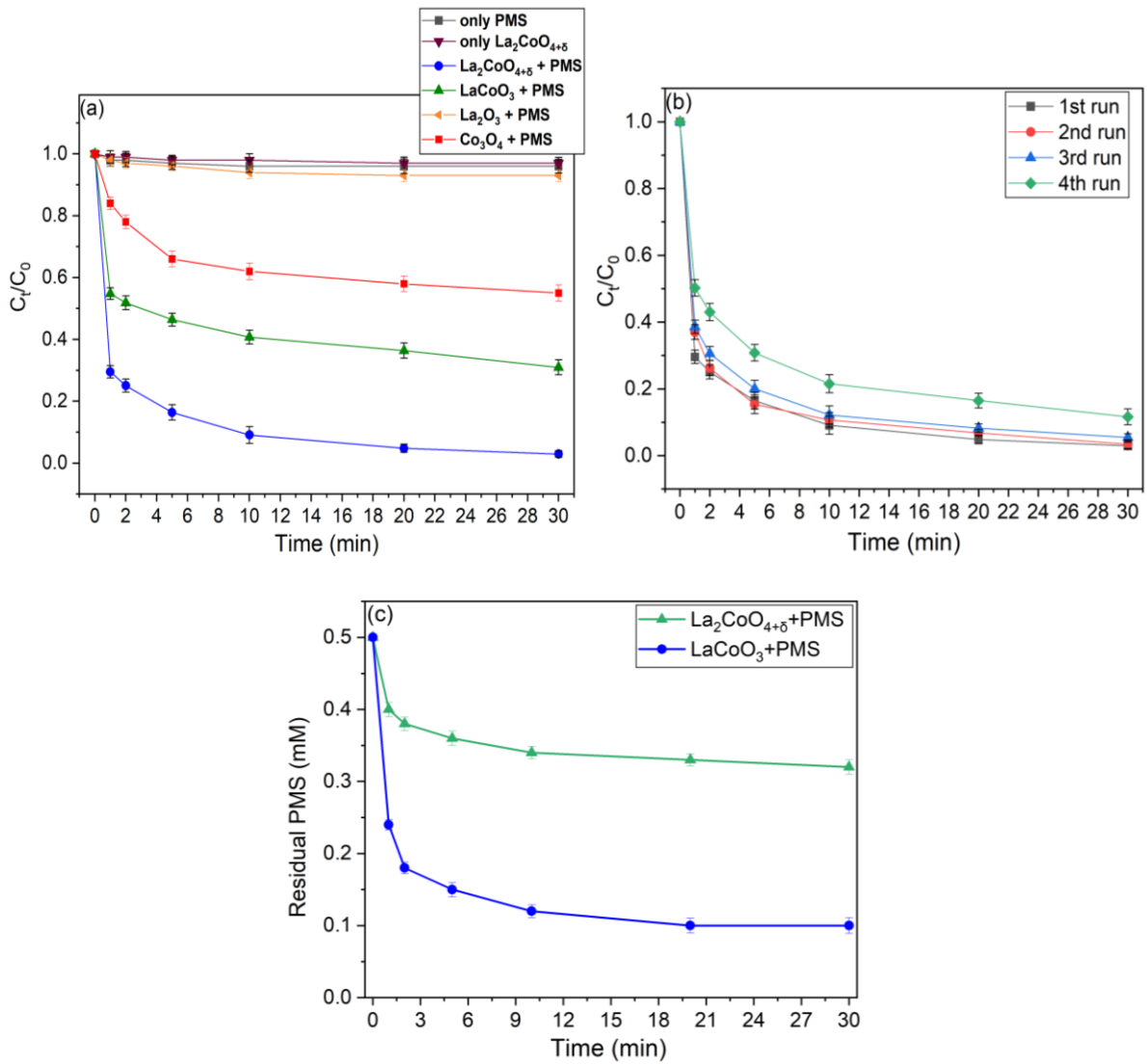


Figure 5. a) BPA degradation with various catalysts in different reaction systems, b) Stability tests of $\text{La}_2\text{CoO}_{4+\delta}$, and c) Residual PMS variation along with the reaction time in different systems. Reaction conditions: (BPA) = 40 mg/L, (PMS) = 0.5 mM; (Catalyst) = 60 mg/L, initial pH = 6.8.

Table 1. Comparison of the BPA degradation by $\text{La}_2\text{CoO}_{4+\delta}$ in this work with those of other related Co-based catalysts in the literature.

| Catalyst | Dosage (mg L ⁻¹) | BPA conc. (mg L ⁻¹) | PMS conc (mM) | BPA removal (%) | Time (min) | k_{app} (min ⁻¹) | Co leaching (mg L ⁻¹) | References |
|--|---------------------------------|------------------------------------|------------------|--------------------|---------------|-----------------------------------|--------------------------------------|------------|
| $\text{CoFe}_2\text{O}_{4-x}$ | 50 | 30 | 1 | 98 | 30 | - | ≈ 1.2 | [50] |
| $\text{Co}_3\text{O}_4/\text{MXene}$ | 100 | 20 | 1 | >99 | 20 | 0.3984 | ≈ 0.36 | [51] |
| $\text{Fe}_{0.8}\text{Co}_{2.2}\text{O}_4$ | 100 | 20 | 0.65 | 95 | 60 | 0.049 | ≈ 0.36 | [52] |

| | | | | | | | | |
|--|-----|----|------|-----|----|--------|--------|-----------|
| Fe ₃ Co ₇ /C | 100 | 20 | 1.3 | 98 | 30 | 0.132 | ≈ 3.30 | [53] |
| Co ₃ O ₄ /MOFs | 100 | 20 | 1.6 | 95 | 10 | 0.87 | ≈ 0.35 | [54] |
| Co ₃ O ₄ /Bi ₂ O ₃ | 300 | 20 | 0.32 | 98 | 30 | 0.1219 | ≈ 0.35 | [55] |
| Co ₃ O ₄ /CC | 100 | 10 | 0.32 | >99 | 10 | ≈0.52 | ≈ 0.25 | [56] |
| La ₂ CoO _{4+δ} | 60 | 40 | 0.5 | 95 | 20 | 0.152 | ≈ 0.04 | This work |

To confirm the practicability of the catalyst in the La₂CoO_{4+δ}/PMS system, the reusability of the La₂CoO_{4+δ} material was investigated in four cycling experiments. As displayed in Figure 5b, the reused La₂CoO_{4+δ} exhibited excellent catalytic performance in the first three reaction runs. However, a decrease in BPA removal to 89% was observed after three reaction runs, which can be mainly ascribed to the formation of insoluble lanthanum carbonate contaminants on the surface of La₂CoO_{4+δ}, resulting in the partial deactivation of the catalyst. This structural change of La₂CoO_{4+δ} catalyst could also be identified by XRD and FTIR. The XRD pattern of the multiple used catalyst shows three additional low-intensity peaks at $2\theta = 18.4^\circ$, 28° , and 41° (Figure 6a), which can be indexed to the orthorhombic layered structure of La₂(CO₃)₃·1.1 H₂O [57]. A similar phenomenon was also observed in the FTIR spectra (Figure 6b). An increased peak intensity around 730 cm^{-1} might be ascribed to the formation of La₂(CO₃)₃·1.1 H₂O [58].

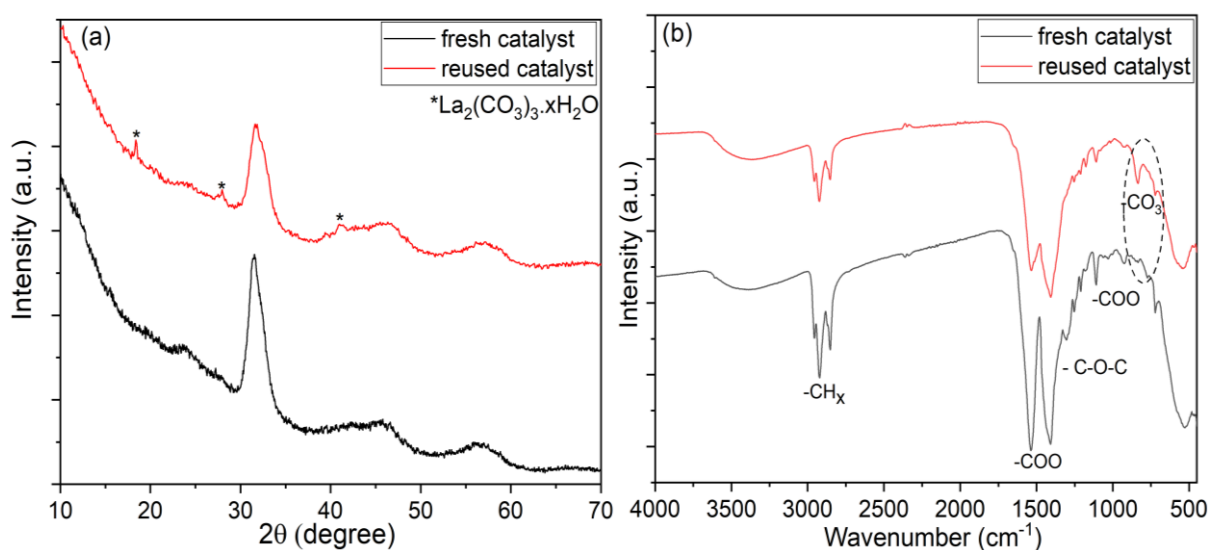


Figure 6. a) XRD patterns and b) FTIR spectra of fresh and reused La₂CoO_{4+δ} catalyst.

Besides, the mineralization extent of BPA was monitored by the TOC analyzer. After 30 min, the TOC removals of BPA was 27% and 49% for LaCoO_{3-x} and $\text{La}_2\text{CoO}_{4+\delta}$ materials, respectively, implying the high BPA mineralization in the $\text{La}_2\text{CoO}_{4+\delta}$ + PMS system. Moreover, the leaching of cobalt and lanthanum ions was further investigated by Atomic Absorption Spectroscopy (AAS) analysis during the PMS activation. Compared to LaCoO_{3-x} (2.6 mg/mL), $\text{La}_2\text{CoO}_{4+\delta}$ showed less Co leaching (0.04 mg/mL), which attributed to about 4.3% and 0.06% of the initial catalyst concentration, respectively, whereas the concentrations of leached lanthanum for LaCoO_{3-x} and $\text{La}_2\text{CoO}_{4+\delta}$ material were around 6.1 and 0.7 mg/L, respectively, accounting to about 10.2% and 1.17% of the initial catalyst concentration, respectively. **We also tested the BPA removal efficiency using the leaching solution under the same conditions (see supplementary material, Figure S5). The BPA removal on the homogenous system was less than 5%. This suggests that the catalytic activity mainly results from the heterogeneous $\text{La}_2\text{CoO}_{4+\delta}$ /PMS system.** These results showed that the $\text{La}_2\text{CoO}_{4+\delta}$ catalyst exhibited high stability and very low cobalt leaching, compared to other cobalt-based catalysts used for BPA removal (Table 1) and further cobalt-based perovskite materials [24,59,60].

3.3 Reactive species and possible mechanisms

Many reactive oxygen species such as $\text{SO}_4^{\bullet-}$, $\cdot\text{OH}$, $^1\text{O}_2$, and $\text{SO}_5^{\bullet-}$ may be involved in the reaction of BPA degradation [61]. $\text{SO}_5^{\bullet-}$ is less efficient to oxidize BPA due to its lower oxidation potential (0.81 V) compared to $\text{SO}_4^{\bullet-}$ [62]. To obtain more detailed information, the contribution of different reactive radicals to BPA degradation was investigated by radical quenching experiments employing $\text{La}_2\text{CoO}_{4+\delta}$. Ethanol (EtOH) was used to scavenge both $\text{SO}_4^{\bullet-}$ and $\cdot\text{OH}$ with a high quenching rate constant of $k_{\text{EtOH}/\cdot\text{OH}} = (1.2-2.8) \times 10^9 \text{ M}^{-1} \text{ s}^{-1}$ and $k_{\text{EtOH}/\text{SO}_4^{\bullet-}} = (1.6-7.7) \times 10^9 \text{ M}^{-1} \text{ s}^{-1}$, while tert-butyl alcohol (TBA) was employed to scavenge only $\cdot\text{OH}$ with a reaction rate constant of $k_{\text{TBA}/\cdot\text{OH}} = (3.8-7.6) \times 10^9 \text{ M}^{-1} \text{ s}^{-1}$ [63]. Besides, singlet

oxygen ($^1\text{O}_2$) might be generated during PMS activation and can be scavenged by β -carotene with a rate constant of $k_{\beta\text{-carotene}/^1\text{O}_2} = (2\text{--}3.0)\times 10^{10} \text{ M}^{-1} \text{ s}^{-1}$ [64].

As shown in Figure 7a, the addition of 0.1 M TBA slightly decreased the removal efficiency of BPA from 97% to 95%, and no significant change was observed with the increase of TBA concentration to 0.5 M. In contrast, the BPA removal with the addition of 0.1 M EtOH was significantly declined to about 58% and even stronger inhibition was observed for higher EtOH concentration (0.5 M). However, the BPA removal inhibited by EtOH is incomplete, suggesting that other reactive radicals may be involved in the reaction of BPA degradation. Singlet oxygen ($^1\text{O}_2$) may also be generated during PMS activation and can be scavenged by β -carotene [64]. It can be seen from Figure 7a that the addition of 0.5 mM β -carotene declined the BPA removal to about 76%, while the addition of β -carotene together with EtOH decreased the BPA degradation in 30 min from 97% to 6%, confirming that $^1\text{O}_2$ was also generated in $\text{La}_2\text{CoO}_{4+\delta}$ /PMS system. The quenching tests imply that $\text{SO}_4^{\cdot-}$ is the primary active radical in the $\text{La}_2\text{CoO}_{4+\delta}$ /PMS system.

To confirm the generation of reactive radicals from PMS activation, Electron Paramagnetic Resonance (EPR) experiments were conducted using DMPO and TEMP as a radical spin-trapping agent (Figure 7b). There was no signal peak detected in the presence of PMS alone or of the catalyst alone, indicating that no radicals could be generated with bare PMS and catalyst. However, when $\text{La}_2\text{CoO}_{4+\delta}$ /PMS were added, characteristic signals for DMPO- $\cdot\text{OH}$ adducts (with hyperfine splitting constants of $\alpha_{\text{H}} = \alpha_{\text{N}} = 14.8 \text{ G}$) and DMPO- $\text{SO}_4^{\cdot-}$ adducts ($\alpha_{\text{N}} = 13.2 \text{ G}$, $\alpha_{\text{N}} = 9.6 \text{ G}$, $\alpha_{\text{H}} = 1.48 \text{ G}$, $\alpha_{\text{H}} = 0.78 \text{ G}$) were observed, confirming that both $\cdot\text{OH}$ and $\text{SO}_4^{\cdot-}$ radicals were produced by the $\text{La}_2\text{CoO}_{4+\delta}$ /PMS system. Thus, we propose that the generation of $\cdot\text{OH}$ in the $\text{La}_2\text{CoO}_{4+\delta}$ /PMS system originates from the reaction of $\text{SO}_4^{\cdot-}$ with the hydroxyl ion (equation 2) or water (equation 3) [65].



Besides, TEMP was selected as the trapping agent to gain more evidence for the generation of the singlet oxygen ($^1\text{O}_2$) by the EPR test. As illustrated in Figure 7c, the characteristic peak assigned to TEMP- $^1\text{O}_2$ was observed in the $\text{La}_2\text{CoO}_{4+\delta}/\text{PMS}$ system. These results are in good agreement with the quenching experiments, confirming the generation of $^1\text{O}_2$ in the $\text{La}_2\text{CoO}_{4+\delta}/\text{PMS}$ system.

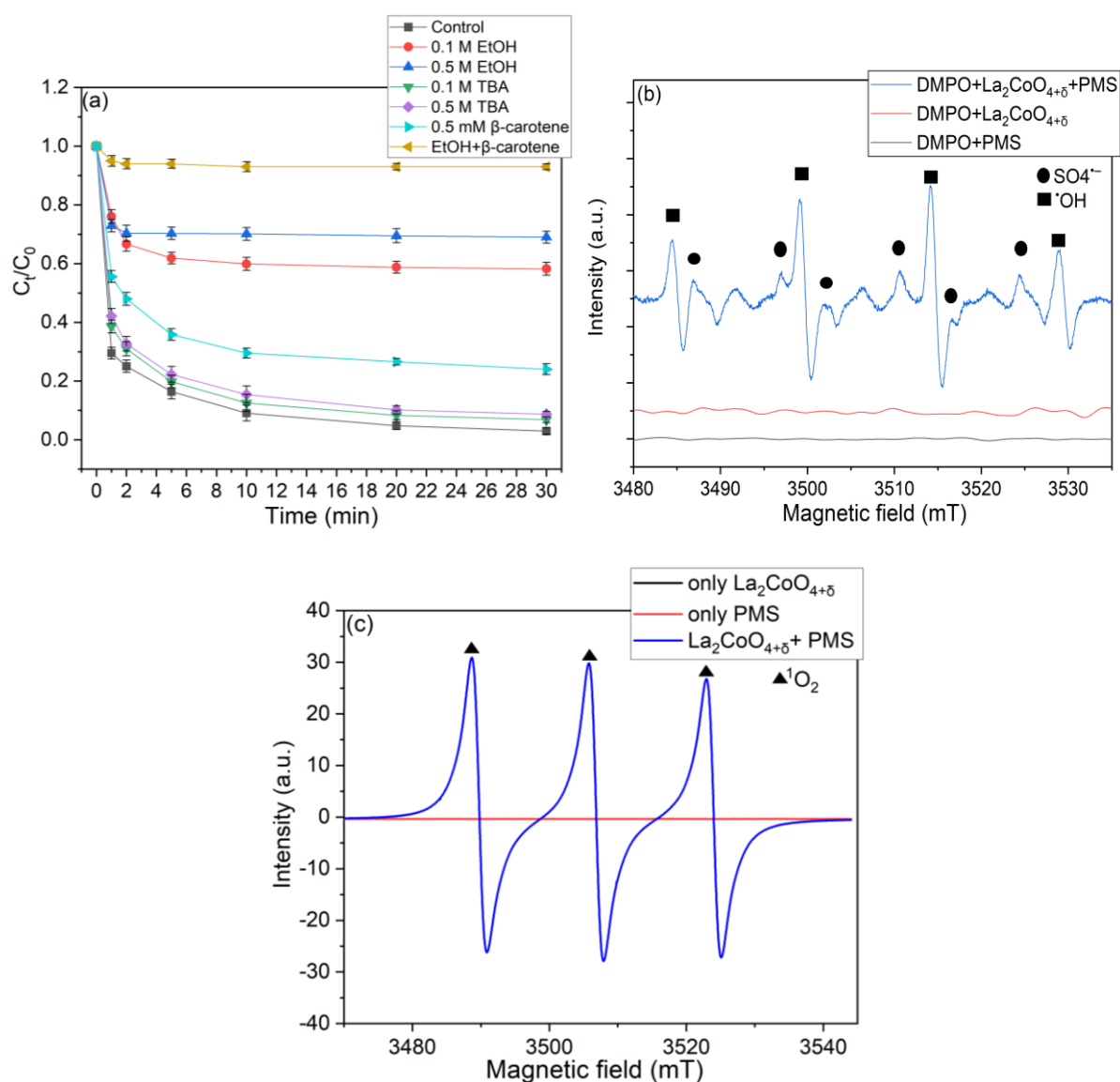


Figure 7. a) Effect of radical scavengers on BPA degradation in different reaction systems, b) EPR spectra in $\text{La}_2\text{CoO}_{4+\delta}/\text{PMS}$ systems with DMPO, and c) EPR spectra in $\text{La}_2\text{CoO}_{4+\delta}/\text{PMS}$ systems with TEMP as the trapping agent. Reaction conditions: (BPA) = 40 mg/L, (PMS) = 0.5 mM, (Catalyst) = 60 mg/L, (DMPO) = 50 mM, (TEMP) = 20 mM, initial pH = 6.8.

To further elaborate the mechanism of PMS activation and the roles of La, Co, and O species, the XPS spectra of $\text{La}_2\text{CoO}_{4+\delta}$ before and after four runs of catalytic experiments were studied. There was no significant change in the La3d spectrum before and after the reaction, suggesting that La is not involved in the PMS activation (see supplementary material, Figure S6). As depicted in Figure 8a, the high-resolution Co2p XPS spectra for the fresh and used catalysts can be fitted using five core-level peaks centered at $\sim 778.2, 779.6, 780.4, 781.4, 782.2$, and the satellite at ~ 786.5 eV. The binding energies at 780.4 and 782.1 eV can be assigned to Co^{2+} , whereas the peak with binding energy positioned at 779.6 eV is assigned to Co^{3+} [66]. The shake-up satellite peak located at 786.5 eV indicates the presence of Co^{2+} species [66]. **While the initial proportions of $\text{Co}^{3+}/\text{Co}^{2+}/\text{Co}$ were determined as of 40/49/11, they changed to 37/55/8, which indicates the increasing surface concentration of Co^{2+} ions, thereby suggesting a redox process $\text{Co}^{2+} - \text{Co}^{3+} - \text{Co}^{2+}$ at the catalysts' surface.** This finding is supported by analyzing the O1s spectra (Figure 8b). The peaks centered at 528.5, 529.6, 531.2, and 532.3 eV corresponded to oxygen in the lattice (O_L), surface $\text{O}_2^{2-}/\text{O}^-$, surface hydroxyl groups (OH), and adsorbed water and carbonates, respectively, and initially accounted for 22, 13, 46, and 19%, respectively [60]. These relative proportions change to 17, 14, 46, and 23% after the catalytic reaction [60]. The decline in the O_L can be attributed to the release of oxygen in combination with the reduction of Co^{3+} to Co^{2+} , suggesting that lattice O_L participated in the cobalt redox reaction. The increment of carbonate and water contents can be attributed to the formation of lanthanum carbonate contaminants on the surface of $\text{La}_2\text{CoO}_{4+\delta}$.

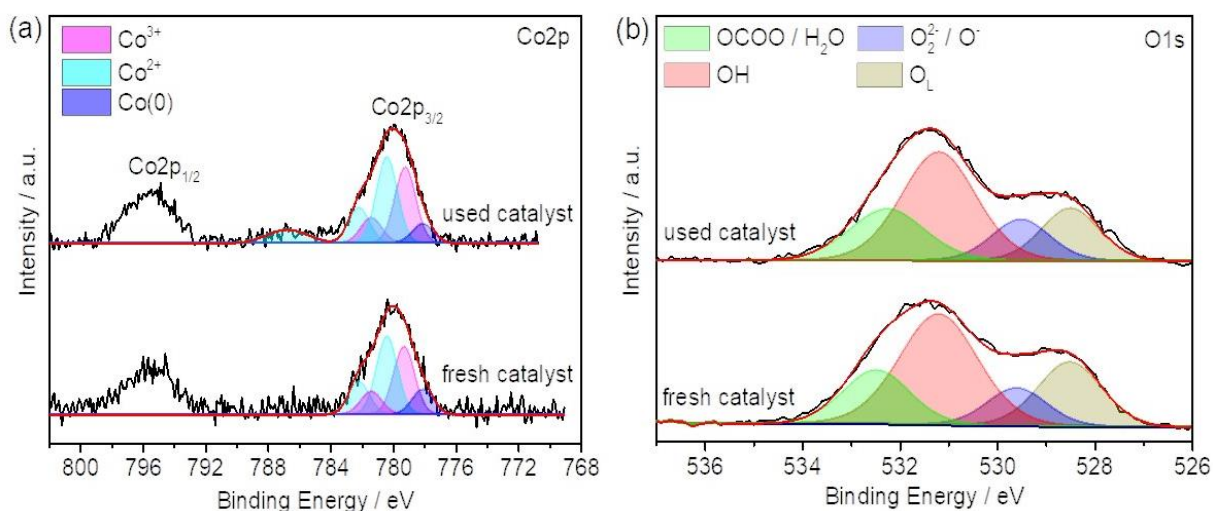
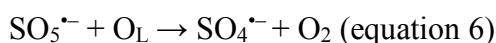
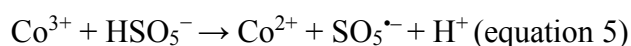
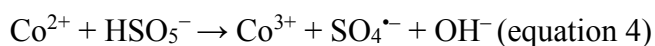


Figure 8. XPS spectra of (a) Co2p and (b) O1s for fresh and used $\text{La}_2\text{CoO}_{4+\delta}$ materials.

Based on the above results, a catalysis mechanism of PMS activation by $\text{La}_2\text{CoO}_{4+\delta}$ is proposed as follows: After the addition of PMS, $\text{SO}_4^{\cdot-}$ is initially generated by the activation of HSO_5^- species on $\text{La}_2\text{CoO}_{4+\delta}$ (equation 4) and simultaneously some initially generated $\text{SO}_4^{\cdot-}$ will react with hydroxyl ion or water to generate $\cdot\text{OH}$ (equations 2-3). These radicals could attack and mineralize the BPA to small organic intermediates and then finally to CO_2 (equation 7). On the other hand, to keep the charge balance on the $\text{La}_2\text{CoO}_{4+\delta}$ surface, the lattice oxygen could facilitate the charge transfer to Co^{3+} and be released to the system in the form of O_2 (equations 5-6). Lattice oxygen ions cannot migrate from the bulk to the surface under the atmospheric ambience in the aqueous phase [67,68]. Therefore, the adsorbed oxygen might transform to lattice oxygen due to the high charge and oxygen-ion conductivity [69], which would compensate the surface lattice oxygen to improve catalytic efficiency. Furthermore, since the standard potential value of $\text{Co}^{2+}/\text{Co}^{3+}$ redox pairs (1.8 V) is higher than that of $\text{HSO}_5^-/\text{SO}_5^{\cdot-}$ (1.1 V), the reduction of Co^{3+} is thermodynamically favorable. Therefore, the regeneration of the catalyst can be achieved by the reverse electron transfer from Co^{3+} to Co^{2+} .

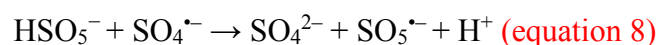


3.4 Effect of reaction parameters on BPA degradation

To select the optimum dosage of $\text{La}_2\text{CoO}_{4+\delta}$ and PMS concentration, the influence of catalyst dosage and PMS concentration on the BPA removal efficiency was investigated. Moreover, the pH of the medium is one of the important factors for the catalytic stability of $\text{La}_2\text{CoO}_{4+\delta}$. Thus, different initial pH values, as well as the effect of the inorganic anions in the process of PMS oxidation, were also investigated as a basis for a practical application of the $\text{La}_2\text{CoO}_{4+\delta}$ catalyst.

3.4.1 Effect of catalyst dose and PMS concentration

Not surprisingly, as depicted in Figure 9a, k_{app} was enhanced from 0.046 min^{-1} to 0.19 min^{-1} when the $\text{La}_2\text{CoO}_{4+\delta}$ loading was increased from between 0.03 to 0.24 g/L. We attribute this to an increasing number of active sites on the surface of $\text{La}_2\text{CoO}_{4+\delta}$ which are accessible for PMS activation and thus generating more active radicals. The k_{app} also was increased as the PMS concentration was raised from 0.25 to 2 mM (Figure 9b), however, it decreased in the case of overdose (4 mM), which was most likely due to the scavenging of $\text{SO}_4^{\bullet-}$ by the excessive HSO_5^- (equation 8) [70].



3.4.2 Effect of initial pH

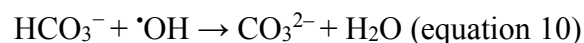
The initial pH of the reaction solution is also a significant parameter for PMS activation that can affect the interfacial interactions between the catalyst and PMS and is studied in the process of PMS oxidation. Figure 9c displays the influence of initial pH on BPA removal in the $\text{La}_2\text{CoO}_{4+\delta}$ /PMS system. It is obvious that the BPA was almost degraded within 30 min over a pH of 5.0 to 8.8. However, when the initial pH of the solution was adjusted to 3.3 and 10.6, the BPA removal efficiency decreased to 50 and 89%, respectively. Since the $\text{pK}_{\text{a}1}$ of PMS is 0 and $\text{pK}_{\text{a}2}$ is 9.4, PMS mainly exists as HSO_5^- in the pH range of 0-9.4. The pH_{pzc} (pH at the point

of zero charges) of $\text{La}_2\text{CoO}_{4+\delta}$ is determined at around 9.5 (see supplementary material, Figure S7). Accordingly, when pH is higher than 9.4, SO_5^{2-} would replace HSO_5^- , which reduces the amount of active reactive species and therefore diminishing the $\text{La}_2\text{CoO}_{4+\delta}$ /PMS efficiency [71]. Moreover, the electrostatic repulsion interactions between negatively charged $\text{La}_2\text{CoO}_{4+\delta}$ and PMS species would slow the activation efficiency of PMS, thus the removal efficiency of BPA is reduced. At strong acidic conditions (pH=3.5), a large number of hydrogen ions H^+ attached to HSO_5^- and form a hydrogen bond, which is unfavorable for the interaction between $\text{La}_2\text{CoO}_{4+\delta}$ and PMS species. Furthermore, lower pH can result in the leaching of cobalt ions into the solution, resulting in a decrease in the number of catalytic sites (Figure 9d). The concentration of leached cobalt ions in the acidic solution (pH = 3.5) is 0.8 mg/L and decreased to 0.04 mg/L at pH = 6.8. Therefore, BPA removal efficiency declined significantly at acidic conditions (pH = 3.5).

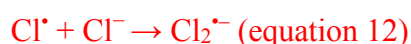
3.4.3 Effect of co-existing ions

The effect of various anions relevant in aqueous systems (such as Cl^- , NO_3^- , H_2PO_4^- , HCO_3^- , etc.) on the degradation of BPA in $\text{La}_2\text{CoO}_{4+\delta}$ /PMS was also investigated and is shown in Figure 9e. Compared to the $\text{La}_2\text{CoO}_{4+\delta}$ /PMS system, the addition of NO_3^- anion did not have a significant impact on BPA degradation. Moreover, H_2PO_4^- and HCO_3^- anions exerted an inhibitory effect on BPA degradation while the Cl^- anions accelerated the BPA degradation. In the presence of H_2PO_4^- , the degradation of BPA was reduced due to the formation of complex compounds of phosphate-Co during the PMS oxidation system (see supplementary material, Figure S8), which deactivate the catalytic reactive sites. However, HCO_3^- exhibited an inhibitory effect on BPA removal higher than the inhibition caused by H_2PO_4^- . This negative influence might be due to the scavenging effect of $\text{SO}_4^{\bullet-}$ and $\cdot\text{OH}$ by HCO_3^- in the solution (equation 9-10), which can lead to a decrease in the performance of BPA degradation.





Low concentrations of Cl^- (0.01-0.03 M) had a slight inhibitory effect on BPA degradation (see supplementary material, Figure S9), which may be ascribed to the reaction of Cl^- with $\text{SO}_4^{\cdot-}$ (equations 11-12), producing radicals with lower redox potentials (Cl^\cdot and $\text{Cl}_2^{\cdot-}$) compared to $\text{SO}_4^{\cdot-}$. In contrast, the removal efficiency is enhanced with the addition of Cl^- (0.05-0.1 M). The positive influence of Cl^- ions on BPA degradation may be ascribed to the generation of a large amount of more effective chlorine species (e.g. HOCl) which participate in BPA degradation because of the reaction with HSO_5^- (equations 13). To further investigate the influence of Cl^- on BPA degradation, the catalytic processes in the presence of only PMS were carried out (see supplementary material, Figure S10). The BPA degradation was significantly enhanced with 0.1 M Cl^- , suggest that HOCl generated from the reaction of Cl^- ions with HSO_5^- as a nonradical pathway for BPA degradation. Moreover, the adsorption of BPA with the different Cl^- concentrations was also studied (see supplementary material, Figure S11). 4-6% of BPA was adsorbed by the $\text{La}_2\text{CoO}_{4+\delta}$ at different Cl^- concentrations, indicating that the impact of Cl^- on BPA adsorption was almost negligible. Thus, we propose that the accelerated BPA degradation is based on the generation of HOCl in the $\text{La}_2\text{CoO}_{4+\delta}/\text{PMS}/\text{Cl}^-$ system



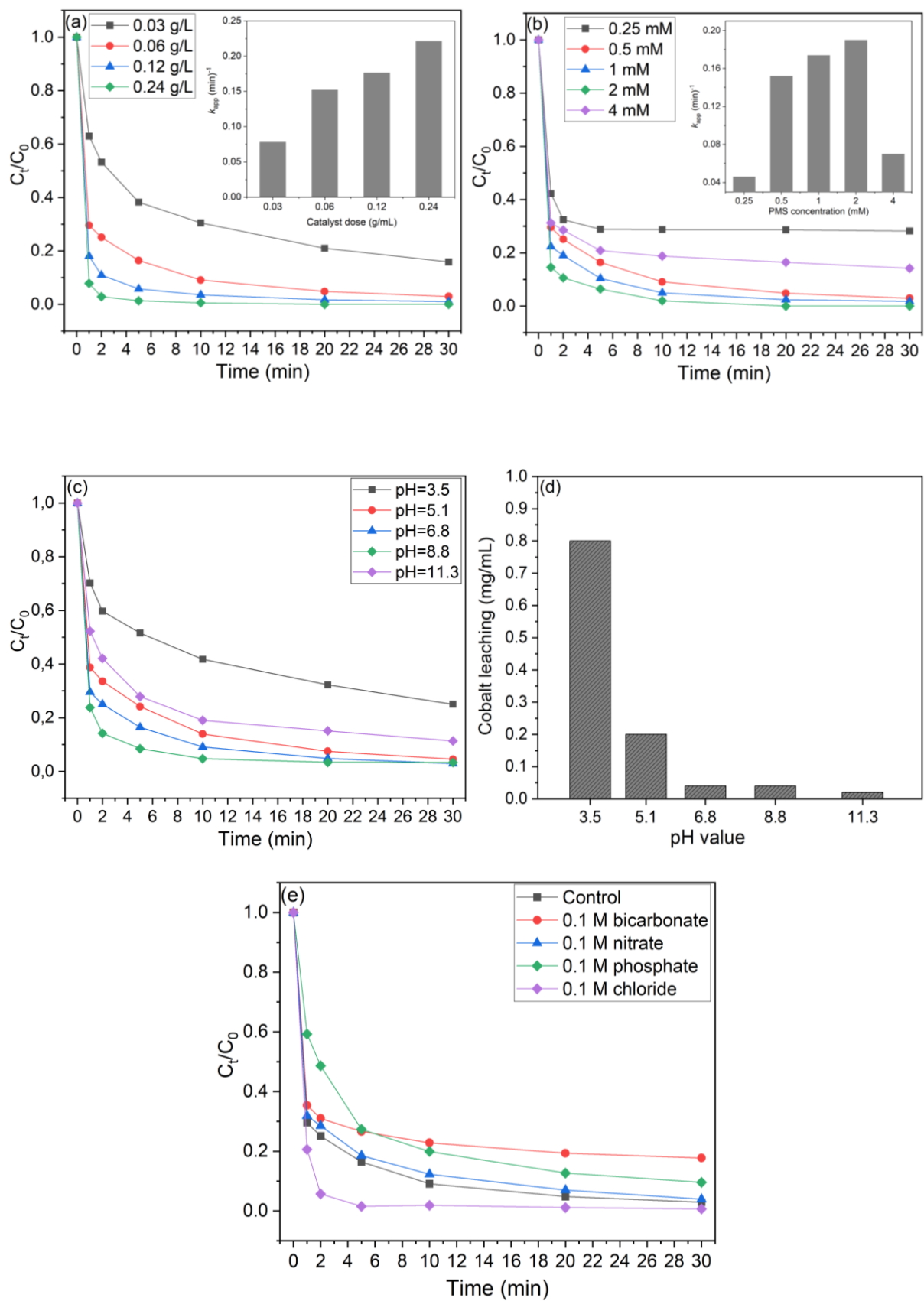


Figure 9. Effects of (a) catalyst loading, (b) PMS dosages, (c) initial pH values and (d) cobalt leaching, and (e) inorganic anions on BPA degradation by $\text{La}_2\text{CoO}_{4+\delta}/\text{PMS}$. Reaction conditions: (BPA) = 40 mg/L, (PMS) = 0.5 mM, (Catalyst) = 60 mg/L, initial pH = 6.8.

3.4.4 Effect of water matrices and different pollutants

The catalytic performance of the $\text{La}_2\text{CoO}_{4+\delta}$ nanoparticles in degrading different types of organic pollutants is important for its environmental remediation application. Hence, the catalytic activity $\text{La}_2\text{CoO}_{4+\delta}$ was evaluated with different charge organic pollutants including MB, RhB, and AO7. As shown in Figure 10a, the removal efficiency of MB, RhB, and AO7 after 30 min was 99%, 90%, and 99%, respectively, proving that the $\text{La}_2\text{CoO}_{4+\delta}$ /PMS system could be employed to degrade effectively different kind of organic pollutant. Moreover, to detect the applicability of the $\text{La}_2\text{CoO}_{4+\delta}$ + PMS system in real aquatic environments, the effect of various water matrices such as drinking water and taping water on the catalytic activity of $\text{La}_2\text{CoO}_{4+\delta}$ was studied. As depicted in Figure 10b, the removal efficiency of BPA was unremarkably affected in the drinking water sample, whereas the degradation efficiency of BPA was decreased slightly in the tap water sample to 90%. These results suggest that the anions in the water had an insignificant inhibitory effect on the BPA removal.

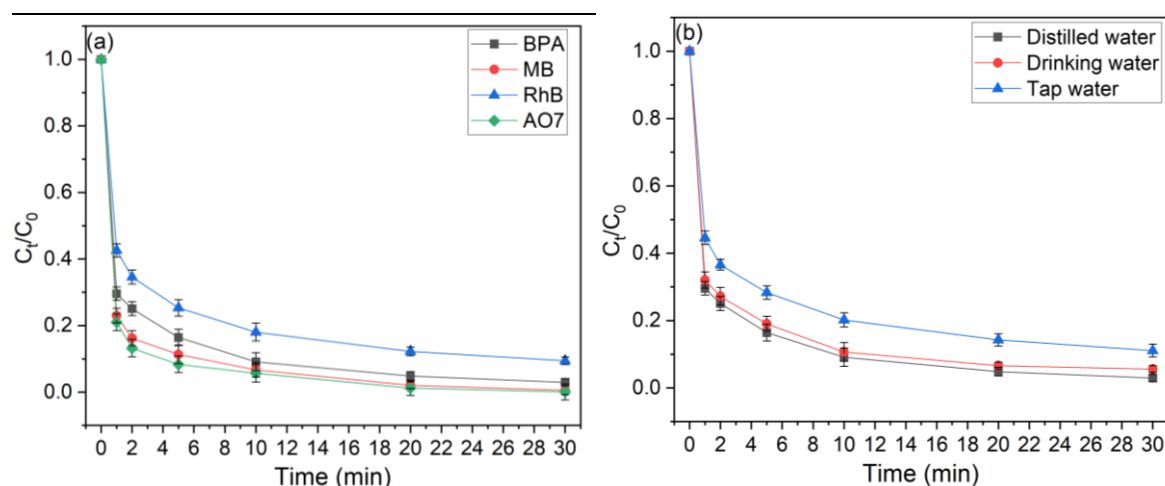


Figure 10. a) Catalytic activity of $\text{La}_2\text{CoO}_{4+\delta}$ a) in the removal of various organics dyes and b) in water matrices.

3.5 Possible degradation pathways

To study the degradation pathway of BPA, the degradation intermediates of BPA via the $\text{La}_2\text{CoO}_{4+\delta}$ /PMS system were identified by LC-MS (see supplementary material, Figure S12).

According to the mass spectrometric results (see supplementary material, Table S2), the aromatic and aliphatic intermediates, namely, 2-(4-hydroxyphenyl)-propanol-2-ol, 4-isopropenylphenol, ethanedioic acid, 1,5-hexadiene-3-ol, and trimethylhexane were detected. Mainly, the aromatic ring in BPA is attacked by $\text{SO}_4^{\cdot-}$ or $\cdot\text{OH}$ and converted to 2-(4-hydroxyphenyl)-propanol-2-ol [52] and the attack on the tertiary hydroxyl produces 4-isopropenylphenol. Afterwards, the intermediate products were subsequently attacked to form ethanedioic acid, 1,5-hexadiene-3-ol, and trimethylhexane. Finally, the intermediate products were further oxidized and mineralized into CO_2 and H_2O .

4 Conclusions

In summary, we have demonstrated that $\text{La}_2\text{CoO}_{4+\delta}$ nanoparticles were successfully synthesized via spray-flame synthesis, and applied as novel catalysts for PMS activation. The spray-flame synthesis method has practical advantages such as scalability to produce large amounts of $\text{La}_2\text{CoO}_{4+\delta}$ nanoparticles in one step without high-temperature annealing, eco-friendliness, and cost-effectivity. Compared to LaCoO_{3-x} catalyst, $\text{La}_2\text{CoO}_{4+\delta}$ nanoparticles exhibit a faster catalytic activity for BPA oxidation and better stability with less cobalt leaching in the presence of PMS. These enhancements were attributed to the lower oxidation state of cobalt, fast regeneration of Co^{2+} during PMS activation, and large catalyst particle surface area. Moreover, the removal efficiency maintained 89% after four successive experimental runs. Radicals quenching experiments and electron paramagnetic resonance studies showed that $\text{SO}_4^{\cdot-}$ played a dominant role during the activation of PMS. In consideration of catalytic activity and costs, this study provides an option to broaden the application of $\text{La}_2\text{CoO}_{4+\delta}$ catalysts for water treatment by PMS activation.

5 References

- [1] C. Erler, J. Novak, Bisphenol A Exposure: Human Risk and Health Policy, *J. Pediatr. Nurs.* 25 (2010) 400–407. <https://doi.org/https://doi.org/10.1016/j.pedn.2009.05.006>.
- [2] A. Schechter, N. Malik, D. Haffner, S. Smith, T.R. Harris, O. Paepke, L. Birnbaum, Bisphenol A (BPA) in U.S. Food, *Environ. Sci. Technol.* 44 (2010) 9425–9430. <https://doi.org/10.1021/es102785d>.
- [3] Y. Yoon, P. Westerhoff, S.A. Snyder, E.C. Wert, Nanofiltration and ultrafiltration of endocrine disrupting compounds, pharmaceuticals and personal care products, *J. Memb. Sci.* 270 (2006) 88–100. <https://doi.org/https://doi.org/10.1016/j.memsci.2005.06.045>.
- [4] J. Ali, W. Jiang, A. Shahzad, J. Ifthikar, X. Yang, B. Wu, D.T. Oyekunle, W. Jia, Z. Chen, L. Zheng, Z. Chen, Isolated copper ions and surface hydroxyl groups as a function of non-redox metals to modulate the reactivity and persulfate activation mechanism of spinel oxides, *Chem. Eng. J.* 425 (2021) 130679. <https://doi.org/https://doi.org/10.1016/j.cej.2021.130679>.
- [5] M. Hammad, P. Fortugno, S. Hardt, C. Kim, S. Salamon, T.C. Schmidt, H. Wende, C. Schulz, H. Wiggers, Large-scale synthesis of iron oxide/graphene hybrid materials as highly efficient photo-Fenton catalyst for water remediation, *Environ. Technol. Innov.* (2020) 101239. <https://doi.org/https://doi.org/10.1016/j.eti.2020.101239>.
- [6] S. Guo, H. Wang, W. Yang, H. Fida, L. You, K. Zhou, Scalable synthesis of Ca-doped α -Fe₂O₃ with abundant oxygen vacancies for enhanced degradation of organic pollutants through peroxymonosulfate activation, *Appl. Catal. B Environ.* 262 (2020) 118250. <https://doi.org/https://doi.org/10.1016/j.apcatb.2019.118250>.
- [7] J. Ali, A. Shahzad, J. Wang, J. Ifthikar, W. Lei, G.G. Aregay, Z. Chen, Z. Chen, Modulating the redox cycles of homogenous Fe(III)/PMS system through constructing

- electron rich thiomolybdate centres in confined layered double hydroxides, *Chem. Eng. J.* 408 (2021) 127242. <https://doi.org/10.1016/j.cej.2020.127242>.
- [8] Y. Liu, Y. Wang, Q. Wang, J. Pan, J. Zhang, Simultaneous removal of NO and SO₂ using vacuum ultraviolet light (VUV)/heat/peroxymonosulfate (PMS), *Chemosphere*. 190 (2018) 431–441.
<https://doi.org/10.1016/j.chemosphere.2017.10.020>.
- [9] Z.-H. Diao, Z.-Y. Lin, X.-Z. Chen, L. Yan, F.-X. Dong, W. Qian, L.-J. Kong, J.-J. Du, W. Chu, Ultrasound-assisted heterogeneous activation of peroxymonosulphate by natural pyrite for 2,4-dichlorophenol degradation in water: Synergistic effects, pathway and mechanism, *Chem. Eng. J.* (2019) 123771.
<https://doi.org/10.1016/j.cej.2019.123771>.
- [10] R. Xie, J. Ji, K. Guo, D. Lei, Q. Fan, D.Y.C. Leung, H. Huang, Wet scrubber coupled with UV/PMS process for efficient removal of gaseous VOCs: Roles of sulfate and hydroxyl radicals, *Chem. Eng. J.* 356 (2019) 632–640.
<https://doi.org/10.1016/j.cej.2018.09.025>.
- [11] H. Song, L. Yan, Y. Wang, J. Jiang, J. Ma, C. Li, G. Wang, J. Gu, P. Liu, Electrochemically activated PMS and PDS: Radical oxidation versus nonradical oxidation, *Chem. Eng. J.* (2019) 123560.
<https://doi.org/10.1016/j.cej.2019.123560>.
- [12] B. Bouzayani, E. Rosales, M. Pazos, S.C. Elaoud, M.A. Sanromán, Homogeneous and heterogeneous peroxymonosulfate activation by transition metals for the degradation of industrial leather dye, *J. Clean. Prod.* 228 (2019) 222–230.
<https://doi.org/10.1016/j.jclepro.2019.04.217>.
- [13] G.P. Anipsitakis, D.D. Dionysiou, Radical Generation by the Interaction of Transition Metals with Common Oxidants, *Environ. Sci. Technol.* 38 (2004) 3705–3712.
<https://doi.org/10.1021/es035121o>.

- [14] F.J. Rivas, O. Gimeno, T. Borallho, Aqueous pharmaceutical compounds removal by potassium monopersulfate. Uncatalyzed and catalyzed semicontinuous experiments, *Chem. Eng. J.* 192 (2012) 326–333.
<https://doi.org/https://doi.org/10.1016/j.cej.2012.03.055>.
- [15] J. Wang, S. Wang, Activation of persulfate (PS) and peroxymonosulfate (PMS) and application for the degradation of emerging contaminants, *Chem. Eng. J.* 334 (2018) 1502–1517. <https://doi.org/https://doi.org/10.1016/j.cej.2017.11.059>.
- [16] E. Saputra, S. Muhammad, H. Sun, H.-M. Ang, M.O. Tadé, S. Wang, A comparative study of spinel structured Mn₃O₄, Co₃O₄ and Fe₃O₄ nanoparticles in catalytic oxidation of phenolic contaminants in aqueous solutions, *J. Colloid Interface Sci.* 407 (2013) 467–473. <https://doi.org/https://doi.org/10.1016/j.jcis.2013.06.061>.
- [17] Y. Yao, Y. Cai, G. Wu, F. Wei, X. Li, H. Chen, S. Wang, Sulfate radicals induced from peroxymonosulfate by cobalt manganese oxides (Co_xMn_{3-x}O₄) for Fenton-Like reaction in water, *J. Hazard. Mater.* 296 (2015) 128–137.
<https://doi.org/https://doi.org/10.1016/j.jhazmat.2015.04.014>.
- [18] A. Jawad, J. Lang, Z. Liao, A. Khan, J. Ifthikar, Z. Lv, S. Long, Z. Chen, Z. Chen, Activation of persulfate by CuOx@Co-LDH: A novel heterogeneous system for contaminant degradation with broad pH window and controlled leaching, *Chem. Eng. J.* 335 (2018) 548–559. <https://doi.org/https://doi.org/10.1016/j.cej.2017.10.097>.
- [19] J.C. Espinosa, P. Manickam-Periyaraman, F. Bernat-Quesada, S. Sivanesan, M. Álvaro, H. García, S. Navalón, Engineering of activated carbon surface to enhance the catalytic activity of supported cobalt oxide nanoparticles in peroxymonosulfate activation, *Appl. Catal. B Environ.* 249 (2019) 42–53.
<https://doi.org/https://doi.org/10.1016/j.apcatb.2019.02.043>.
- [20] J. Zhu, H. Li, L. Zhong, P. Xiao, X. Xu, X. Yang, Z. Zhao, J. Li, Perovskite Oxides: Preparation, Characterizations, and Applications in Heterogeneous Catalysis, *ACS*

- Catal. 4 (2014) 2917–2940. <https://doi.org/10.1021/cs500606g>.
- [21] K.-Y.A. Lin, Y.-C. Chen, Y.-F. Lin, LaMO₃ perovskites (M=Co, Cu, Fe and Ni) as heterogeneous catalysts for activating peroxymonosulfate in water, Chem. Eng. Sci. 160 (2017) 96–105. <https://doi.org/https://doi.org/10.1016/j.ces.2016.11.017>.
- [22] X. Pang, Y. Guo, Y. Zhang, B. Xu, F. Qi, LaCoO₃ perovskite oxide activation of peroxymonosulfate for aqueous 2-phenyl-5-sulfobenzimidazole degradation: Effect of synthetic method and the reaction mechanism, Chem. Eng. J. 304 (2016) 897–907. <https://doi.org/https://doi.org/10.1016/j.cej.2016.07.027>.
- [23] P. Liang, D. Meng, Y. Liang, Z. Wang, C. Zhang, S. Wang, Z. Zhang, Cation deficiency tuned LaCoO_{3-δ} perovskite for peroxymonosulfate activation towards bisphenol A degradation, Chem. Eng. J. 409 (2021) 128196. <https://doi.org/https://doi.org/10.1016/j.cej.2020.128196>.
- [24] X. Duan, C. Su, J. Miao, Y. Zhong, Z. Shao, S. Wang, H. Sun, Insights into perovskite-catalyzed peroxymonosulfate activation: Maneuverable cobalt sites for promoted evolution of sulfate radicals, Appl. Catal. B Environ. 220 (2018) 626–634. <https://doi.org/https://doi.org/10.1016/j.apcatb.2017.08.088>.
- [25] Y. Takeda, R. Kanno, M. Sakano, O. Yamamoto, M. Takano, Y. Bando, H. Akinaga, K. Takita, J.B. Goodenough, Crystal chemistry and physical properties of La_{2-x}Sr_xNiO₄ (0 ≤ x ≤ 1.6), Mater. Res. Bull. 25 (1990) 293–306. [https://doi.org/https://doi.org/10.1016/0025-5408\(90\)90100-G](https://doi.org/https://doi.org/10.1016/0025-5408(90)90100-G).
- [26] S.D. Peter, E. Garbowski, N. Guilhaume, V. Perrichon, M. Primet, Catalytic properties of La₂CuO₄ in the CO + NO reaction, Catal. Letters. 54 (1998) 79–84. <https://doi.org/10.1023/A:1019063502409>.
- [27] Y. Huan, S. Chen, R. Zeng, T. Wei, D. Dong, X. Hu, Y. Huang, Intrinsic Effects of Ruddlesden-Popper-Based Bifunctional Catalysts for High-Temperature Oxygen Reduction and Evolution, Adv. Energy Mater. 9 (2019) 1901573.

- <https://doi.org/https://doi.org/10.1002/aenm.201901573>.
- [28] T. Oshima, T. Yokoi, M. Eguchi, K. Maeda, Synthesis and photocatalytic activity of $K_2CaNaNb_3O_{10}$, a new Ruddlesden–Popper phase layered perovskite, *Dalt. Trans.* 46 (2017) 10594–10601. <https://doi.org/10.1039/C6DT04872B>.
- [29] J. Zhu, Z. Zhao, D. Xiao, J. Li, X. Yang, Y. Wu, CO Oxidation, NO Decomposition, and NO + CO Reduction over Perovskite-like Oxides La_2CuO_4 and $La_{2-x}Sr_xCuO_4$: An MS–TPD Study, *Ind. Eng. Chem. Res.* 44 (2005) 4227–4233. <https://doi.org/10.1021/ie050317d>.
- [30] R.P. Forslund, C.T. Alexander, A.M. Abakumov, K.P. Johnston, K.J. Stevenson, Enhanced Electrocatalytic Activities by Substitutional Tuning of Nickel-Based Ruddlesden–Popper Catalysts for the Oxidation of Urea and Small Alcohols, *ACS Catal.* 9 (2019) 2664–2673. <https://doi.org/10.1021/acscatal.8b04103>.
- [31] J. Choi, S. Park, H. Han, M. Kim, M. Park, J. Han, W.B. Kim, Highly efficient CO_2 electrolysis to CO on Ruddlesden–Popper perovskite oxide with in situ exsolved Fe nanoparticles, *J. Mater. Chem. A.* 9 (2021) 8740–8748. <https://doi.org/10.1039/D0TA11328J>.
- [32] H. Chen, Y. Xu, K. Zhu, H. Zhang, Understanding oxygen-deficient $La_2CuO_{4-\delta}$ perovskite activated peroxy monosulfate for bisphenol A degradation: The role of localized electron within oxygen vacancy, *Appl. Catal. B Environ.* 284 (2021) 119732. <https://doi.org/https://doi.org/10.1016/j.apcatb.2020.119732>.
- [33] Ş. Ortatatlı, J. Ternieden, C. Weidenthaler, Low Temperature Formation of Ruddlesden–Popper-Type Layered $La_2CoO_{4\pm\delta}$ Perovskite Monitored via In Situ X-ray Powder Diffraction, *Eur. J. Inorg. Chem.* 2018 (2018) 5238–5245. <https://doi.org/https://doi.org/10.1002/ejic.201801162>.
- [34] X.-K. Gu, E. Nikolla, Design of Ruddlesden–Popper Oxides with Optimal Surface Oxygen Exchange Properties for Oxygen Reduction and Evolution, *ACS Catal.* 7

- (2017) 5912–5920. <https://doi.org/10.1021/acscatal.7b01483>.
- [35] S.-Y. Jeon, M.-B. Choi, H.-N. Im, J.-H. Hwang, S.-J. Song, Oxygen ionic conductivity of $\text{La}_2\text{NiO}_{4+\delta}$ via interstitial oxygen defect, *J. Phys. Chem. Solids*. 73 (2012) 656–660. <https://doi.org/https://doi.org/10.1016/j.jpics.2012.01.006>.
- [36] J. Guo, H. Lou, Y. Zhu, X. Zheng, La-based perovskite precursors preparation and its catalytic activity for CO_2 reforming of CH_4 , *Mater. Lett.* 57 (2003) 4450–4455. [https://doi.org/https://doi.org/10.1016/S0167-577X\(03\)00341-0](https://doi.org/https://doi.org/10.1016/S0167-577X(03)00341-0).
- [37] C. Jeong, J.-H. Lee, M. Park, J. Hong, H. Kim, J.-W. Son, J.-H. Lee, B.-K. Kim, K.J. Yoon, Design and processing parameters of $\text{La}_2\text{NiO}_{4+\delta}$ -based cathode for anode-supported planar solid oxide fuel cells (SOFCs), *J. Power Sources*. 297 (2015) 370–378. <https://doi.org/https://doi.org/10.1016/j.jpowsour.2015.08.023>.
- [38] X. Weng, P. Boldrin, I. Abrahams, S.J. Skinner, J.A. Darr, Direct Syntheses of Mixed Ion and Electronic Conductors $\text{La}_4\text{Ni}_3\text{O}_{10}$ and $\text{La}_3\text{Ni}_2\text{O}_7$ from Nanosized Coprecipitates, *Chem. Mater.* 19 (2007) 4382–4384. <https://doi.org/10.1021/cm070134c>.
- [39] S.J. Kim, T. Akbay, J. Matsuda, A. Takagaki, T. Ishihara, Strain Effects on Oxygen Reduction Activity of Pr_2NiO_4 Caused by Gold Bulk Dispersion for Low Temperature Solid Oxide Fuel Cells, *ACS Appl. Energy Mater.* 2 (2019) 1210–1220. <https://doi.org/10.1021/acsaem.8b01776>.
- [40] D. Waffel, B. Alkan, Q. Fu, Y.-T. Chen, S. Schmidt, C. Schulz, H. Wiggers, M. Muhler, B. Peng, Towards Mechanistic Understanding of Liquid-Phase Cinnamyl Alcohol Oxidation with tert-Butyl Hydroperoxide over Noble-Metal-Free $\text{LaCo}_{1-x}\text{Fe}_x\text{O}_3$ Perovskites, *Chempluschem*. 84 (2019) 1155–1163. <https://doi.org/10.1002/cplu.201900429>.
- [41] S. Angel, J. Neises, M. Dreyer, K. Friedel Ortega, M. Behrens, Y. Wang, H. Arandiyán, C. Schulz, H. Wiggers, Spray-flame synthesis of $\text{La}(\text{Fe}, \text{Co})\text{O}_3$ nano-

- perovskites from metal nitrates, *AIChE J.* 66 (2020) e16748.
<https://doi.org/10.1002/aic.16748>.
- [42] B. Alkan, S. Cychy, S. Varhade, M. Muhler, C. Schulz, W. Schuhmann, H. Wiggers, C. Andronescu, Spray-Flame-Synthesized $\text{LaCo}_{1-x}\text{Fe}_x\text{O}_3$ Perovskite Nanoparticles as Electrocatalysts for Water and Ethanol Oxidation, *ChemElectroChem.* 6 (2019) 4266–4274. <https://doi.org/10.1002/celec.201900168>.
- [43] F. Schneider, S. Suleiman, J. Menser, E. Borukhovich, I. Wlokas, A. Kempf, H. Wiggers, C. Schulz, SpraySyn—A standardized burner configuration for nanoparticle synthesis in spray flames, *Rev. Sci. Instrum.* 90 (2019) 85108.
<https://doi.org/10.1063/1.5090232>.
- [44] A. Grimaud, F. Mauvy, J.M. Bassat, S. Fourcade, L. Rocheron, M. Marrony, J.C. Grenier, Hydration Properties and Rate Determining Steps of the Oxygen Reduction Reaction of Perovskite-Related Oxides as H^+ -SOFC Cathodes, *J. Electrochem. Soc.* 159 (2012) B683–B694. <https://doi.org/10.1149/2.101205jes>.
- [45] L. Armelao, M. Bettinelli, G. Bottaro, D. Barreca, E. Tondello, LaCoO_3 Nanopowders by XPS, *Surf. Sci. Spectra.* 8 (2001) 24–31. <https://doi.org/10.1116/11.20010701>.
- [46] M.C. Biesinger, B.P. Payne, A.P. Grosvenor, L.W.M. Lau, A.R. Gerson, R.S.C. Smart, Resolving surface chemical states in XPS analysis of first row transition metals, oxides and hydroxides: Cr, Mn, Fe, Co and Ni, *Appl. Surf. Sci.* 257 (2011) 2717–2730.
<https://doi.org/https://doi.org/10.1016/j.apsusc.2010.10.051>.
- [47] P.H.T. Ngamou, K. Kohse-Höinghaus, N. Bahlawane, CO and ethanol oxidation over LaCoO_3 planar model catalysts: Effect of the thickness, *Catal. Commun.* 12 (2011) 1344–1350. <https://doi.org/https://doi.org/10.1016/j.catcom.2011.04.029>.
- [48] S. Pegoraro, M.M. Natile, A. Galenda, A. Glisenti, $\text{La}_2\text{Cu}_{0.8}\text{Co}_{0.2}\text{O}_{4+\delta}$ by Pechini Method, *Surf. Sci. Spectra.* 16 (2009) 75–82. <https://doi.org/10.1116/11.20090201>.
- [49] X. Duan, C. Su, L. Zhou, H. Sun, A. Suvorova, T. Odedairo, Z. Zhu, Z. Shao, S. Wang,

- Surface controlled generation of reactive radicals from persulfate by carbocatalysis on nanodiamonds, *Appl. Catal. B Environ.* 194 (2016) 7–15.
<https://doi.org/https://doi.org/10.1016/j.apcatb.2016.04.043>.
- [50] L. Wu, Y. Yu, Q. Zhang, J. Hong, J. Wang, Y. She, A novel magnetic heterogeneous catalyst oxygen-defective $\text{CoFe}_2\text{O}_{4-x}$ for activating peroxymonosulfate, *Appl. Surf. Sci.* 480 (2019) 717–726. <https://doi.org/10.1016/j.apsusc.2019.03.034>.
- [51] Y. Liu, R. Luo, Y. Li, J. Qi, C. Wang, J. Li, X. Sun, L. Wang, Sandwich-like $\text{Co}_3\text{O}_4/\text{MXene}$ composite with enhanced catalytic performance for Bisphenol A degradation, *Chem. Eng. J.* 347 (2018) 731–740.
<https://doi.org/https://doi.org/10.1016/j.cej.2018.04.155>.
- [52] X. Li, Z. Wang, B. Zhang, A.I. Rykov, M.A. Ahmed, J. Wang, $\text{Fe}_x\text{Co}_{3-x}\text{O}_4$ nanocages derived from nanoscale metal–organic frameworks for removal of bisphenol A by activation of peroxymonosulfate, *Appl. Catal. B Environ.* 181 (2016) 788–799.
<https://doi.org/https://doi.org/10.1016/j.apcatb.2015.08.050>.
- [53] X. Li, A.I. Rykov, B. Zhang, Y. Zhang, J. Wang, Graphene encapsulated Fe_xCo_y nanocages derived from metal–organic frameworks as efficient activators for peroxymonosulfate, *Catal. Sci. Technol.* 6 (2016) 7486–7494.
<https://doi.org/10.1039/C6CY01479H>.
- [54] C. Wang, H. Wang, R. Luo, C. Liu, J. Li, X. Sun, J. Shen, W. Han, L. Wang, Metal-organic framework one-dimensional fibers as efficient catalysts for activating peroxymonosulfate, *Chem. Eng. J.* 330 (2017) 262–271.
<https://doi.org/https://doi.org/10.1016/j.cej.2017.07.156>.
- [55] L. Hu, G. Zhang, Q. Wang, Y. Sun, M. Liu, P. Wang, Facile synthesis of novel $\text{Co}_3\text{O}_4\text{-Bi}_2\text{O}_3$ catalysts and their catalytic activity on bisphenol A by peroxymonosulfate activation, *Chem. Eng. J.* 326 (2017) 1095–1104.
<https://doi.org/https://doi.org/10.1016/j.cej.2017.05.168>.

- [56] R. Luo, C. Liu, J. Li, C. Wang, X. Sun, J. Shen, W. Han, L. Wang, Convenient synthesis and engineering of ultrafine Co₃O₄-incorporated carbon composite: towards practical application of environmental remediation, *J. Mater. Chem. A*. 6 (2018) 3454–3461. <https://doi.org/10.1039/C7TA11052A>.
- [57] X. ZHANG, C. HE, L. WANG, J. LIU, M. DENG, Q. FENG, Non-isothermal kinetic analysis of thermal dehydration of La₂(CO₃)₃·3.4H₂O in air, *Trans. Nonferrous Met. Soc. China*. 24 (2014) 3378–3385. [https://doi.org/https://doi.org/10.1016/S1003-6326\(14\)63480-4](https://doi.org/https://doi.org/10.1016/S1003-6326(14)63480-4).
- [58] M. Dreyer, M. Krebs, S. Najafshirtari, A. Rabe, K. Friedel Ortega, M. Behrens, The Effect of Co Incorporation on the CO Oxidation Activity of LaFe_{1-x}Co_xO₃ Perovskites, *Catal.* . 11 (2021). <https://doi.org/10.3390/catal11050550>.
- [59] S. Lu, G. Wang, S. Chen, H. Yu, F. Ye, X. Quan, Heterogeneous activation of peroxymonosulfate by LaCo_{1-x}Cu_xO₃ perovskites for degradation of organic pollutants, *J. Hazard. Mater.* 353 (2018) 401—409. <https://doi.org/10.1016/j.jhazmat.2018.04.021>.
- [60] C. Su, X. Duan, J. Miao, Y. Zhong, W. Zhou, S. Wang, Z. Shao, Mixed Conducting Perovskite Materials as Superior Catalysts for Fast Aqueous-Phase Advanced Oxidation: A Mechanistic Study, *ACS Catal.* 7 (2017) 388–397. <https://doi.org/10.1021/acscatal.6b02303>.
- [61] X. Tian, P. Gao, Y. Nie, C. Yang, Z. Zhou, Y. Li, Y. Wang, A novel singlet oxygen involved peroxymonosulfate activation mechanism for degradation of ofloxacin and phenol in water, *Chem. Commun.* 53 (2017) 6589–6592. <https://doi.org/10.1039/C7CC02820B>.
- [62] P. Neta, R.E. Huie, A.B. Ross, Rate Constants for Reactions of Inorganic Radicals in Aqueous Solution, *J. Phys. Chem. Ref. Data*. 17 (1988) 1027–1284. <https://doi.org/10.1063/1.555808>.

- [63] G.P. Anipsitakis, D.D. Dionysiou, Degradation of Organic Contaminants in Water with Sulfate Radicals Generated by the Conjunction of Peroxymonosulfate with Cobalt, *Environ. Sci. Technol.* 37 (2003) 4790–4797. <https://doi.org/10.1021/es0263792>.
- [64] R. Luo, M. Li, C. Wang, M. Zhang, M.A. Nasir Khan, X. Sun, J. Shen, W. Han, L. Wang, J. Li, Singlet oxygen-dominated non-radical oxidation process for efficient degradation of bisphenol A under high salinity condition, *Water Res.* 148 (2019) 416–424. <https://doi.org/https://doi.org/10.1016/j.watres.2018.10.087>.
- [65] X. Dong, B. Ren, Z. Sun, C. Li, X. Zhang, M. Kong, S. Zheng, D.D. Dionysiou, Monodispersed CuFe₂O₄ nanoparticles anchored on natural kaolinite as highly efficient peroxymonosulfate catalyst for bisphenol A degradation, *Appl. Catal. B Environ.* 253 (2019) 206–217. <https://doi.org/https://doi.org/10.1016/j.apcatb.2019.04.052>.
- [66] A.F. Lucrédio, G.T. Filho, E.M. Assaf, Co/Mg/Al hydrotalcite-type precursor, promoted with La and Ce, studied by XPS and applied to methane steam reforming reactions, *Appl. Surf. Sci.* 255 (2009) 5851–5856. <https://doi.org/https://doi.org/10.1016/j.apsusc.2009.01.020>.
- [67] Z. Shao, S.M. Haile, A high-performance cathode for the next generation of solid-oxide fuel cells, *Nature.* 431 (2004) 170–173. <https://doi.org/10.1038/nature02863>.
- [68] S. Baumann, F. Schulze-Küppers, S. Roitsch, M. Betz, M. Zwick, E.M. Pfaff, W.A. Meulenber, J. Mayer, D. Stöver, Influence of sintering conditions on microstructure and oxygen permeation of Ba_{0.5}Sr_{0.5}Co_{0.8}Fe_{0.2}O_{3-δ} (BSCF) oxygen transport membranes, *J. Memb. Sci.* 359 (2010) 102–109. <https://doi.org/https://doi.org/10.1016/j.memsci.2010.02.002>.
- [69] M.M. Kuklja, E.A. Kotomin, R. Merkle, Y.A. Mastrikov, J. Maier, Combined theoretical and experimental analysis of processes determining cathode performance in solid oxide fuel cells, *Phys. Chem. Chem. Phys.* 15 (2013) 5443–5471.

<https://doi.org/10.1039/C3CP44363A>.

- [70] Y. Huang, C. Han, Y. Liu, M.N. Nadagouda, L. Machala, K.E. O'Shea, V.K. Sharma, D.D. Dionysiou, Degradation of atrazine by $Zn_xCu_{1-x}Fe_2O_4$ nanomaterial-catalyzed sulfite under UV-vis light irradiation: Green strategy to generate SO_4^- , *Appl. Catal. B Environ.* 221 (2018) 380–392.

<https://doi.org/https://doi.org/10.1016/j.apcatb.2017.09.001>.

- [71] Y. Feng, P.-H. Lee, D. Wu, K. Shih, Surface-bound sulfate radical-dominated degradation of 1,4-dioxane by alumina-supported palladium (Pd/Al₂O₃) catalyzed peroxymonosulfate, *Water Res.* 120 (2017) 12–21.

<https://doi.org/https://doi.org/10.1016/j.watres.2017.04.070>.